UNIVERSITY OF CALIFORNIA,
IRVINE

Nonlinear Optical Microscopy and Spectroscopy Studies of Biological Molecules

DISSERTATION

submitted in partial satisfaction of the requirements
for the degree of

DOCTOR OF PHILOSOPHY

in Chemistry

by

Julie Chih-chi Hsu

Dissertation Committee:
Professor Eric Olaf Potma, Chair
Professor Robert M. Corn
Professor Nien-Hui Ge

2017

DEDICATION

To

My family and friends
who have supported me
throughout my time at UCI

TABLE OF CONTENTS

LIST OF FIGURES

LIST OF TABLES

ACKNOWLEDGMENTS

I would like to express the deepest appreciation to my committee chair, Professor Eric O. Potma, for his guidance and encouragement over the course of my degree. His insight and support have been invaluable to my learning experience. Without his help this dissertation would not have been possible.

I would like to thank my committee members, Professor Nien-Hui Ge and Professor Robert M. Corn, for their input in my research that has helped me move forward in my progress. Additionally, I wish to express my gratitude to Professor Vasan Venugopalan for the opportunity to participate in the interdisciplinary BEST IGERT program.

I wish to thank Dr. Chao-Yu Chung, Dr. Yang Han, Professor Eun Seong Lee, and Professor Nien-Hui Ge for their collaboration on the sum frequency microscope project. I learned a lot from them over the course of the project. I would also like to deeply thank Dr. Dima Fishman for his support in the sum frequency project and the melanin project.

Furthermore, I thank all the Potma Lab members for the great time spent together. I also extend a special thank you to my classmates and friends in the Department of Chemistry for being there for me.

I would like to acknowledge the American Physical Society and American Chemical Society for permission to include copyrighted content as part of my thesis.
Portions of Chapter 3 reprinted (abstract/excerpt/figure) with permission from Chao-Yu Chung, Julie Hsu, Shaul Mukamel, and Eric O. Potma, Phys. Rev. A 87, 033833 (2013). Copyright (2013) by the American Physical Society.
Portions of Chapter 4 reprinted with permission from Yang Han, Julie Hsu, Nien-Hui Ge, and Eric O. Potma, The Journal of Physical Chemistry B 119 (8), 3356-3365 (2015). Copyright {2015} American Chemical Society.
Financial support was provided by NSF GRFP Fellowship and NSF IGERT Traineeship Program NSF-DGE-1144901.

CURRICULUM VITAE

Julie Chih-chi Hsu

EDUCATION

Doctor of Philosophy in Chemistry, 2011-2017

Department of Chemistry, University of California, Irvine, CA, U.S.A.

Bachelor of Science, 2007- 2011

National Tsing-Hua University, Hsinchu, Taiwan

Exchange Student, 2009-2010

University of California, Riverside, CA, U.S.A.

EXPERIENCE

Graduate Research Assistant, 2012-2017

Department of Chemistry, University of California, Irvine, CA, U.S.A.

Intern, July 2015-Jan 2016

Smithsonian National Museum of Natural History, Washington D.C.,U.S.A.

Teaching Assistant, 2011-2012, 2017

Department of Chemistry, University of California, Irvine, CA, U.S.A.

Undergraduate Researcher, Jan 2010-June 2010

Department of Chemistry, University of California, Riverside, CA, U.S.A.

Undergraduate Summer Intern, June 2008-Sept 2008

National Tsing-Hua University, Hsinchu, Taiwan

AWARDS

National Science Foundation GRFP Fellowship *2012-2017*

National Science Foundation IGERT Traineeship *2012-2014*

University of California, Irvine Teaching Assistant Award *2011-2012*

PUBLICATIONS

1. Moore, B.; Sun, Q.; Hsu, J.C.; Lee, A.H.; Yoo, G.C.; Ly, T.; Julian, R.R., "Dissociation Chemistry of Hydrogen-Deficient Radical Peptide Anions."*Journal of the American Society for Mass Spectrometry.* **23,** 460-468 (2012).

2. Chung, C.-Y.; Hsu, J; Mukamel, S.; Potma, E.O., "Controlling stimulated coherent spectroscopy and microscopy by a position-dependent phase" *Physical Review A.* **87**, 033833 (2013).

3. Lee, E.S.; Lee, S.W.; Hsu, J.; Potma, E.O., "Vibrationally resonant sum-frequency generation microscopy with a solid immersion lens," *Biomedical Optics Express* **5**, 2125-2134 (2014).

4. Han, Y.; Hsu, J.; Ge, N.-H.; Potma, E.O., "Polarization-Sensitive Sum-Frequency Generation Microscopy of Collagen Fibers," *Journal of Physical Chemistry B.* **119**, 3356-3365 (2015).

ABSTRACT OF THE DISSERTATION

Nonlinear Optical Microscopy and Spectroscopy Studies of Biological Molecules

By

Julie Chih-chi Hsu

Doctor of Philosophy in Chemistry

University of California, Irvine, 2017

Associate Professor Eric Olaf Potma, Chair

Coherent nonlinear optical microscopy is a rapidly developing field that is widely applicable to the study of biological molecules and systems. These techniques have the inherent advantages of high speed and resolution, three-dimensional focusing, minimal sample damage, and label free chemical selectivity. In this thesis, applications of different vibrationally resonant nonlinear techniques to studying the optical and chemical properties of biological molecules are explored. The noncentrosymmetry sensitive vibrationally-resonant sum frequency generation microscopy is used in a polarization sensitive study of collagen second order nonlinear susceptibility tensor terms. Transient absorption spectroscopy is used to explore the excited state dynamics of of Sepia melanin. Additionally, position dependent phase shifts and changes in spectra in stimulated Raman microscopy are calculated. Optical design of achromatic lenses for implementation in sum frequency generation microscopy is also included.

Chapter 1. Introduction

Nonlinear optical spectroscopy is an advantageous modality for the study of optical and chemical characteristics of biological samples. There are many different forms of nonlinear optical spectroscopy techniques that can probe different optical processes. The signals generated through nonlinear optical spectroscopy techniques show nonlinear dependence on the incident light and require high photo density, spatial coherence, and temporal coherence [1]. The spatial coherence and high photon density requirements allow for three-dimensional focusing on sample locations. Additionally, the wavelengths of the excitation light can be chosen such as to accommodate experimental or sample requirements such as using infrared wavelengths to obtain vibrational resonance with the sample, near-infrared wavelengths to avoid biological tissue absorption, or multiple wavelength combinations to allow signal detection in the visible range. The ability to tune the incident light to match the vibrational or electronic resonances of the sample allows for label-free chemical specificity with minimal sample damage.

In this chapter the general form of nonlinear optical responses is introduced, while three different nonlinear optical spectroscopy modalities relevant to the work presented in the following chapters will be briefly described.

1.1. Nonlinear Optical Response

The nonlinear optical response can be generally expressed by writing out the polarization induced by the interaction of an electric field with a sample. When an electric field interacts with a sample, the sample is polarized:

$$P=\chi E \tag{1.1}$$

where P is the induced polarization, E is the incident electric field, and χ is the susceptibility, a proportionality factor between the electric field and the polarization. χ is a property of the sample, but in strong electric fields the susceptibility becomes dependent on the field applied as well [2]:

$$P= \chi(E) E \tag{1.2}$$

This expression can then be expanded with a power series to obtain:

$$\chi(E) = \chi^{(1)} + \chi^{(2)} E + \chi^{(3)}E^2 + ... \tag{1.3}$$

and

$$P = \chi^{(1)}E + \chi^{(2)} E^2 + \chi^{(3)}E^3 + ... \tag{1.4}$$

Aside from the linear first term, the higher order terms are the origin of the nonlinear optical response. Here χ is a tensor that relates the components of the electrical field to the induced polarization in each component. These susceptibility terms are small, and therefore the nonlinear signal is usually weak and requires high incident photon intensities to be detected.

1.2. Stimulated Raman Scattering

Raman scattering is a form of inelastic scattering where a photon interacts with material to produce an emitted photon of different energy. There are two possible types of Raman scattering: Stokes and anti-Stokes. In Stokes scattering, the emitted photon has lower energy than the incident photon, while in anti-Stokes scattering the emitted photon has higher energy than the incident photon. The difference in energy results from interaction with energy states of the

material, and therefore the resulting emitted wavelengths will be dependent on the properties of the material. The intensity of spontaneous Raman scattering can be expressed as [3]:

$$I(\omega_s) = N\, z\, \sigma(\omega_s)\, I_0 \tag{1.5}$$

where N is the molecular number density, z is the path length, $\sigma(\omega_s)$ is the cross section of the sample molecules at wavelength ω_s, and I_0 is the intensity of the incident light. Typical cross sections for organic liquids are on the order of magnitude of 10^{-29} cm^2, and as such spontaneous Raman scattering is a relatively weak process [1]. The signal is isotropic and incoherent. To improve the signal generation and obtain coherent signal, stimulated Raman scattering can be used instead.

Stimulated Raman scattering is a third order nonlinear optical process. It uses two incident fields, the pump E_p and the Stokes E_s with frequencies of ω_p and ω_s, respectively. When the difference between ω_p and ω_s is close to a vibrational mode of the sample, a stimulated Raman resonance is produced. Stimulated Raman scattering can be detected with either a stimulated Raman gain (SRG) mode or a stimulated Raman loss (SRL) mode. In stimulated Raman loss, the signal generated is at the same frequency as the incoming pump wavelength ω_p. The process is an energy transfer that results in a loss of signal for the incident pump field. This can be detected through frequency modulation of the incident pump field and detection with a lock-in. The polarization response for stimulated Raman loss can be expressed as:

$$P^{(3)}(\omega_p) = \chi^{(3)}(\omega_p)\, |E_s|^2\, E_p \tag{1.6}$$

As stimulated Raman scattering only detects the imaginary part of the nonlinear susceptibility, the SRS spectra show absorption curve shapes that directly correspond to the spontaneous Raman spectra and are free of nonresonant background. This methodology has the advantages of

chemical specificity, good signal-to-noise ratio, and efficient signal acquisition that is desired for biological sample studies.

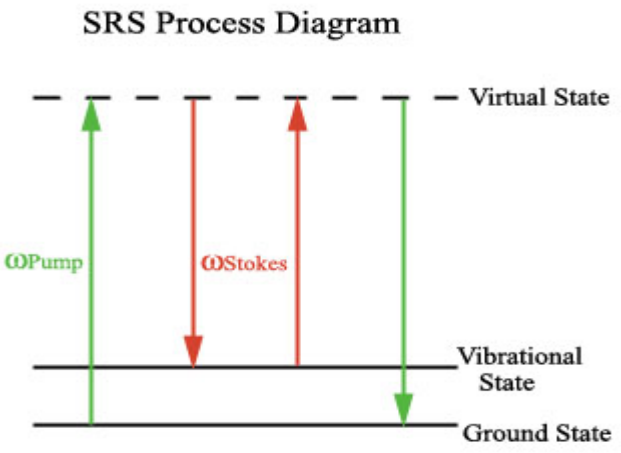

Figure 1.1: Schematic diagram of stimulated Raman scattering process. The molecule, initially in the ground state, interacts with the pump beam and Stokes beam, which have a frequency difference that matches a vibrationally excited state.

1.3. Sum Frequency Generation

Sum frequency generation is a second order nonlinear process where two frequencies ω_1 and ω_2 interact with the sample to generate a signal frequency at $\omega_3 = \omega_1 + \omega_2$ (Figure 1.2). Sum frequency generation is only sensitive to systems without inversion symmetry, such as surfaces or bulk noncentrosymmetric systems. The second-order susceptibility $\chi^{(2)}$ signal vanishes in systems with inversion symmetry due to dipole approximations [4]. As such it has been a widely used spectroscopic technique for surface specific measurements such as surface monolayers, molecular adsorbates at interfaces, semiconductor and metal surfaces, and surface reaction

dynamics [5-7]. The technique can be taken further to provide chemical specificity when one of the incident frequencies is chosen to be in resonance with a vibrational mode of the sample. This is referred to as vibrationally-resonant sum frequency generation (VR-SFG), and the signal in such a process is largely enhanced due to the resonance.

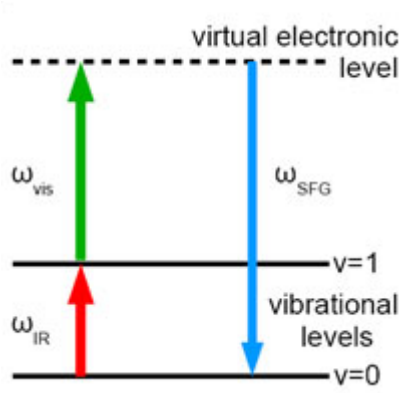

Figure 1.2: Schematic diagram of the sum frequency generation process. The first frequency is chosen to be in resonance with the vibrational level of the molecule for a VR-SFG.

1.4. Electronic Pump Probe Spectroscopy

Pump probe spectroscopy is a nonlinear technique used to observe the transient absorption of a molecule. In this technique, a pump beam is used to excite the sample molecule, then a probe beam is used to detect the changes in the excited state as a function of wavelength and time. The many variables that can be probed allows the pump probe technique to distinguish otherwise spectrally similar molecules as well as the dynamics of these optical processes.

In pump probe spectroscopy, the molecule is excited by absorption of the pump beam from the ground state S0 to some excited state S1. The molecule may undergo internal conversion to

arrive at state S2. From this state, the molecule interacts with a second beam, the probe. The probe may drive the molecule in three ways[8]:

1. From S2, the molecule absorbs the probe beam and arrives at an excited state S3.
2. The probe beam drives stimulated emission of the molecule from S2 to S0.
3. The probe depletes the ground state S0 by driving a S0-S4 transition.

The processes are shown in Figure 1.3. The signal is detected by applying a modulated pump beam, then applying the probe beam at varying times delays after the pump beam, and collecting the ratio of the absorption of the probe with and without the pump. In this detection scheme, of the above mentioned cases, case 1 generates a positive signal, while case 2 and 3 generate negative signals. The pump probe spectroscopy can be applied to study pump induced changes in the probe and the optical pathways of a molecule.

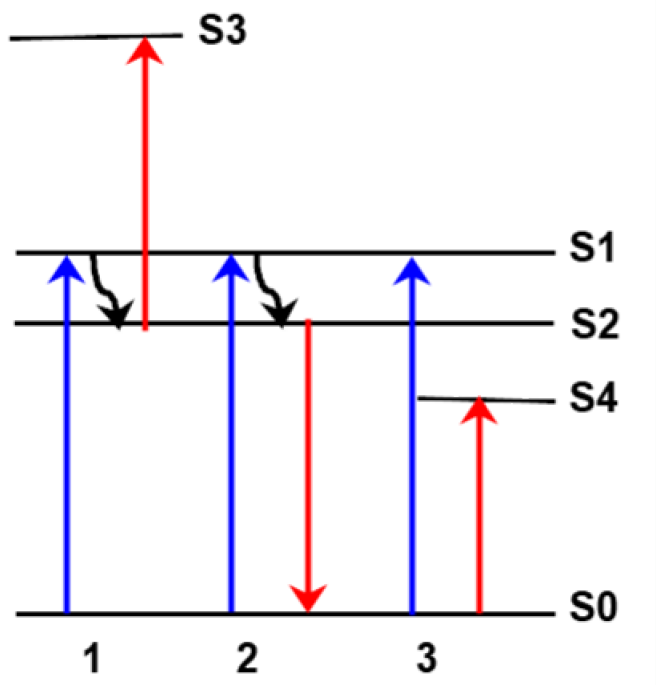

Figure 1.3: Schematic diagram of pump probe processes. Three scenarios are shown from left to right: 1) excited state absorption, 2) stimulated emission, 3) ground state depletion.

Chapter 2. Achromatic Optical Lens Design

Vibrationally-resonant sum frequency generation has the unique qualities of surface noncentrosymmetry specificity as well as chemical specificity. Although these qualities make it advantageous for studies of certain systems such as surface monolayers or surface reaction dynamics, it has remained mostly a spectroscopic technique. Development of a VR-SFG microscope has been met with difficulties in meeting the imaging requirements of high speed and resolution [9-11]. The setup previously assembled in our research group provides an improvement to the VR-SFG microscope by featuring picosecond pulsed beams and collinear illumination. However, it is still unable to achieve the resolution and speed of other common coherent nonlinear microscopy techniques due to limitations in the optics. In this chapter, alternative designs that can improve the performance of the VR-SFG microscope are evaluated.

2.1. Introduction

The VR-SFG microscope setup (Figure 2.1) features improvements over previous designs due to implementation of pulsed picosecond lasers and collinear illumination with a focusing objective [12]. The objective chosen is a 0.65 NA, 74x reflective objective, as this allows for focusing of both the near-infrared and mid-infrared beams even as the wavelengths generated by the optical parametric oscillator are tuned to generate vibrational resonances with the sample. The image is obtained by loading the sample on a two dimensional piezo stage and scanning it across the optical beam path. Although this configuration works, as will be demonstrated in Chapter 4, there are still many improvements to be desired.

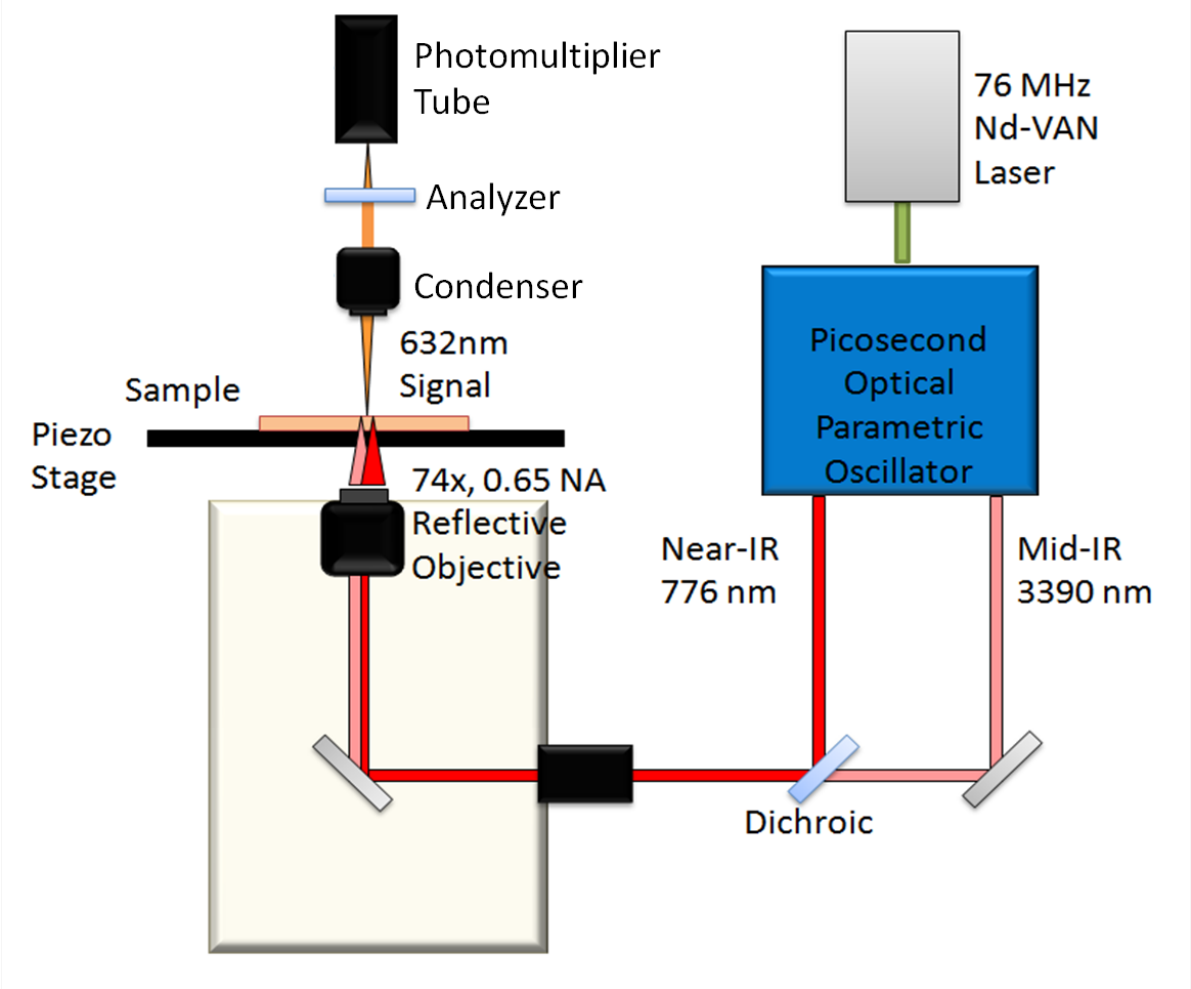

Figure 2.1: VR-SFG microscope setup with reflective objective and piezo stage scanning.

On the issue of imaging speed, the above setup is limited by the speed of the sample piezo stage scanning over the optical axis. The speed of image scanning can be greatly improved by scanning the optical path of the laser beam instead through use of a mirror galvanometer. The use of the mirror galvanometer can reduce the time necessary for imaging a 512 by 512 pixel image from up to ten minutes to less than 30 seconds. The implementation of beam scanning will require reducing the beam diameter to less than the galvo mirror size, then re-expanding the beam diameter to fill the back aperture of the objective lens [13]. The reducing of the beam size

can be accomplished by use of a pair of curved mirrors, while the re-expanding of the beam requires implementation of a scan and tube lens pair. Curved mirrors would not work well for this purpose as the scanned beam can not be aimed at the center of the mirror, and it is physically difficult to mount the curved mirror inside commercial microscope housing. The scan and tube lens pair also serve the additional function of creating a conjugate plane pair between the galvo mirrors and the back aperture of the objective lens. This allows the beam to be stationary at the back aperture of the objective lens and then scan over the focal plane. Due to the large difference in the frequencies ω_1 and ω_2, finding a suitable scan and tube lens pair that does not induce severe chromatic aberration, where different wavelengths of light are focused onto different focal points, is an issue that must be addressed.

On the issue of resolution, the reflective objective lens (Edmund Optics, 0.65 NA, 74x) was found to have poor axial focusing along the optical axis due to the obstruction of the center of the incident beam in the reflective design. A refractive based objective lens capable of focusing in both the mid-infrared and near infrared would be highly desirable for improving the performance of the VR-SFG microscope [14]. As of current, there are no suitable commercial lenses that are capable of focusing such a wide range of near-IR and mid-IR wavelengths simultaneously to the same point, and a new design is necessary.

The improved configuration for the VR-SFG microscope is shown in Figure 2.2 in comparison with the original configuration. The implementation of laser scanning and a complete set of refractive, achromatic lenses is expected to allow the VR-SFG microscope to achieve resolution, speed, and image quality similar to techniques such as coherent anti-Stokes Raman scattering.

a

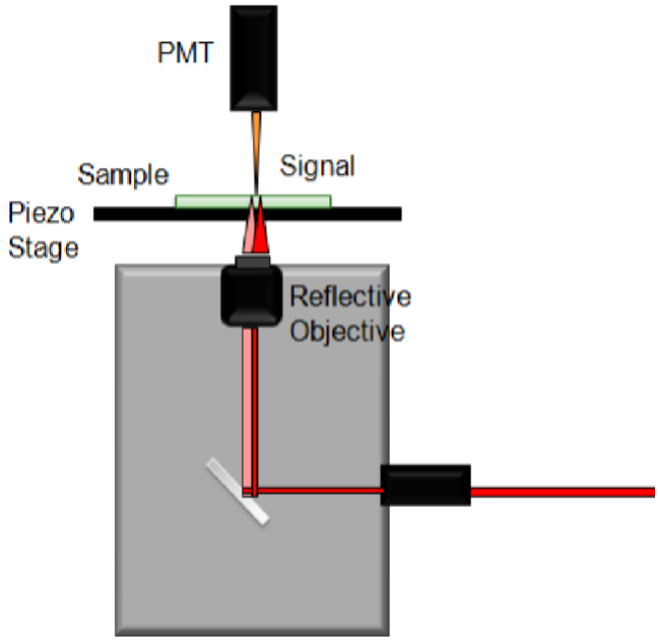

b

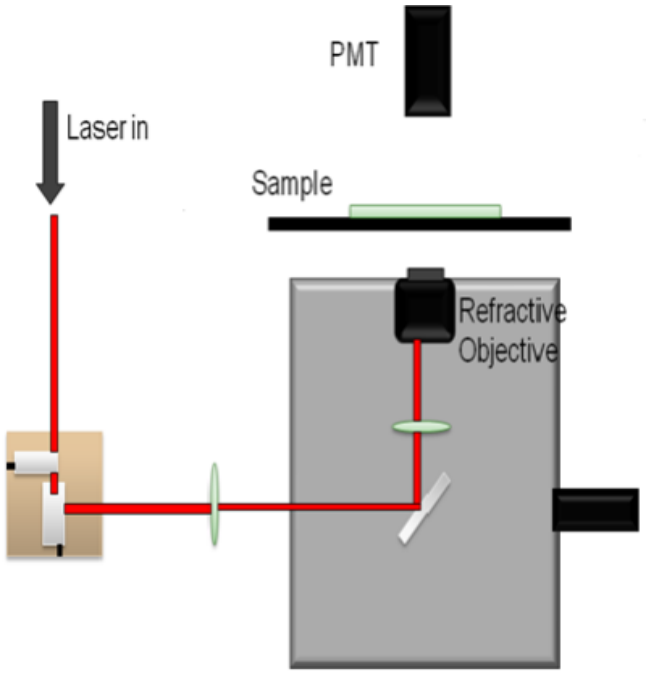

Figure 2.2: Schematic diagrams of VR-SFG microscope setups. a) Original setup consisting of piezo stage sample scanning and a reflective objective. b) New setup consisting of mirror galvanometer laser scanning and a refractive objective.

2.2. Selection of Materials

In order to design custom refractive lenses for the VR-SFG microscope, selection of appropriate lens materials is important. Main selection criteria for lens materials include:

1. Transmission range: the lens material needs to have efficient transmission for the near-infrared to mid-infrared range (wavelengths of VR-SFG interest range from 750 nm to 3400 nm).

2. Small $\chi^{(2)}$: the lens material should not itself have a large sum frequency generation signal that would interfere with the imaging.

3. Refractive index: the scattering properties of the materials selected should complement each other in order to produce an achromatic effect where the overall refractive index is relatively constant over the range of wavelengths of interest.

4. Other considerations for practicality: special characteristics that may be impractical for use as lens material, such as rarity, toxicity, hygroscopic, or large thermal expansion.

The selection of materials was first narrowed down by considering crystals and glasses that had considerable transmission within the range of interest. As it is a wide range covering near-infrared to mid-infrared, only some select crystals fit the criteria, and not many commercial glass options are available. Table 2.1 compiles a list of crystalline materials and their transmission ranges that are potentially a fit for the range of interest [15-17]. The comments include special characteristics that may need consideration. Table 2.2 lists some special infrared commercial glasses that best match the transmission criteria and the other available information on these glasses. Unfortunately after inquiry the production of special glasses that match the transmission

Table 2.1: Transmission ranges of crystals.

Material	Transmission Range	Comments
CaF2	0.13-10	
BaF2	0.14-13	slightly hygroscopic
SrF2	0.21-11.5	
MgF2	0.2-7.7	
PbF2	0.25-11	toxic
LiF	0.1-11	
ZnS	0.37-13.5	large χ2
ZnSe	0.6-21	large χ2
Al2O3 (Sapphire)	0.15-5	
MgAl2O4 (Spinel)	0.4-5	
Tl[Br,I] (KRS-5)	0.6-40	toxic
Tl[Cl,Br] (KRS-6)	0.4-25	toxic
SiO2 (IR grade fused silica)	0.18-3.5	high partial dispersion
MgO	0.36-5.4	
KBr	0.23-25	hygroscopic
CsBr	0.25-40	hygroscopic, large thermal expansion
NaBr	0.17-18	hygroscopic
KCl	0.21-21	hygroscopic
NaCl	0.2-15	hygroscopic
AgCl	0.4-25	slightly light sensitive
CsCl	0.19-30	hygroscopic
NaI	0.26-24	hygroscopic, large thermal expansion
KI	0.38-35	hygroscopic
CsI	0.25-55	hygroscopic
TiO2	0.43-5	
Y3Al5O12 (YAG)	0.21-5.5	
Y2O3	0.2-12	
As2S3	0.6-11	
GaN	0.35-10	
AlN	0.22-5	
Ag3AsS3	0.63-4.6	
SrTiO3	0.43-3.8	
BeO	0.44-7	
CaMoO4	0.45-3.8	
CaWO4	0.45-4	
KNbO3	0.4-5.3	birefringent
KTiOPO4	0.43-3.54	birefringent
LiIO3	0.5-5	
CuGaS2	0.55-11.5	
GaS	0.633-10.59	
HfO2-Y2O3	0.365-5	
ZrO2-Y2O3	0.36-5.1	

Material	Transmission Range	Type	Abbe #	n(775)	n(3.39)	Δn
Special Glasses						
Schott IRG 2	0.44-5.1	Flint	30	1.871	1.8253	0.0457
Schott IRG 3	0.4-4			1.83	1.7764	0.0536
Schott IRG N6	0.25-4.75			1.582	1.5451	0.0369
Schott IRG 7	0.4-4			1.556	1.5164	0.0396
Schott IRG 9	0.38-4.1	Crown	81	1.482	1.458	0.024
Schott IRG 11	0.44-4.75	Flint	44.2	1.67	1.6349	0.0351
Schott IG 2	0.85-12			2.66866	2.5158	0.15286
Schott IG 4	0.85-11.5			2.8162	2.6248	0.1914
Ohara S-FTM16	0.35-2.4	Flint	35.31	1.58217		
Ohara HTF-1	0.21-6.9	Crown	92.5	1.52	1.5	0.02
Corning 9753	0.38-4.3			1.595	1.56	0.035
Corning 9754	0.36-4.8	Flint	46.5		1.62	
ZBL (fluoride glass)	0.25-7.0					
ZBLA (fluoride glass)	0.29-7.0	Crown	62			
ZBLAN (fluoride glass)	0.25-6.9	Crown	64			
ZBT (fluoride glass)	0.32-6.8					
BS-39B (Barr&Stroud)	0.38-4.9	Flint	44.5			
BD-2 (LightPath)	0.8-14				2.6266	
Ultran 30 (Schott)	0.23-3.95	Crown	74.3			
Poly IR 5 (Fresnel Technologies)	0.4-5					
IKC23 (Lzos)	0.7-11					
IKC24 (Lzos)	0.7-11					

Table 2.2: Transmission ranges of special glasses.

criteria have mostly been discontinued by companies. This narrows the search down to crystal materials that fit the transmission range and do not have practicality considerations. Table 2.3 lists the second order nonlinear response of some of the crystals from Table 2.1; those with high second order nonlinear response are also unsuitable for the purpose.

Table 2.3: Second order nonlinear susceptibilities for crystals.

Second Order Susceptibilities	
Material	d(1064) in pm/V
Quartz	0.3
ZnS	20
ZnSe	27
ZnTe	90
$LiNbO_3$	7
ADP	0.46
KDP	0.63
GaN	8.2
AlN	7
GaP	99.7
$LiIO_3$	7.11
$AgGaSe_2$	37
$KTiOPO_4$	5.85

After the above considerations, the refractive index is also an important factor in determining whether the material is suitable or not. Typically materials have some amount of dispersion, where the refractive index of a material will vary as a function of the wavelength, and as such it is not possible to achieve the same focus for two widely separated wavelengths using only a single material. Therefore an achromatic lens is required. The achromatic lens usually consists of

two individual lenses made from two materials that have different amounts of dispersion. One lens is made of a material that has higher dispersion (flint), and the other is made of a material with lower dispersion (crown). The two lenses shaped and are mounted together so that the overall effective lens has reduced chromatic aberration and is able to bring two different wavelengths to the same focus. When considering dispersion properties of lens materials for an achromat, the Abbe number is a frequently used measure. The standard Abbe number V is expressed by:

$$V_D = \frac{n_D - 1}{n_F - n_C}, \tag{2.1}$$

where n_D, n_F and n_C are the refractive indices of the material at the wavelengths 589, 486 nm and 656 nm, respectively [18]. The wavelengths chosen for calculating the Abbe number can be modified in some instances to calculate a dispersion index more specific to the case at hand. Table 2.4 shows the Abbe number, refractive index, and classification of the crystals previously examined in Table 2.1.

For a first order design, the Abbe number and the focusing power of the two lenses coupled in the achromat can be chosen so as to satisfy:

$$\frac{\phi_1}{V_1} + \frac{\phi_2}{V_2} = 0\,, \tag{2.2}$$

where ϕ_1 and ϕ_2 are the focusing power of the first lens and second lens, respectively, and V_1 and V_2 the Abbe number of the two lenses [18].

Table 2.4: Refractive indices of crystals.

Material	n(775)	n(3.39)	Δn	Abbe #	Type
CaF2	1.4308	1.41493	0.01587	94.96	Crown
BaF2	1.47072	1.45955	0.01117	81.61	Crown
SrF2	1.43474	1.41874	0.016	91.59	Crown
MgF2	1.37529	1.35602	0.01927	106.22	Crown
PbF2	1.75012	1.72106	0.02906	28.51	Flint
LiF	1.38926	1.36039	0.02887	97.29	
ZnS	2.31719	2.25504	0.06215		Flint
ZnSe	2.53047	2.43565	0.09482		Flint
Al2O3 (Sapphire)	1.7606	1.726	0.0346	72.4	Crown
MgAl2O4 (Spinel)	1.70824	1.65757	0.05067	60.67	Crown
Tl[Br,I] (KRS-5)	2.49758	2.384	0.11358		
Tl[Cl,Br] (KRS-6)	2.19628	2.19342	0.00286		
SiO2 (IR grade fused silica)	1.45376	1.4091	0.04466	67.41	Crown
MgO	1.72845	1.68311	0.04534	53.5	Crown
KBr	1.54971	1.53634	0.01337	33.64	Flint
CsBr	1.68444	1.66858	0.01586	34.11	Flint
NaBr	1.63045	1.61301	0.01744	31.72	Flint
KCl	1.48348	1.47317	0.01031	44.39	Flint
NaCl	1.53625	1.52327	0.01298	42.89	Flint
AgCl	2.03712	2.00141	0.03571		Flint
CsCl	1.63121	1.61871	0.0125	43.92	Flint
NaI	1.75701	1.73414	0.02287	26.69	Flint
KI	1.6494	1.62875	0.02065	23.66	Flint
CsI	1.76733	1.74356	0.02377	23.99	Flint
TiO2	2.48893	2.41	0.07893		
Y3Al5O12 (YAG)	1.82235	1.77357	0.04878		
Y2O3	1.9128	1.86934	0.04346	32.95	Flint
As2S3	2.52756	2.41386	0.1137		
GaN	2.35724	2.28184	0.90097	18.78	Flint
AlN	2.1399	2.07728	0.06262	50.73	Crown
Ag3AsS3	2.90002	2.73911	0.16091		
SrTiO3	2.34704	2.214	0.13304	12.71	Flint
BeO	1.71319	1.65877	0.05442	93.25	Crown
CaMoO4	1.97084	1.91645	0.05439	28.83	Flint
CaWO4	1.90367	1.85825	0.04542	34.95	Flint
KNbO3	2.14316	2.05033	0.09283	18	Flint
KTiOPO4	1.74975	1.68107	0.06868	25.56	Flint
LiIO3	1.86792	1.82589	0.04203		
CuGaS2	2.59947	2.49233	0.10714		
GaS	2.66579	2.57625	0.08954		
HfO2-Y2O3	2.09351	2.03473	0.05878	39.53	Flint
ZrO2-Y2O3	2.13704	2.06958	0.06746	33.54	Flint

In the 1962 study by Herzberger and Salzburg, a method for selecting appropriate pairs of materials for achromatic lenses is proposed [19]. According to their method, a modified Abbe number can be calculated as follows:

$$\nu = \frac{n(\lambda_2) - 1}{n(\lambda_1) - n(\lambda_3)} \tag{2.3}$$

and a partial dispersion defined as:

$$P = \frac{n(\lambda_2) - n(\lambda_3)}{n(\lambda_1) - n(\lambda_3)} \tag{2.4}$$

To find suitable achromat pairs for the range $\lambda 1 < \lambda 2 < \lambda 3$, one should try to find a pair that maximizes $\Delta \nu$ and minimizes ΔP. Oliva and Gennari apply this to some combinations of near-infrared materials in their 1995 study and note possible pairs [20]. Following this method, the above mentioned criteria, and considerations on the availability of the material, the list can be narrowed down to calcium fluoride (CaF_2) and magnesium oxide (MgO), a pair of materials that would be suitable for an achromatic lens in the near-infrared to mid-infrared region. In the following section, lenses consisting of these two materials are modeled to see if indeed they could fix the chromatic aberration in the VR-SFG microscope system.

2.3. Results and Discussion

Designs for achromats, starting with a scan and tube lens and finally a refractive objective, are chosen with the actual dimensions and parameters of the VR-SFG microscope setup in mind. The optical design and performance were modeled and optimized using Zemax (Radiant LLC).

Briefly, the scan lens was located approximately 50 mm from the galvo mirrors, with an incoming beam width of 1.41 mm and scan angles of ± 2 degrees. the distance between the scan lens and the tube lens housed in the microscope frame was approximately 180 mm, and the distance between the tube lens and the objective was approximately 145 mm. The incident beam from the galvo scanning mirrors required expansion of approximately 3 times to just overfill the back aperture of the objective lens. As the scan and tube lens act as the beam expander, the expansion ratio of 3 determines their relative focal lengths. Therefore, the scan lens was designed as a 1 inch lens with an effective focal length of approximately 45 mm, the tube lens with approximately 135 mm, and the objective with 2 mm and characteristics similar to the 0.65 NA, 74x of the reflective objective.

The design and performance of the scan lens with the calcium fluoride and magnesium oxide achromat is shown in Figure 2.3 in comparison with a calcium fluoride singlet. It can be seen that the doublet performance focuses the two wavelengths (0.775 and 3.39 μm) to a much closer point than the singlet does. The singlet produces a chromatic focal shift of roughly 3.8 mm while the achromatic doublet only produces about 20 μm of focal shift.

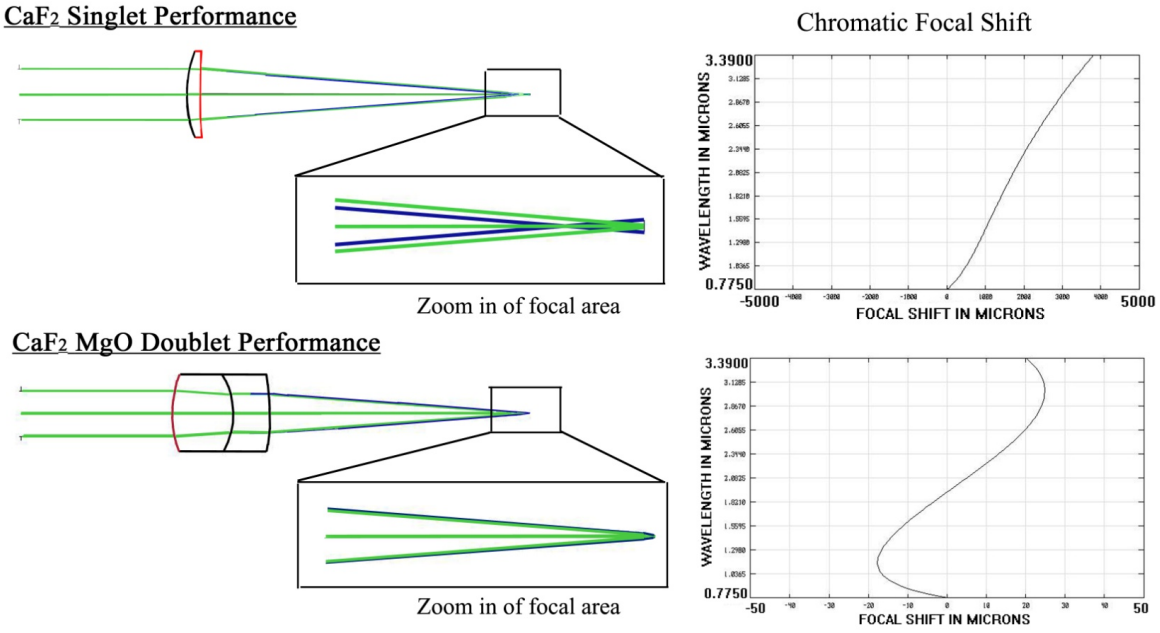

Figure 2.3: Comparison of optical performance of a calcium fluoride and magnesium oxide doublet scan lens with a calcium fluoride singlet.

The large improvement in reducing chromatic focal shift that the achromatic doublet offers is further highlighted in Figure 2.4. The figure demonstrates that there is indeed an improvement in chromatic focal shift to be obtained through the design of achromatic doublets of the calcium fluoride/oxide pair. As such, the designs were optimized in Zemax with a RMS spot radius based merit function with additional significant weight placed on the longitudinal chromatic aberration while varying weights were placed on other terms of aberration that appeared to be dominant. Reasonable limitations were also placed on the thickness (between 2 to 20 mm) and curvature of the surfaces. Several configurations were tested, and multiple rounds of local Hammer optimization and global optimization were performed to reach the final design.

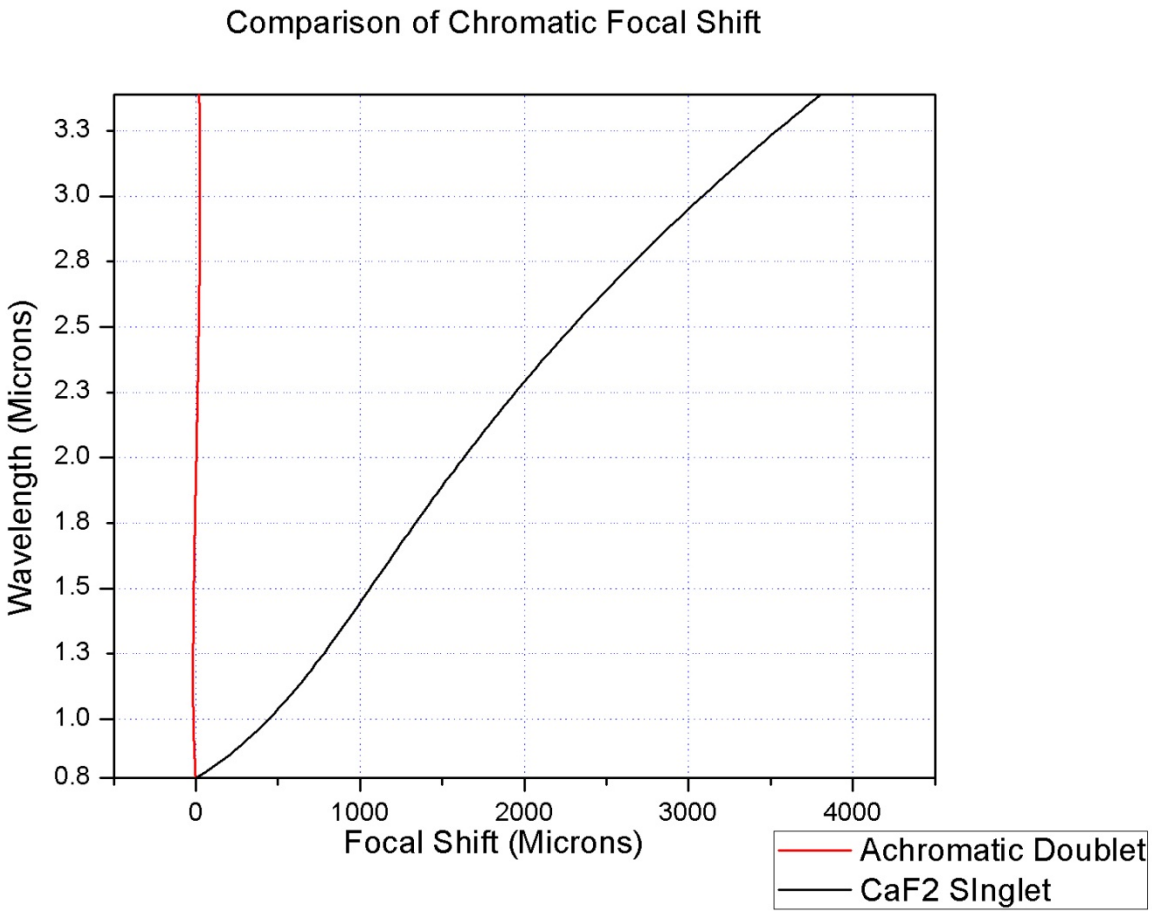

Figure 2.4: Comparison of chromatic focal shift. Performance of the achromatic doublet in red, calcium fluoride singlet in black.

The optimized design for the scan lens is shown below in Figure 2.5, while the surface details are listed in Table 2.5. This design was optimized for 7 different wavelengths that cover the possible VR-SFG wavelength tuning over the CH stretch range. It was optimized with 6 fields covering 0 to 4 degrees to account for the angled incident beams from the galvo mirrors; this is in excess of the actual scanning angles of ± 2 degrees that are actually necessary for the experimental setup. The performance of this lens is shown in Figures 2.6 through 2.9.

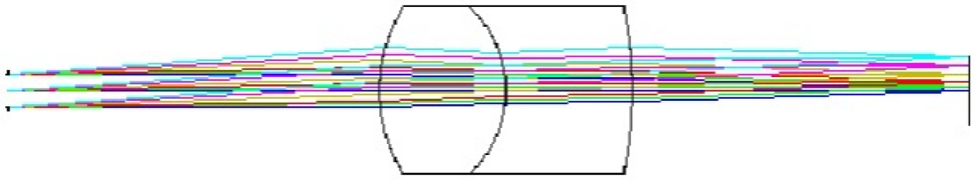

Figure 2.5: Layout for optimized scan lens design.

Table 2.5: Scan lens design surface parameters.

	Surf:Type	Comment	Radius		Thickness		Glass		Semi-Diameter		Conic
OBJ	Standard		Infinity		Infinity				Infinity		0.000
STO	Standard		Infinity		43.998				2.000		0.000
2*	Standard	front	18.546	V	15.000	V	CAF2		10.000	U	0.000
3*	Standard	middle	-13.602	V	15.003	V	MGO		10.000	U	0.000
4*	Standard	rear	-46.888	V	39.983				10.000	U	0.000
IMA	Standard		Infinity		-				4.018		0.000

The chromatic aberration of the achromatic scan lens design is shown in Figure 2.6. Similar to the comparison before in Figure 2.3, the chromatic aberration is limited to roughly 20 μm in the achromatic design. Figure 2.7 shows the Seidel diagram, where each column shows the general types of aberrations at each surface of the achromat. The total aberration from the lens will be a sum of the aberrations from each individual surface. It can be seen from the last column that the overall aberrations are well balanced out for this lens design. The aberration performance can be further observed in Figure 2.8, the spot diagram. Each of the six grids shows the focal point spot for a different field angle, and the seven wavelengths modeled are shown in different colors. It can be seen that for up to 2 degrees of field angle, the focal spot is well within the diffraction limited Airy radius. For 3- 4 degrees of field angle, the focal spot shows a little more distortion, however this is beyond the experimentally required angle.

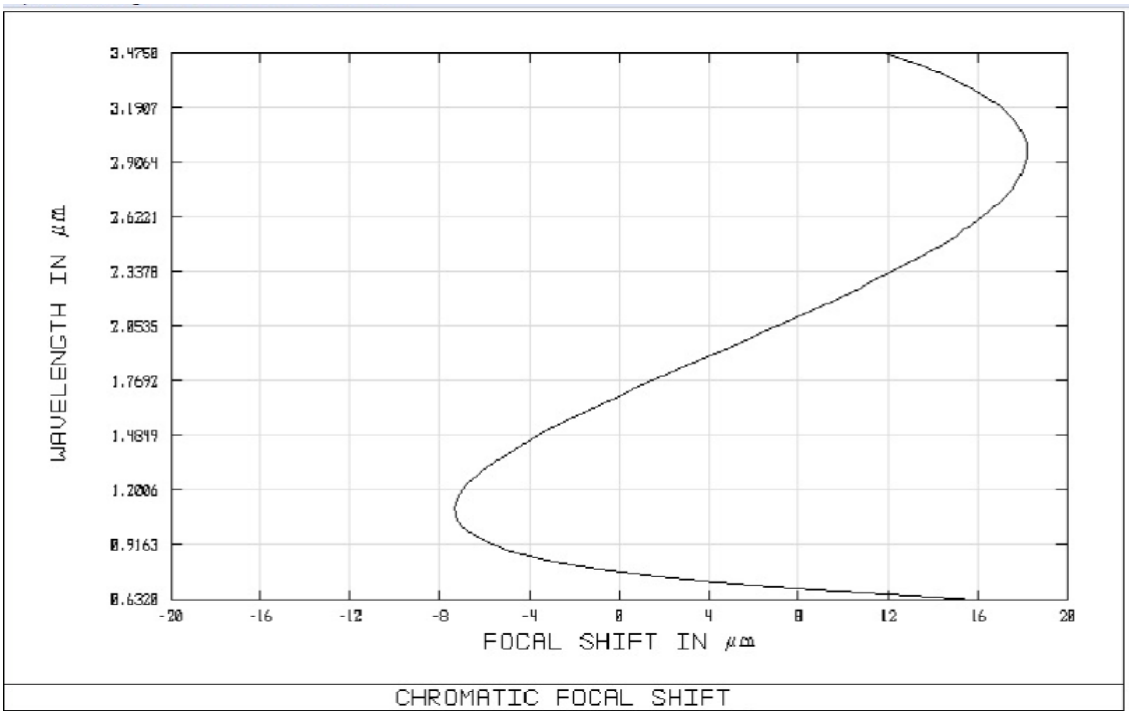

Figure 2.6: Chromatic focal shift for the optimized achromatic scan lens.

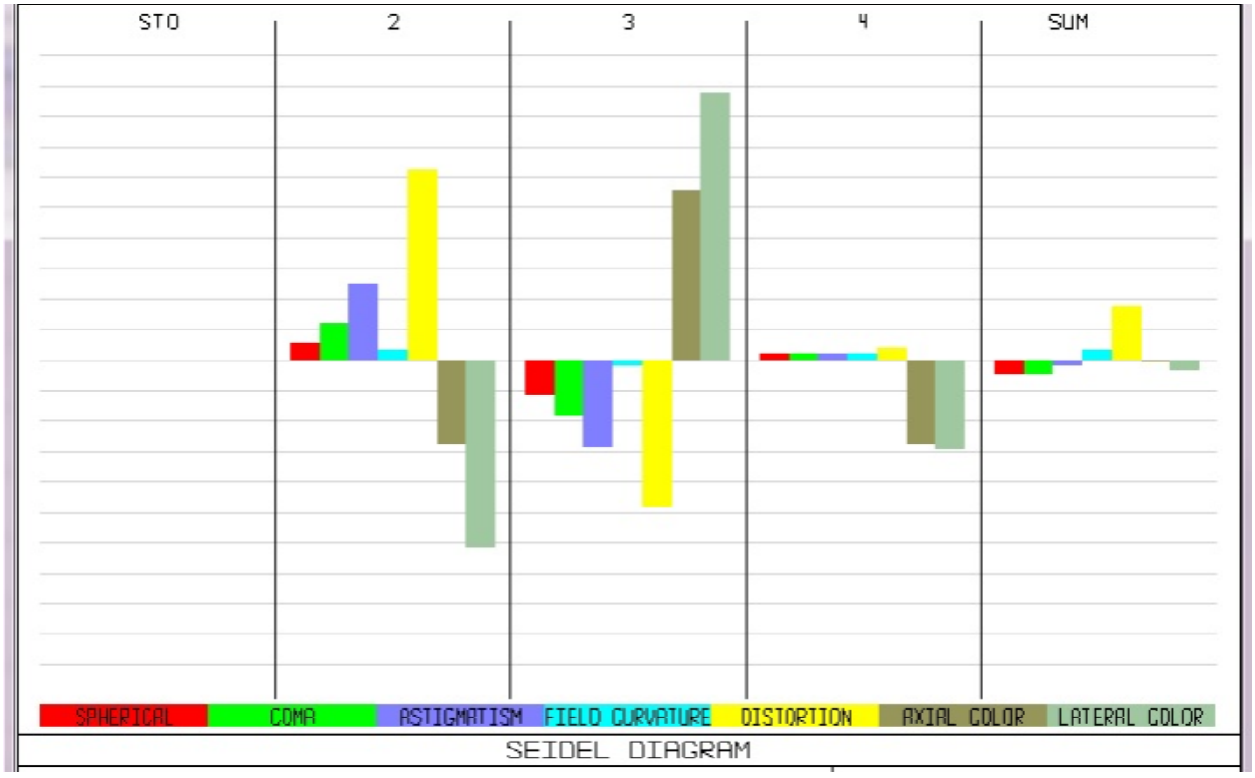

Figure 2.7: Seidel diagram showing the aberrations in the achromat. The last column shows the overall aberrations for the lens after the two elements balance each other out.

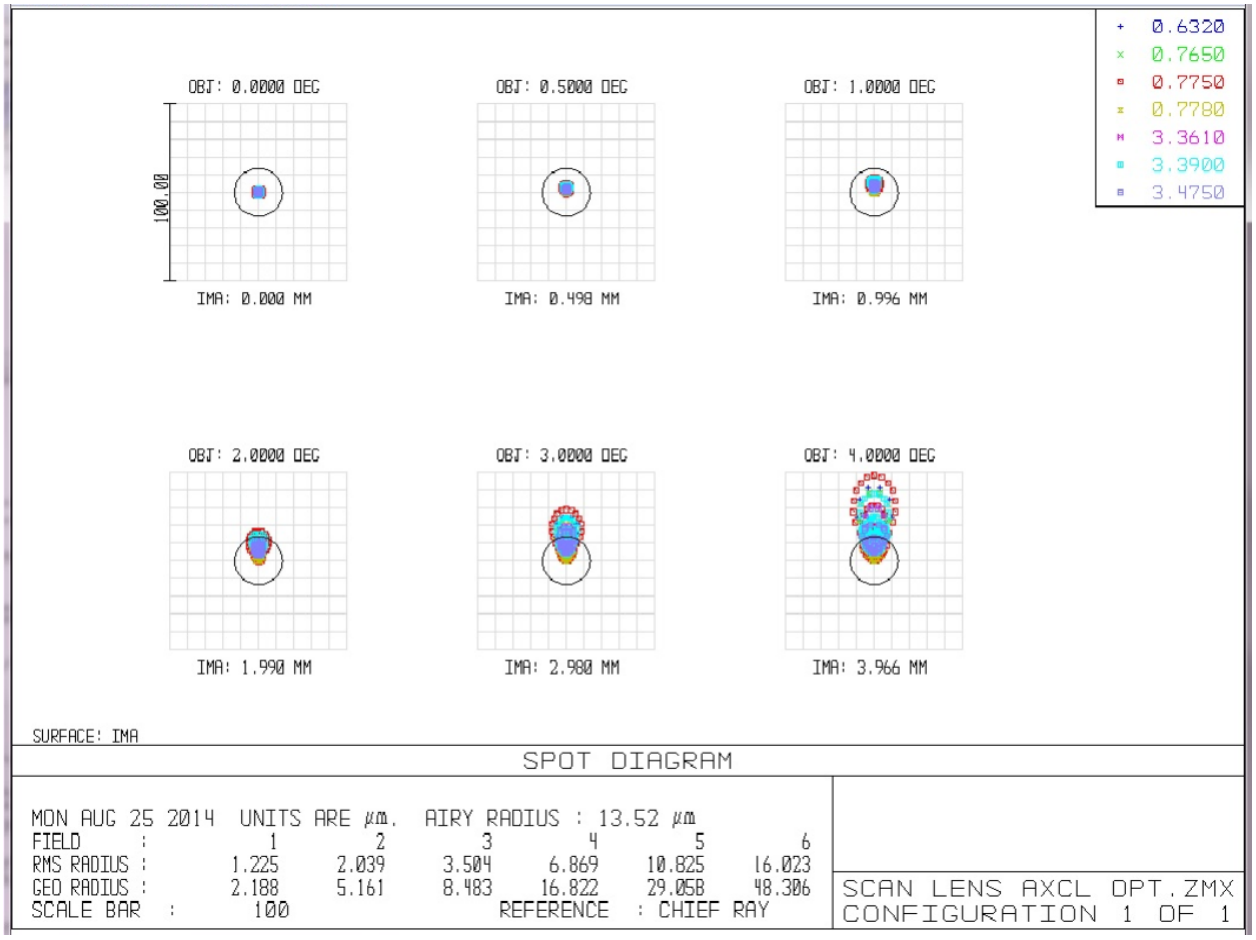

Figure 2.8: Spot diagram for the achromatic scan lens design. Each grid represent a different field angle, and the colors indicate the different wavelengths. The black circle is the calculated Airy radius.

The final measure of the performance of the lens is the Strehl ratio. The Strehl ratio varies between a value of 0 to 1, where a ratio of 1 indicates a system completely free of aberration. Based on , values of the Strehl ratio of 0.82 and above are acceptable. In Figure 2.9 it can be seen that the achromatic scan lens has Strehl ratios of 0.941 and 0.995 for 0.775 and 3.39 µm, respectively, at a 2 degree field angle. This is within the acceptable range and the lens design performance overall is much improved over non-corrected singlet lenses.

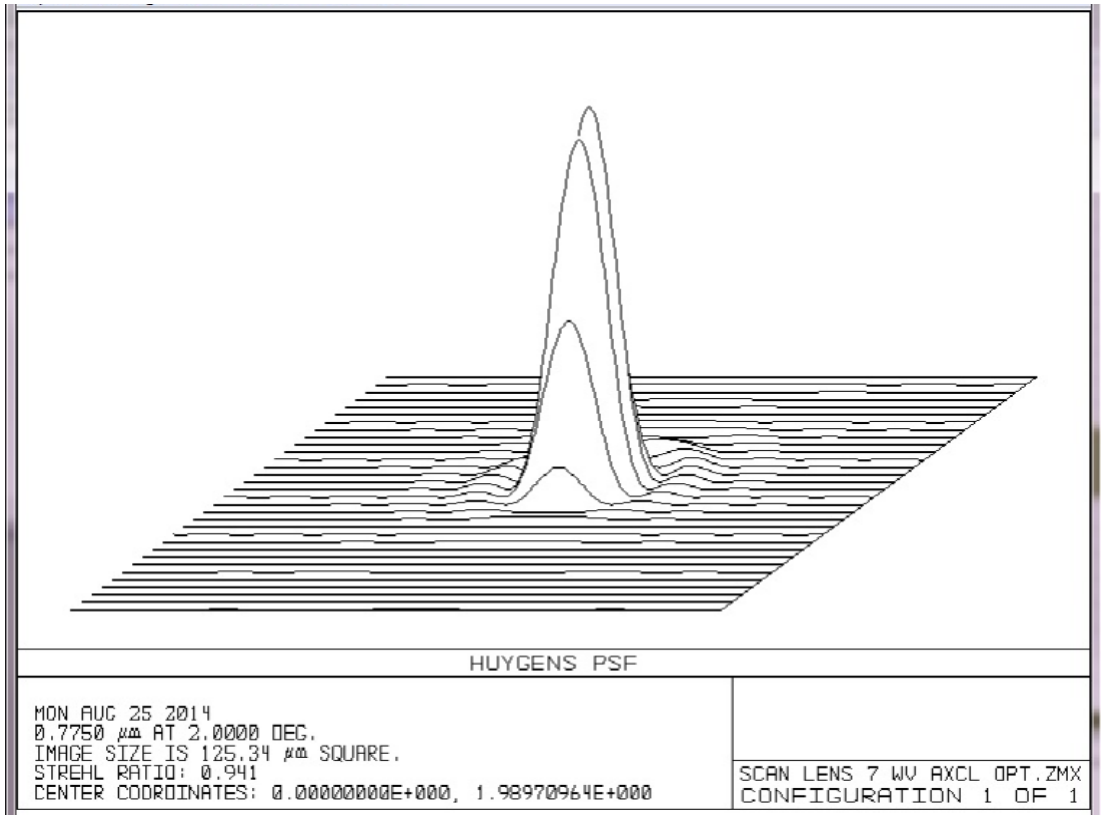

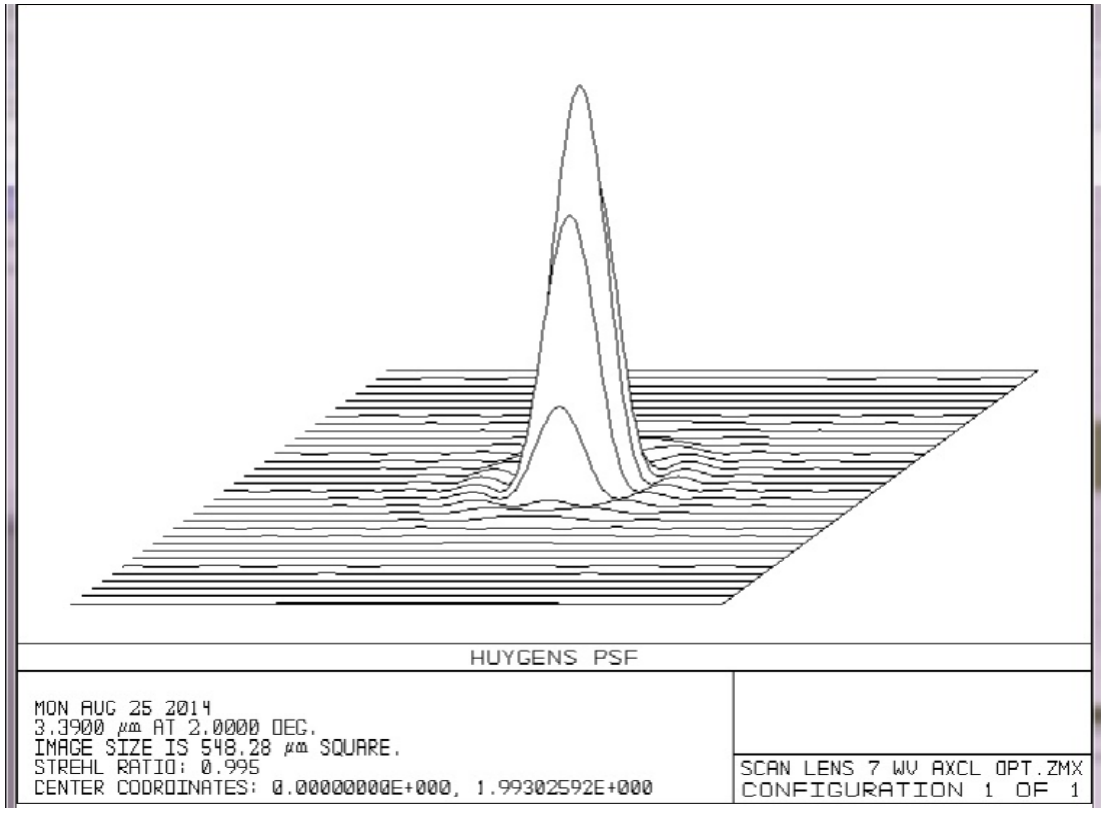

Figure 2.9: Point spread function and Strehl ratio at 0.775(top) and 3.39 µm(bottom).

A similar design and optimization was carried out for the tube lens, creating a design with effective focal length of approximately 135 nm. The layout of this achromatic tube lens is shown in Figure 2.10, while the surface parameters are listed in Table 2.6.

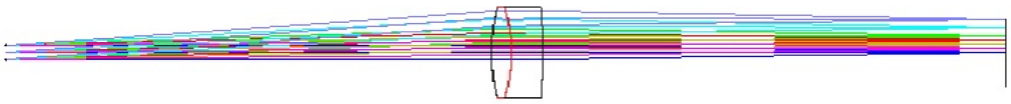

Figure 2.10: Layout of the achromatic tube lens.

Table 2.6: Surface parameters for achromatic tube lens design.

Surf	Type	Comment	Radius	Thickness		Glass		Semi-Diameter		Conic
OBJ	Standard		Infinity	Infinity				Infinity		0.000
STO	Standard		Infinity	135.000				2.000		0.000
2*	Standard	front	49.004	5.528		CAF2		12.700	U	0.000
3*	Standard	middle	-44.404	8.739		JULIESMGO		12.700	U	0.000
4*	Standard	rear	-136.534	128.915	V			12.700	U	0.000
IMA	Standard		Infinity	-				9.368		0.000

The performance of the tube lens was similarly satisfactory. Figure 2.11 shows the chromatic aberration of the tube lens design, where the chromatic aberration between the wavelengths of 0.775 and 3.39 µm is less than 40µm. This value is within the diffraction limited range for these wavelengths. Figure 2.12 shows to spot diagram for the tube lens. In this figure it can be readily seen the the focal spots for all field angles even up to 4 degrees are well within the limits of the Airy radius, and the different wavelengths are well overlapped. The overall performance of the scan lens and tube lens doublets are high and both offer a large improvement in terms of the chromatic aberration.

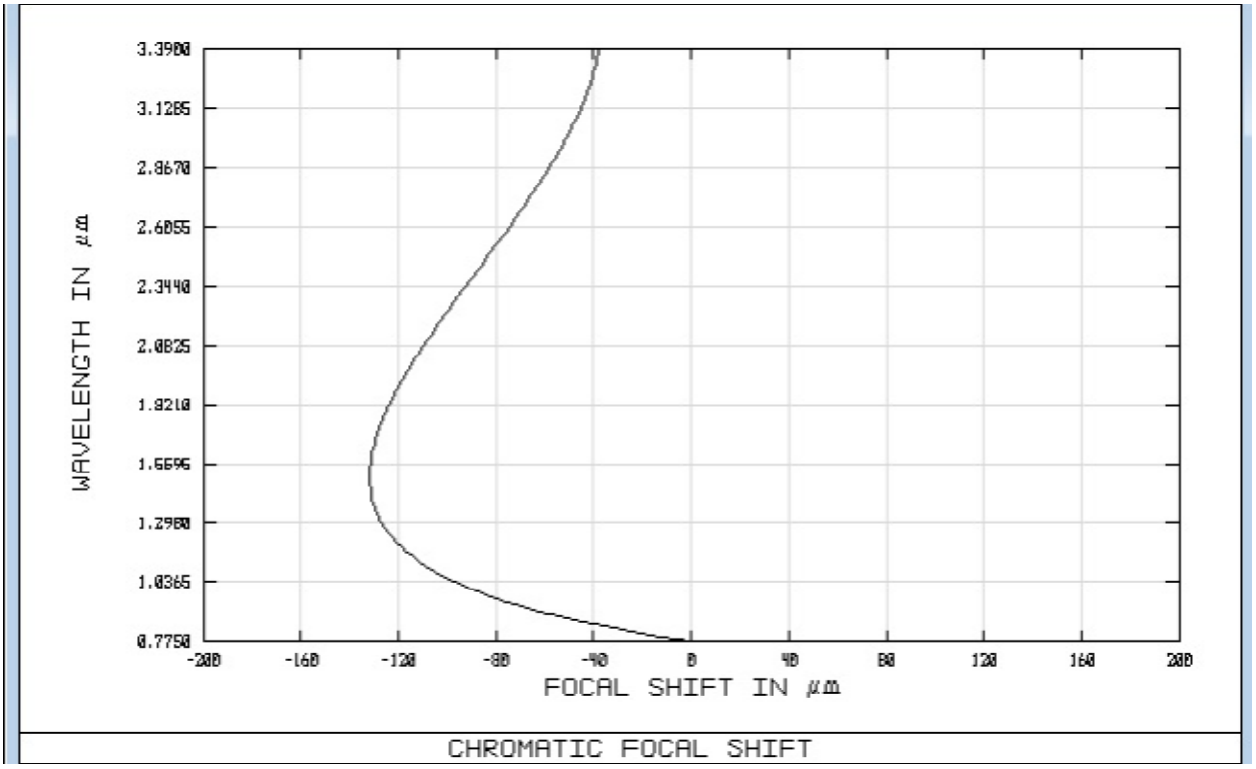

Figure 2.11: Chromatic focal shift of the achromat tube lens.

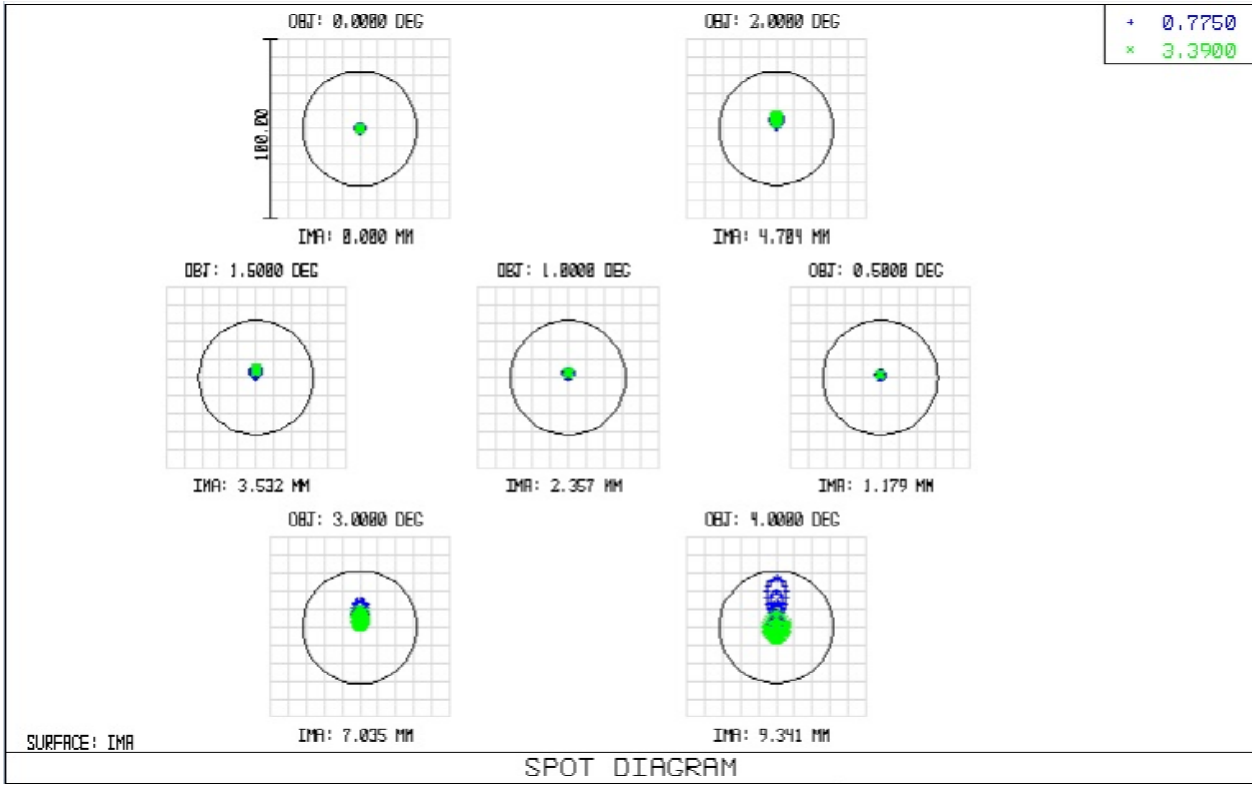

Figure 2.12: Spot diagram for the achromatic tube lens design.

Following the design and optimization of the scan lens and tube lens, a preliminary design for a refractive objective is shown below (Figure 2.13). The objective has approximately 0.5 NA, and consists of multiple elements from calcium fluoride and magnesium oxide material. Detailed parameters of each element are listed in Table 2.7.

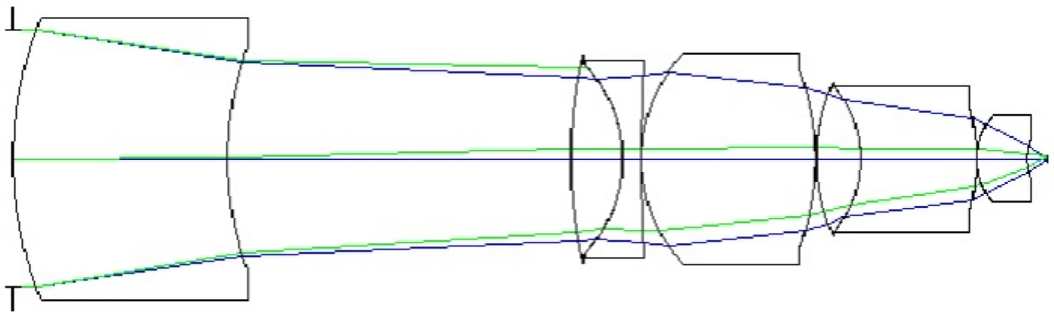

Figure 2.13: Layout of an achromatic refractive objective.

Table 2.7: Surface parameters of achromatic refractive objective.

Surf	Type	Comment	Radius		Thickness		Glass	Semi-Diameter	Conic
OBJ	Standard		Infinity		Infinity			Infinity	0.000
STO	Standard		Infinity		-9.112E-006			3.000	0.000
2	Standard		8.538	V	5.005	V	MGO	3.311	0.000
3	Standard		7.512	V	8.005	V		2.566	0.000
4	Standard	front 1	10.408	V	1.214	V	CAF2	2.428	0.000
5	Standard		-3.149	V	-4.936E-004	V		2.232	0.000
6	Standard	middle 1	-3.157	V	0.431	V	MGO	2.212	0.000
7	Standard	back 1	36.590	V	0.000			2.312	0.000
8	Standard		3.574		4.066		CAF2	2.450	0.000
9	Standard		-5.879		0.000			2.046	0.000
10	Standard	front 2	4.088		1.046		CAF2	1.796	0.000
11	Standard	middle 2	-2.653		2.706		MGO	1.717	0.000
12	Standard	back 2	-4.886		0.000			1.247	0.000
13	Standard	middle 3	1.540		1.166		MGO	1.017	0.000
14	Standard	back 3	1.115		0.491			0.434	0.000
IMA	Standard		Infinity		-			0.092	0.000

The performance of the objective is shown in Figures 2.14, 2.15, and 2.16. Figure 2.14 displays the chromatic focal shift of the refractive objective in the range of 0.775 and 3.39 μm, and the focal shift is less than 2 μm throughout the entire range of wavelengths. Figure 2.15 shows the modulation transfer function for the objective in for the wavelengths of 0.775 and 3.39 μm. The modulation transfer function(MTF) defines the response of a sine wave through the optical lens system for varying sine spatial frequency. The MTF is measured in cycles per millimeter, which can be converted to period in micrometers, thereby making the understanding of the MTF representing what the smallest feature the optical system is capable of spatially resolving more intuitive. Figure 2.15 shows that the objective lens performance is just slightly below diffraction limited performance, and the smallest feature that can be resolved at approximately 0.74 μm. Figure 2.16 shows the spot diagram, where the performance is close to diffraction limited.

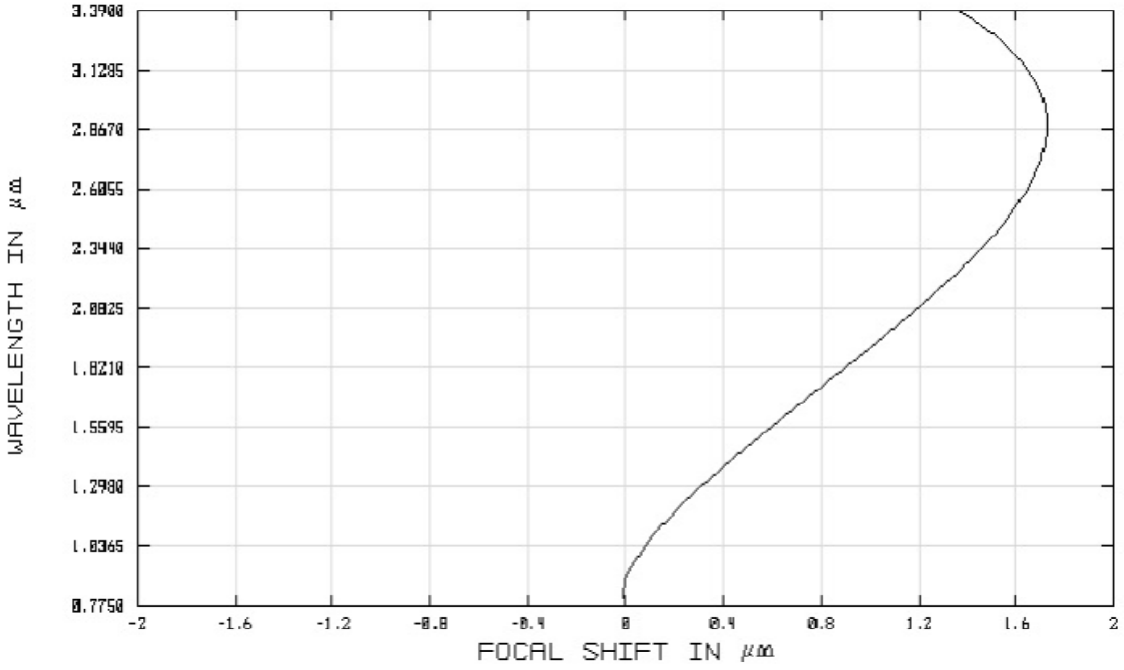

Figure 2.14: Chromatic focal shift of the refractive objective lens.

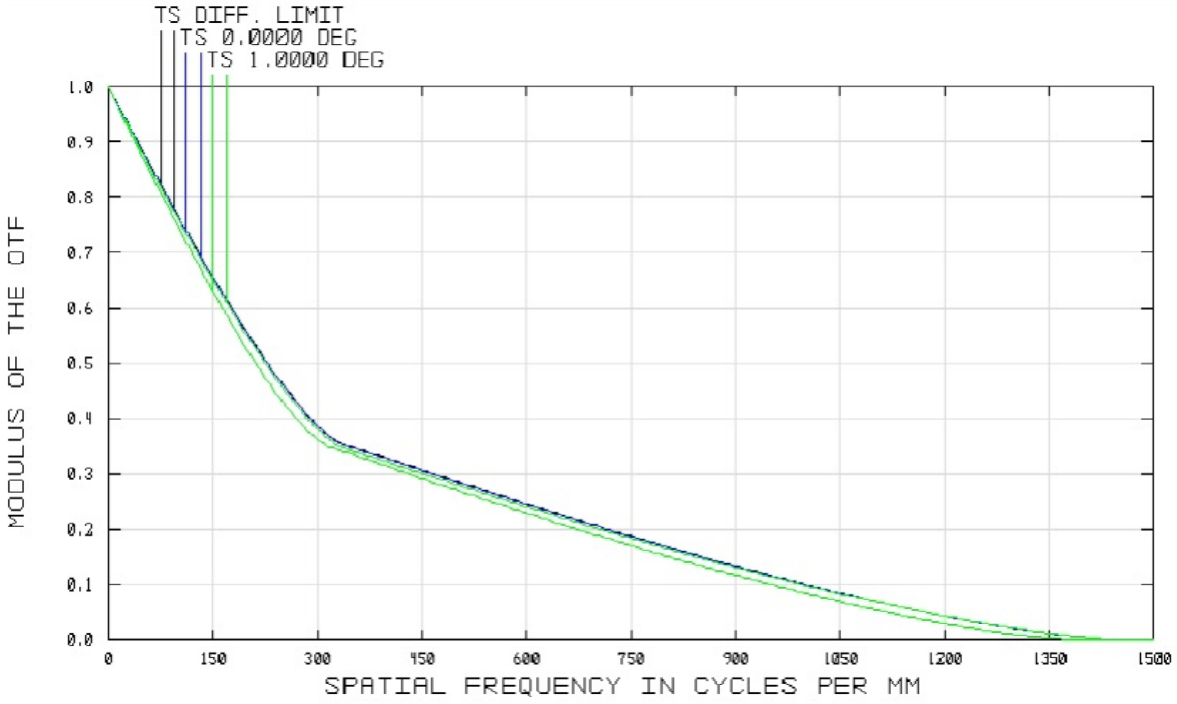

Figure 2.15: Modulation transfer function of the objective lens.

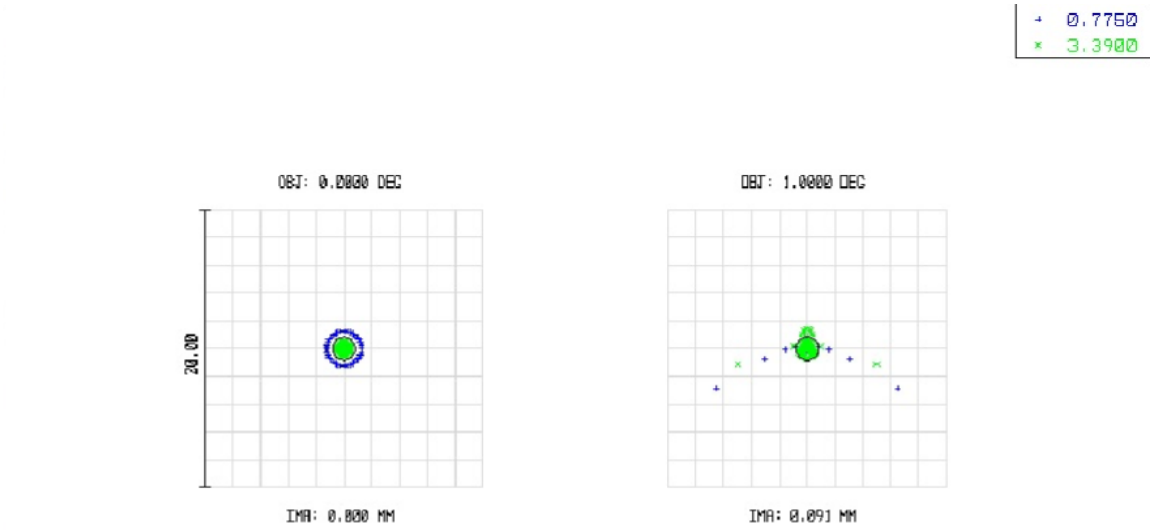

Figure 2.16: Spot diagram of the refractive objective lens.

2.4. Conclusion

The lens designs modeled demonstrate that implementation of achromatic refractive lenses into the VR-SFG microscope in order to improve its resolution and speed is feasible. Although there are no commercially available lenses capable of focusing near-IR and mid-IR simultaneously to the same point, the results have demonstrated that a custom design made from crystal materials available on the market is able to efficiently reduce chromatic aberrations and achieve high performance. The implementation of such lenses and a mirror galvanometer onto the VR-SFG microscope system would enhance its capabilities and improve its compatibility with other coherent nonlinear microscopy systems.

Chapter 3. Geometry Dependent Phase Shifts in Stimulated Raman Scattering

Position and geometry dependent phase shifts are a factor in stimulated Raman spectroscopy that affect the resulting spectral profiles. The position of a sample in the focus as well as the detection configuration can cause changes in the spectral shape that have not previously been examined in detail. A theoretical model for consideration of these spatial geometry effects is presented and compared with experimental data. This provides better understanding of these phase effects and how to set up an ideal configuration to minimize them.

3.1. Introduction

Stimulated Raman scattering uses a pump beam ω_p and Stokes beam ω_s to generate a third-order nonlinear signal at the same wavelength as the incident pump, ω_p. In a classical description what the detector measures can be considered an interference between the excitation pump field E_p and the induced dipole field. This is similar to a heterodyne detection: the excitation pump field is the local oscillator, and the phase difference between the interfering fields is determined by the sample response and experiment geometry.

Previous theoretical studies on how spatial setup of the experiment, including sample excitation as well as signal detection, affect spectra measurement have generally assumed homogeneous samples and plane wave excitation, thus fixing the spatial phase. However, in the case of single molecule spectroscopy, the induced dipole field is emitted from a single point and can not be assumed to be a plane wave. Similarly, in the case of stimulated Raman scattering microscopy, tightly focused excitation fields are used, and the plane wave excitation assumption also does not

apply [21]. Therefore, in the interest of characterizing the geometry dependent phase shift in stimulated Raman scattering microscopy, a theoretical description that takes spatial phase into account is necessary. The calculation provides a fundamental picture of how the electric fields involved in the SRS process change throughout focusing, dipole emitting, and propagating to the far field [22].

3.2. Theoretical Model

Stimulated Raman scattering signal can be described in the classical description as an interference mixing of the excitation field and the induced field at the detector. The total signal intensity detected at the detector from stimulated Raman scattering can then be expressed as:

$$\begin{aligned} S(\mathbf{R}) &= \frac{n(\omega_s)c}{8\pi}|E_s(\mathbf{R}) + E_{LO}(\mathbf{R})|^2 \\ &= I_s(\mathbf{R}) + I_{LO}(\mathbf{R}) + 2\frac{n(\omega_s)c}{8\pi}\,\mathrm{Re}\left\{E_s(\mathbf{R}) \cdot E_{LO}^*(\mathbf{R})\right\} \end{aligned} \tag{3.1}$$

where $\boldsymbol{S}(\mathbf{R})$ is the total signal intensity detected at a far-field point $\mathbf{R}$, $\boldsymbol{E_s}$ is the induced SRS signal field, $\boldsymbol{E_{LO}}$ is the incident excitation field acting as a local oscillator, $n(\omega_s)$ is the refractive index of the sample material at frequency ω_s, c is the speed of light in vacuum, and $\boldsymbol{I_s}$ and $\boldsymbol{I_{LO}}$ are the intensities of the induced signal field and incident excitation field, respectively. From this expression, it can be noted that the heterodyne term of the detected total signal is:

$$S_{het}(\mathbf{R}) = \frac{n\left(\omega_s\right)c}{4\pi}\,\mathrm{Re}\{E_s(\mathbf{R}) \cdot E_{LO}^*(\mathbf{R})\} \tag{3.2}$$

In order to evaluate this expression, it is necessary to formulate $E_s(R)$ and $E_{LO}(R)$ for SRS. In the case of stimulated Raman loss, as mentioned in Chapter 1.2, the induced polarization field at a point **r** of the sample can be expressed as:

$$P^{(3)}(\omega_1, \mathbf{r}) = \chi^{(3)}(\omega_1, \mathbf{r})|E_2(\mathbf{r})|^2 E_1(\mathbf{r}) \tag{3.3}$$

where in the case of stimulated Raman loss, E_1 is the incident pump field and E_2 is the incident Stokes field. Following the generation of the induced field at **r**, the field propagates to the detector at the far field location **R** with a phase shift Φ that is dependent upon the experimental geometry. The electric field at **R** can be related to the field at **r** by:

$$\widetilde{E}(\mathbf{R}, t) = E(\mathbf{r})e^{-i(\omega t + \Phi)} + c.c. \tag{3.4}$$

From these two equations, the heterodyne terms can be rewritten as:

$$E_s(\mathbf{R}) \propto P^{(3)}(\omega_1, \mathbf{r})e^{-i\varphi}$$

$$E_{LO}(\mathbf{R}) = E_1(\mathbf{R}) \approx E_1(\mathbf{r})e^{-i\alpha} \tag{3.5}$$

where φ and α represent the phase shift between **R** and **r** for the induced field and the excitation field, respectively.

The values of φ and α can be discussed for four separate scenarios:

1. Plane wave excitation of a thin homogeneous sample:

   The geometry of this scenario can be seen in Figure 3.1 a. The induced field generated by a sheet of dipoles at plane z has a phase shift of $\varphi = -1/2\ \pi$ [23]. The phase stays constant for plane wave excitation, so $\alpha = 0$. Therefore, these equations can be derived:

$$E_s(\mathbf{R}) \propto iP^{(3)}(\mathbf{r}) \tag{3.6}$$

$$S_{het}(\mathbf{R}) \propto -\operatorname{Im}\left\{P^{(3)}(\mathbf{r})E_{LO}^{*}(\mathbf{R})\right\} \tag{3.7}$$

$$S_{SRL}(\mathbf{R}) \propto -\operatorname{Im}\left\{\chi^{(3)}(\omega_1,\mathbf{r})|E_2(\mathbf{r})|^2 E_1(\mathbf{r})E_1^{*}(\mathbf{R})\right\} \tag{3.8}$$

$$S_{SRL}(\mathbf{R}) \propto -|E_2(\mathbf{r})|^2|E_1(\mathbf{r})|^2 \operatorname{Im}\left\{\chi^{(3)}(\omega_1,\mathbf{r})\right\} \tag{3.9}$$

This result indicates that the SRS signal is linearly proportional to the intensities of the pump beam and Stokes beam at the sample point **r**, and also reflects only the imaginary part of the third order susceptibility.

2. Plane wave excitation of a single dipole:

   For a single dipole (Figure 3.1 b), the induced field generated has a constant phase, and φ = 0. The excitation plane waves also have a constant phase, so α = 0. This leads to the equations:

$$E_s(\mathbf{R}) \propto P^{(3)}(\mathbf{r}) \tag{3.10}$$

$$S_{SRL}(\mathbf{R}) \propto |E_2(\mathbf{r})|^2|E_1(\mathbf{r})|^2 \operatorname{Re}\left\{\chi^{(3)}(\omega_1,\mathbf{r})\right\} \tag{3.11}$$

   In this scenario, the SRS signal is still linearly proportional to both excitation field intensities, but now is proportional to the real part of the third order susceptibility, creating diffusive line shapes.

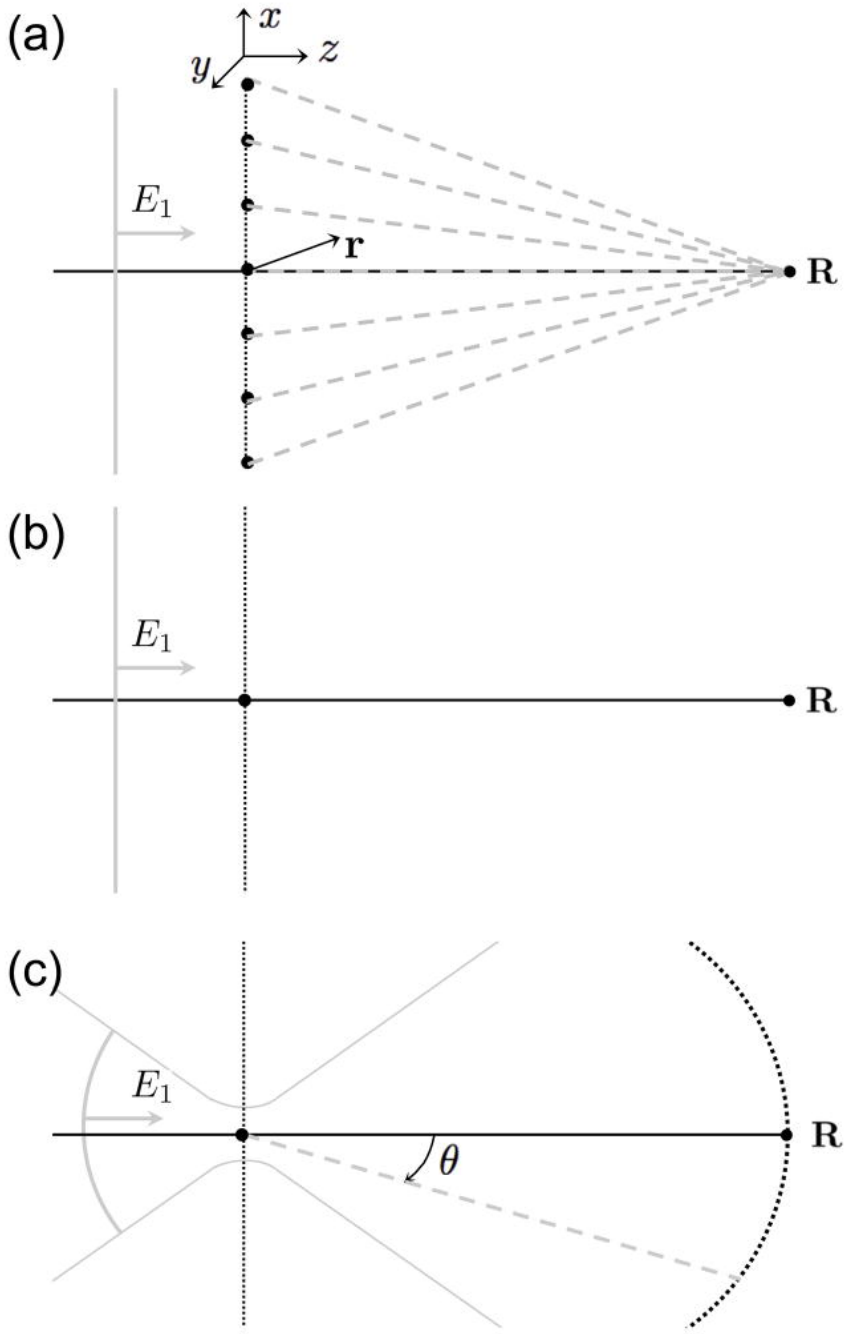

Figure 3.1: Three example geometries for stimulated Raman scattering. $\boldsymbol{E_1}$ is an incident excitation field, **r** indicates a sample position where the induced field is generated, and **R** is a far field point from where the signal is detected. a) Plane wave excitation of a thin layer of uniform dipoles indicated by black dots. The dashed lines indicate the propagation path for each dipole. b) Plane wave excitation of a single dipole. c) Focused beam excitation of a single dipole.

3. Focused beam excitation of a single dipole (in focal plane):

   For the single dipole, the phase shift φ = 0 again. However, the focused excitation field undergoes a Gouy phase shift of α = 1/2 π between **r** and **R** (Figure 3.1 c.) This gives the equation [21]:

$$S_{SRL}(\mathbf{R}) \propto -|E_2(\mathbf{r})|^2 |E_1(\mathbf{r})|^2 \operatorname{Im}\left\{\chi^{(3)}(\omega_1, \mathbf{r})\right\} \tag{3.12}$$

   where once again the signal is linearly proportional to the imaginary part of the third order susceptibility.

4. Focused beam excitation of a single dipole (out of focal plane):

   The single dipole generates an induced field with constant phase, φ = 0. However, the dipole position along the optical axis can be changed to create a different Gouy phase shift for α. This leads to the equation:

$$S_{SRL}(\mathbf{R}) \propto I_1(\mathbf{r}) I_2(\mathbf{r}) \left[\operatorname{Re}\left\{\chi^{(3)}(\omega_1, \mathbf{r})\right\} \cos\alpha(\mathbf{r}) - \operatorname{Im}\left\{\chi^{(3)}(\omega_1, \mathbf{r})\right\} \sin\alpha(\mathbf{r})\right] \tag{3.13}$$

   where it can be seen that the signal contains a position dependent phase shift and may contain real parts of the third order susceptibility for certain configurations (Figure 3.2.)

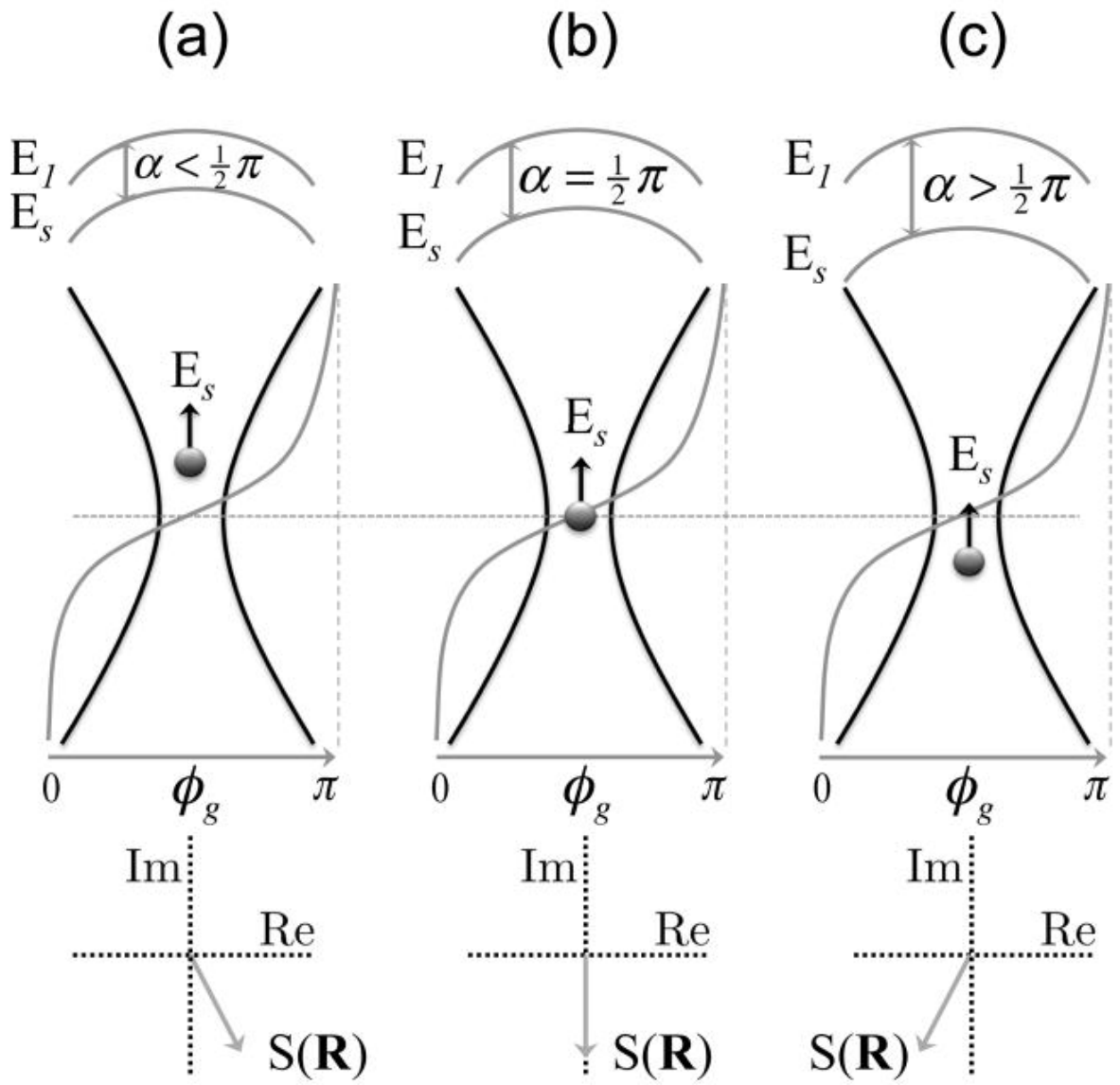

Figure 3.2: Position dependent phase shift. $\boldsymbol{E_1}$ is the incident excitation field, $\boldsymbol{E_s}$ is the induced field from interaction with the single dipole (black dot), the black lines show the focal volume, and the grey line shows the Gouy phase shift ϕ_g. The phase shift α between $\boldsymbol{E_s}$ and $\boldsymbol{E_1}$ is dependent on the position of the dipole. a) Dipole is above the focal plane, $\alpha < 1/2\ \pi$. b) Dipole is on the focal plane, $\alpha = 1/2\ \pi$. c) Dipole is below the focal plane, $\alpha > 1/2\ \pi$. Bottom plots show the phase of the SRS signal on the complex plane for each case.

3.3 Materials and Methods

Computational studies were calculated with Matlab (The Mathworks, Inc.) The program was based on vectoral focal field calculations where the the nonlinear polarization from a single dipole in the focal volume was approximated as a uniform voxel of 50 x 50 x 100 nm^3 according to Eq (3.3). The incident focused fields were calculated with diffraction theory, and the interference at the far field was calculated based on Eq (3.2) [24]. The program scanned through a range of pump beam wavelengths and calculated the intensity of SRL at the detector for each wavelength. It allowed selection of the sample location and NA of the collection lens, and graphed the fields at the focal plane and far field, as well as the final interference pattern. Incoming beams were assumed to be Gaussian, mode 0, and X-polarized. The resonant wavelength was assumed to be at 800 nm, and the pump was varied around that center value. The Stokes wavelength was assumed to be 1064 nm. The objective lens was assumed to be a water lens with NA=1.2. Four types of collection lenses were modeled: 1) air lens with NA=0.9, 2) air lens with NA=1.2, 3) water lens with NA=1.2, and 4) water lens with NA=1.33. The vibrational resonance of $\chi^{(3)}$ was approximated as a Lorentzian curve with a 5 cm^{-1} linewidth.

Stimulated Raman scattering experiments were performed with a coherent Raman scattering microscope described previously [25]. A 532 nm, 7 ps, 76 MHz Nd:vanadate laser from Picotrain, High Q was used to pump an optical parametric oscillator (OPO, Levante) to generate the excitation beams. The Stokes beam was fixed at 1064 nm while the pump beam was tuned within the 795 - 811 nm range. The pump beam was modulated at 10 MHz with an acoustic optical modulator (Crystal Technology). The pump and Stokes beam were overlapped on a dichroic beam combiner, sent into a laser scanner (Fluoview 300, Olympus), and then a Olympus

IX71 inverted microscope. A 60X, 1.2 NA, water-immersion objective lens was used for sample illumination, and a 0.9 NA condenser was used for signal collection. The signal was detected with a photodiode (FDS1010, Thorlabs) and demodulated with a home-built lock-in amplifier. Hyperspectral SRS imaging was achieved through software controlled adjustment of several OPO parameters. A z-axis controller (MFC-2000, Applied Scientific Instrumentation) coupled with a 635 nm diode laser interferometer was used for stabilizing the sample position.

Samples were 0.47 micron polystyrene beads from Polysciences Inc. mixed with agarose gel and fixed on a glass slide.

3.4. Results and Discussion

The computational study modeled the SRS signal for different axial positions of the single dipole with different detection configurations. Figure 3.3 shows the modeling of the focused electric fields at the focal plane. After propagation to the far-field, the interference pattern at the collection lens for on-resonance SRS signal is illustrated in Figure 3.4 [22]. Comparisons are made for the dipole being above the focal plane, on the focal plane, and below the focal plane (Figure 3.4 a.) It can be seen that when the dipole is on the focal plane, the interference pattern shows completely negative signal, indicating loss of the pump beam intensity in agreement with the quantum molecular picture of SRS. However, off of the focal plane, the interference pattern displays positive signal at the edges of the detector, seemingly in contradiction with the quantum molecular description. According to the quantum model, the sample molecule is initially in the ground state, then interacts with the pump beam (absorbs), and emits at the Stokes frequency to arrive at a vibrationally excited state. In this description SRL should always be positive

(meaning a loss for the pump,) and it should be impossible for the beam to gain photons from the sample.

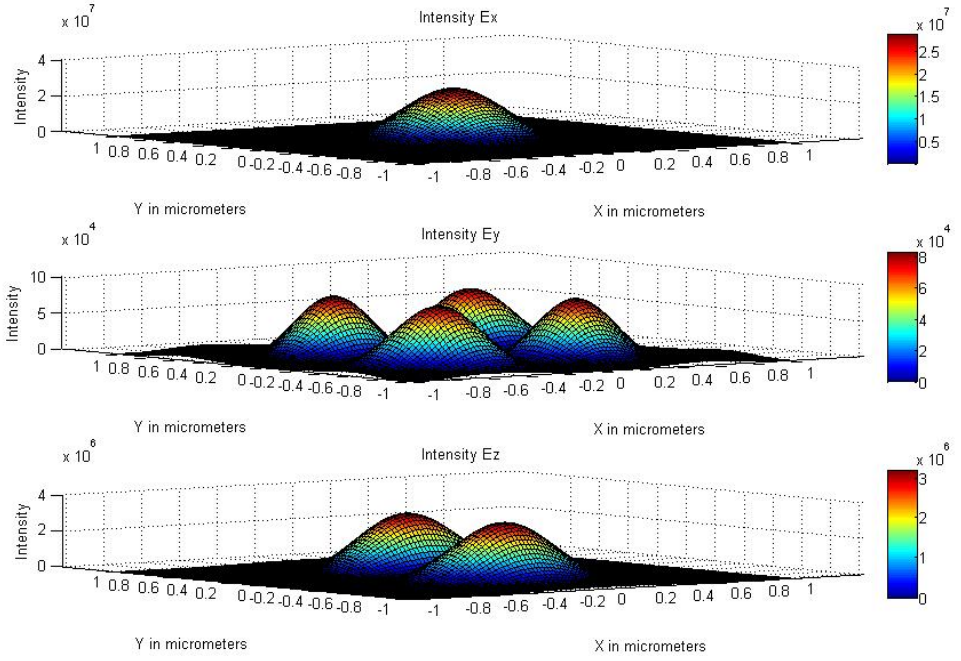

Figure 3.3: Incident electrical fields at the focal plane. The three components of the electrical field at the focal plane were computed. Polarization of incident fields is assumed to be in the x-axis, so the fields are not radially symmetric.

This seeming inconsistency between computed results from a classical wave mechanics model and quantum mechanical model can be explained by comparison of Figure 3.4 b and c, where detected spectra shapes for collection lens of NA=0.9 and NA=1.2 are shown, respectively. For the NA=0.9 lens (Figure 3.4 b), when the dipole is in the focal plane, the signal is proportional to the imaginary part of the nonlinear susceptibility (Eq 3.12), and the lineshape is absorptive. When the dipole is above or below the focal plane, the real part of the nonlinear susceptibility also contributes to the signal, and a dispersive lineshape is observed, pointing to the seeming gain in pump signal also present in Figure 3.4 a. However, upon inspection of Figure 3.4 c,

where the collection lens is assumed to encompass the entire hemisphere (NA=1.2), all lineshapes are Lorentzian regardless of the position of the dipole in the focal volume.

The above results can be explained by considering that the pump beam propagates to the far field with a Gouy phase-shift and mixes with the induced field to generate a SRS interference signal that is not spatially uniform. Therefore, although there is overall destructive interference with the dipole field, the detected signal may be positive if the collection lens is not large enough to receive all forward signals. Once the detection aperture is large enough to capture the full interference signal, then there is no inconsistency between the molecular energy level picture and the wave mechanics picture; either one predicts a loss for the pump beam regardless of sample location and pump wavelength.

Similar results as the above are observed for collection with water immersion lenses of NA=1.2W and NA=1.33W. In Figure 3.5, the dipole induced field is plotted at the far field for a NA=1.2 incomplete collection (Figure 3.5 a) and a NA=1.33 full hemisphere collection (Figure 3.5 b.) The interference at the far field with the pump field is similar to the air collection shown in Figure 3.4. Computed spectra also show that the spectral lineshapes are purely absorptive when the dipole is in the focal plane, but dispersive when the dipole is out of the focal plane.

The geometry based phase shifts were also confirmed experimentally. Figure 3.6 shows the experimental SRL spectra for 0.47 μm polystyrene beads' vinyl stretching vibration. The polystyrene SRL spectrum changes depending on the position along the optical axis, where a bead below the focal plane gives a negative dip on the low energy side of the spectrum and a bead above the focal plane gives a dip on the high energy side. These are in agreement with the computational results.

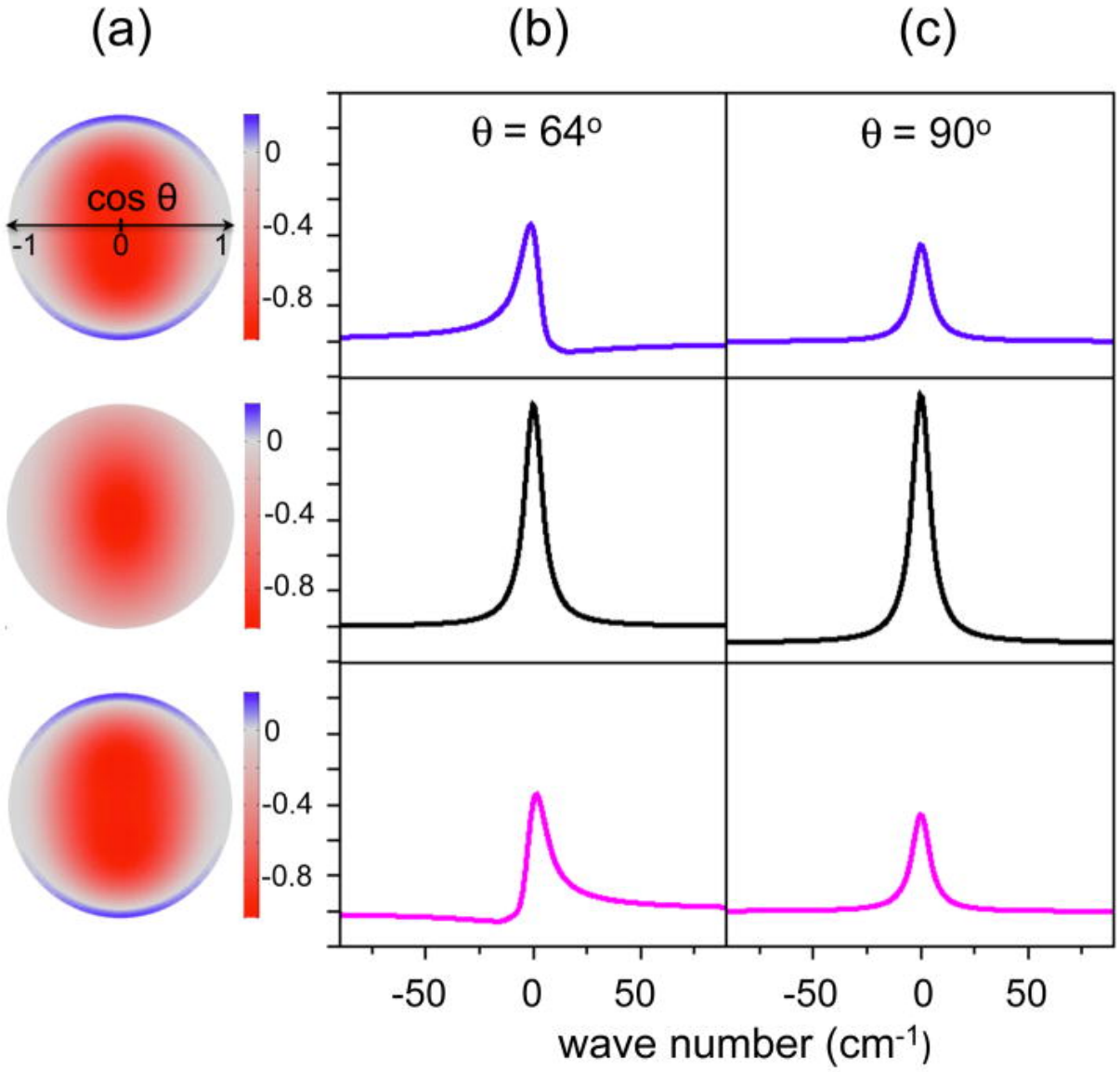

Figure 3.4: Calculation of the detected SRL signal for different configurations. a) Far-field interference pattern when the dipole is 0.5 μm above the focal plane (top), at the focal plane (middle), and 0.5 μm below the focal plane (bottom). b) SRL spectra with collection NA=0.9 for the three dipole positions. c) SRL spectra with a full hemisphere detection, NA=1.2.

a

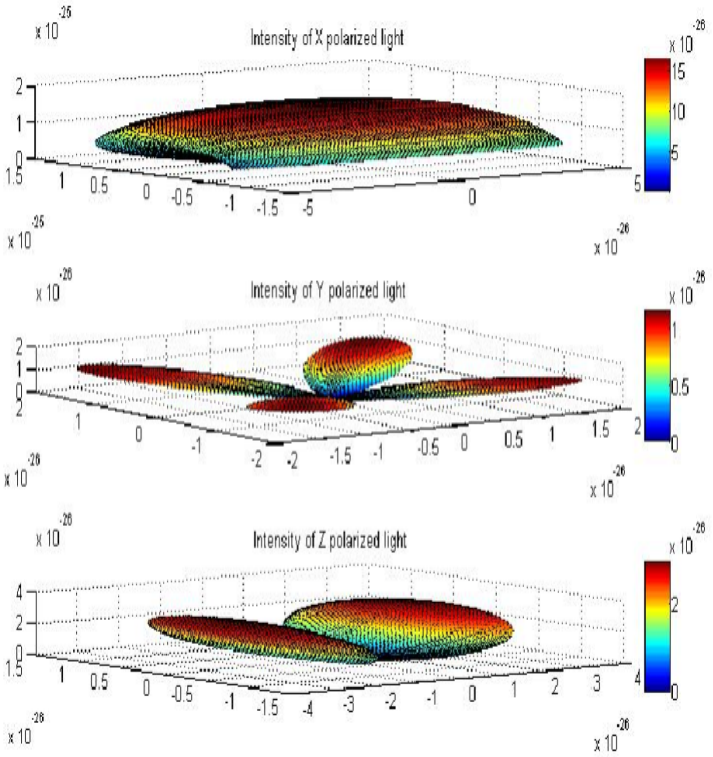

b

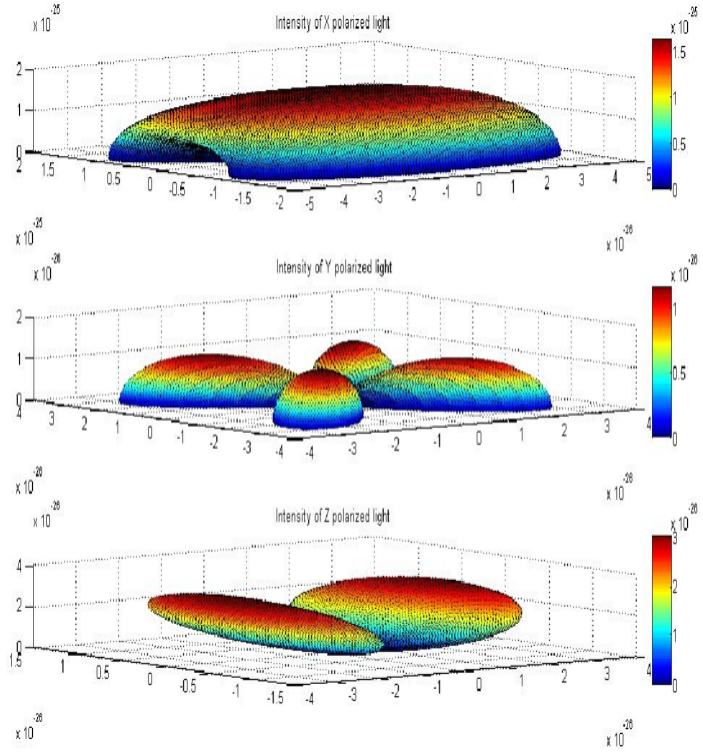

Figure 3.5: Dipole induced fields propagated to the far field. a) The components of the dipole induced field detected with NA=1.2 W. b) The induced field with full detection NA=1.33 W.

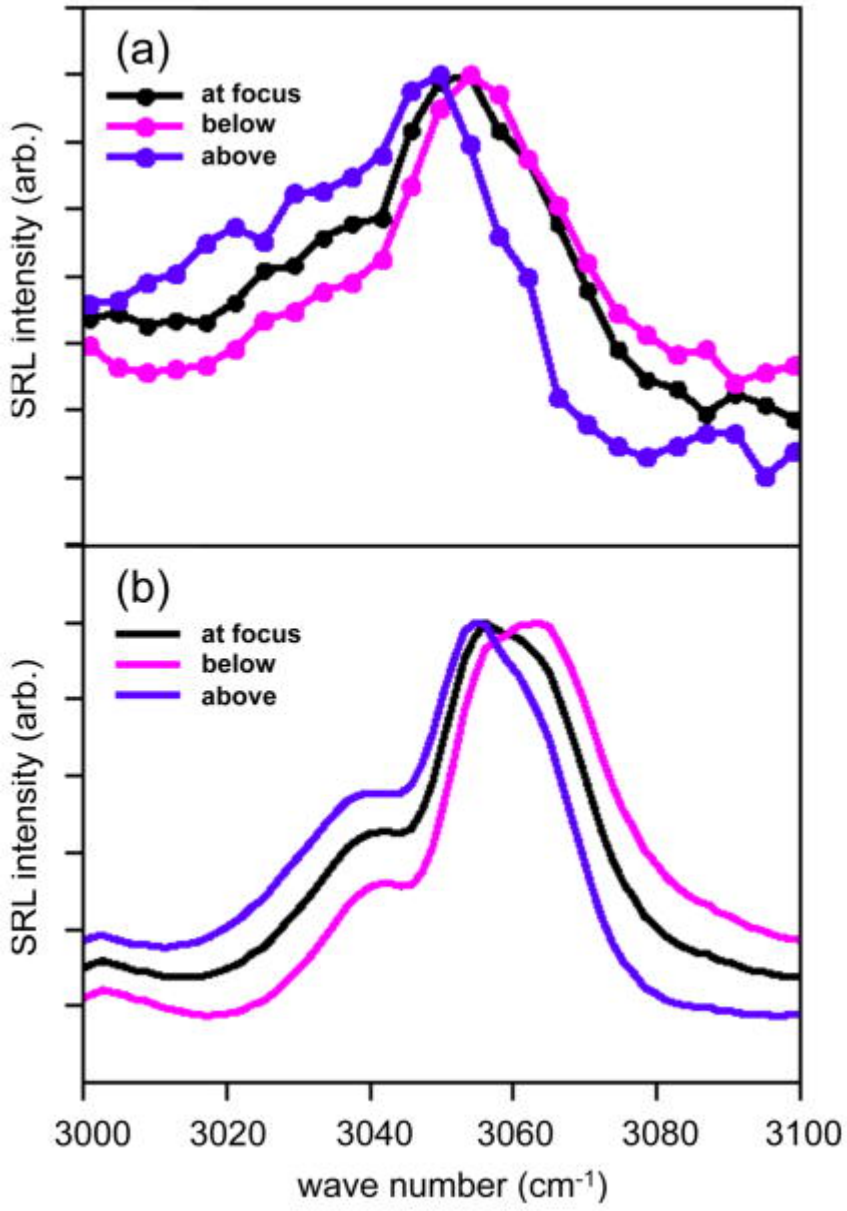

Figure 3.6: Experimental spectra of polystyrene beads with different position dependent phase shifts. a) Experimental SRL spectra for particle 1 micron below the focal plane (pink), on the focal plane (black), and 1 micron above the focal plane (blue). b) Calculated SRL spectra based on a Kramers Kronig transformation of the polystyrene Raman spectrum and various phase shifts. Phase shifts: $\alpha = 70°$ (red), $\alpha = 90°$ (black) and $\alpha = 110°$ (blue).

3.4. Conclusion

The calculations and experimental measurements confirm that sub-wavelength particles are sensitive to the effects of position dependent phase shifts in a stimulated Raman scattering

microscopy measurement. These geometry related phase shifts are reflected on the lineshapes of the spectra. The most optimal configuration for minimizing these effects is for the sample particle to be right on the focal plane and for the collection aperture to be large. The theoretical calculations outline a model for evaluating the geometry and position dependent phase shifts in future stimulated Raman scattering microscopy measurements where the configuration is different from what is described above.

Chapter 4. Sum Frequency Generation Microscopy of Collagen

Vibrationally-resonant sum frequency generation microscopy is an ideal technique for imaging molecules with noncentrosymmetry to clarify the link between the optical signal and the chemical moiety responsible for the second-order molecular response. The unique symmetry sensitive characteristics of SFG have made it a popular spectroscopy technique, but due to technical limitations, it has not been widely used as a microscopy technique. Our research group assembled a microscope for the simultaneous acquisition of nonresonant SHG and vibrationally resonant SFG signals. This VR-SFG microscope has the potential to combine the ability of infrared spectroscopy chemical specificity with the ability of coherent nonlinear imaging to obtain fast, high resolution, and three-dimensional images with no labeling and minimal sample damage. The microscope allows for imaging noncentrosymmetric molecules such as collagen with high speed and resolution and provides information about molecule orientation on a sub-micrometer scale. The microscope was utilized to take polarization sensitive measurements as a function of vibrational energy of collagen. These measurements have provided insight on the molecular modes contributing to collagen sum frequency signal as well as the off resonance contributions to collagen second harmonic signal.

4.1 Collagen

The most abundant protein in the human body, collagen is an ideal study subject for sum frequency generation due to its noncentrosymmetric nature [26]. Collagen has many important biological roles, some of which are areas of high interest in current medical research (e.g. wound

healing.) Of the multiple types of collagen, type I is the most common and is present in skin, tendon, cornea, and connective tissue. Molecularly, collagen peptides have been shown to have many repetitive GPX or GX-Hyp units, where G is glycine, P is proline, Hyp is hydroxyproline, and X is a random amino acid. The peptide is commonly about 1000 amino acids in length, and referred to as a propeptide. Three propeptides will twist together to form the α-helical tropocollagen. Structurally, type I collagen is composed of α-helical tropocollagen assembled into microfibrils, which then pack into fibrils [27]. These fibrils then align in a parallel or antiparallel fashion to produce collagen fibers and lamellae. The structural ordering of these fibrils determines the vastly differing properties of the various types of collagen tissue [28]. The intrinsic lack of inversion symmetry and unique long axis of the collagen molecule has allowed second order nonlinear techniques such as SHG and SFG to image individual fibril orientation with high resolution.

Although the second-order nonlinear method of second harmonic generation (SHG) microscopy has been previously used to study collagen, it is unclear what the origin of the second order nonlinear signal is [29]. SHG has the advantages of fast imaging, high spatial resolution, and selectivity to noncentrosymmetric molecular ordering, but its signal is nonresonant, making it difficult to interpret any links between the optical signal and the chemical modes responsible for the second-order molecular response. Previous studies using SHG have pointed to either the amide group of the peptide bond or the methylene groups of proline as the main source of second-order signal for collagen, yet there is no clear evidence to support this [30, 31]. In contrast, VR-SFG can be tuned into direct resonance with collagen vibrational modes to provide nonlinear signal with no background. Simultaneous measurement of nonresonant SHG

and vibrationally resonant SFG signals with the VR-SFG microscope is carried out in an effort to clarify the chemical origins of the contrast seen in second-order nonlinear imaging of collagen.

4.2. Microscope Setup and Materials

The VR-SFG microscope (Figure 4.1) consists of an optical parametric oscillator (Levante, APE) powered by a 1064 nm, 76 MHz, 7 picosecond pulsed laser (Picotrain, High Q) to produce two synchronized laser beams of ω_1 in the mid-infrared region (2835 to 2970 cm^{-1}) and ω_2 in the near-infrared (765-850 nm). The polarizations two beams were individually controlled with polarizers and half-wave plates. The mid-infrared beam used a BaF_2 wire-grid polarizer (extinction ratio 150:1 at 3300 cm^{-1}) and the near-infrared beam used a SF2 polarizer (extinction ratio 1000:1). The two beams were collinearly combined with a YAG-based dichroic beam combiner and sent to a Olympus IX-71 inverted microscope. The microscope contained a CaF_2 lens and the objective was a 0.65 NA, 74x reflective objective (Edmund Optics). Sample scanning was done in a raster point-scan manner with a two dimensional piezo stage (Madcity Labs) where the sample moved relative to the incident beam. The generated signal was detected in the forward direction with a refractive condenser lens, an analyzer, three 632± 20 nm bandpass filters, and a photomultiplier tube (Hamamatsu). This setup allows tight focusing of the beam without significant sample damage as well as molecular resonance with ω_1 while the signal can be detected in the 625-650 nm visible range. The setup also allows for detection of the SHG signal generated by ω_2 by simply changing to appropriate detection bandpass filters. Tuning of the wavelength was performed by adjusting the temperatures of the PPLN and LBO crystals and cavity length in the OPO.

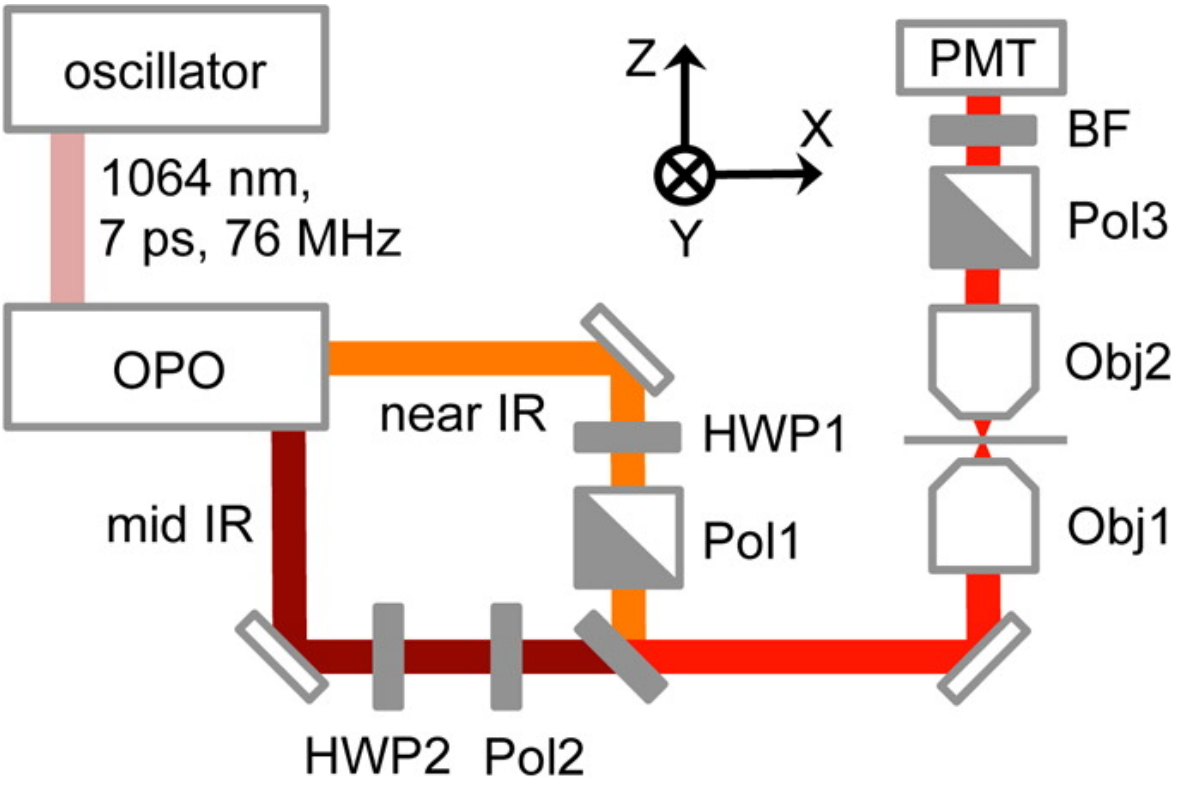

Figure 4.1: Sum frequency generation microscope setup.

Collagen samples were obtained from rat tail tendons and hawk eye corneas. The rat tail tendon was sliced into 100 μm thick strands and flattened between two glass coverslips. The hawk eye cornea was a 100 μm thick sagittal slice provided by Prof. James Jester, Department of Opthalmology, UCI. The slice was placed on a glass coverslip and immersed in phosphate buffered saline.

4.3 Polarization Sensitive SFG and Collagen Second Order Nonlinear Susceptibility

The second order induced polarization in sum frequency generation can be generally expressed as [4]:

$$P^{(2)}_i = \chi^{(2)}_{ijk} E_j E_k \tag{4.1}$$

where the incident electric fields and induced polarization are vectors, and therefore the susceptibility $\chi^{(2)}$ is a rank 3 tensor with 27 elements. In polarization sensitive SFG, different combinations of settings for the polarization directions of the ω_3, ω_2, ω_1 fields allow for probing of different individual elements of the $\chi^{(2)}$ tensor. These tensor elements can then be related back to the hyperpolarizability of chemical groups and their orientations through rotations of the coordinate frame and applying symmetry properties.

In order to understand the relationship between the polarization sensitive SFG signal measured and collagen hyperpolarizability elements, consistent coordinate frames for the laboratory frame and collagen frame must be defined. This is shown in Figure 4.2, where the laboratory frame has axes (*X,Y,Z*) and the collagen frame has axes (*x,y,z*). In the laboratory frame, (*X,Y*) forms the lateral plane where the sample stage moves, and *Z* forms the vertical optical axis. For the collagen molecule, it can be assumed to have a $C_{\infty v}$ point group symmetry where it has a single long axis *y* and is cylindrically symmetric around it [7]. For such a point group, based on Neumann's principle, there are 7 nonzero achiral second order susceptibility tensor elements

$(\chi_{yyy}^{(2)}, \chi_{yzz}^{(2)} = \chi_{yxx}^{(2)}, \chi_{zzy}^{(2)} = \chi_{xxy}^{(2)}, \chi_{zyz}^{(2)} = \chi_{xyx}^{(2)})$ and 6 nonzero chiral tensor elements

$(\chi_{zxy}^{(2)} = -\chi_{xzy}^{(2)}, \chi_{xyz}^{(2)} = -\chi_{zyx}^{(2)}, \chi_{yzx}^{(2)} = -\chi_{yxz}^{(2)})$.

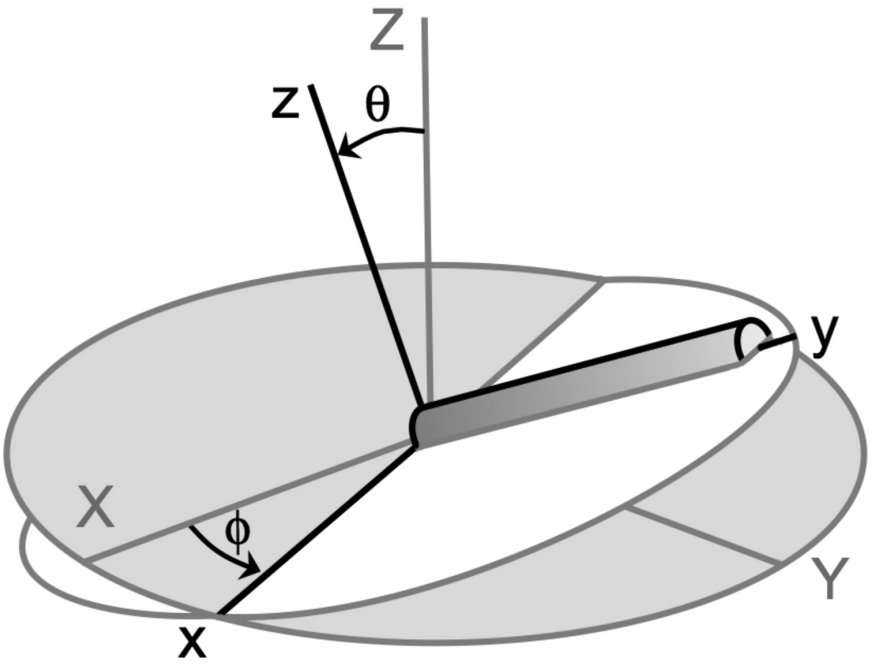

Figure 4.2: Coordinate frames for the laboratory frame (*X,Y,Z*) and collagen frame (*x,y,z*). ϕ indicates a rotation of the fiber around *Z*, and θ indicates a rotation around *x*. Rotations are in a clockwise fashion following the right-hand rule.

Experimentally the incident excitation beams are either polarized in *X* or in *Y*, then combined and sent to the microscope. The sample collagen fiber is laid out in the (*X,Y*) plane and rotated around the central optical axis, creating different ϕ angles but a constant $\theta = 0$. The rotation of the sample is preferable to other variations of polarization settings as they lead to elliptical polarization arising from the optical components of the setup. The polarization of the incident beams is linear with less than 1% error right before the objective lens, and the amount of

polarization in the *Z* axis generated from the 0.65 NA objective is negligible as well. Under these conditions, the collagen nonzero susceptibility tensor elements can be related to the measured SFG polarization elements through a rotation matrix $\mathbf{R}_z$:

$$\begin{pmatrix} \cos\phi & -\sin\phi & 0 \\ \sin\phi & \cos\phi & 0 \\ 0 & 0 & 1 \end{pmatrix}$$

The rotation matrix is applied in the following way:

$$\chi^{(2)}_{IJK} = \sum_{ijk} R_{Ii} R_{Jj} R_{Kk} \chi^{(2)}_{ijk} \tag{4.2}$$

The calculation gives four relevant tensor elements in the laboratory frame with the assumption that there is no *z* component:

$$\chi^{(2)}_{YYY} = \chi^{(2)}_{yyy}\cos^3\phi + (\chi^{(2)}_{xyx} + \chi^{(2)}_{yxx} + \chi^{(2)}_{xxy})\sin^2\phi\cos\phi + \chi^{(2)}_{xxx}\sin^3\phi + (\chi^{(2)}_{xyy} + \chi^{(2)}_{yyx} + \chi^{(2)}_{yxy})\sin\phi\cos^2\phi$$

$$\chi^{(2)}_{XXY} = \chi^{(2)}_{xxy}\cos^3\phi + (\chi^{(2)}_{yyy} - \chi^{(2)}_{xyx} - \chi^{(2)}_{yxx})\sin^2\phi\cos\phi + \chi^{(2)}_{yyx}\sin^3\phi + (\chi^{(2)}_{xxx} - \chi^{(2)}_{xyy} - \chi^{(2)}_{yxy})\sin\phi\cos^2\phi$$

$$\chi^{(2)}_{XYY} = \chi^{(2)}_{xyy}\cos^3\phi + (\chi^{(2)}_{xxx} - \chi^{(2)}_{yyx} - \chi^{(2)}_{yxy})\sin^2\phi\cos\phi - \chi^{(2)}_{yxx}\sin^3\phi + (\chi^{(2)}_{xyx} + \chi^{(2)}_{xxy} - \chi^{(2)}_{yyy})\sin\phi\cos^2\phi$$

$$\chi^{(2)}_{YXY} = \chi^{(2)}_{yxy}\cos^3\phi + (\chi^{(2)}_{xxx} - \chi^{(2)}_{xyy} - \chi^{(2)}_{yyx})\sin^2\phi\cos\phi - \chi^{(2)}_{xyx}\sin^3\phi + (\chi^{(2)}_{yxx} + \chi^{(2)}_{xxy} - \chi^{(2)}_{yyy})\sin\phi\cos^2\phi$$

(4.3-4.6)

Further considering the case that collagen has cylindrical symmetry, but may have some small out of axis tilt, a rotation matrix $\mathbf{R}_x$ can be defined:

$$\begin{pmatrix} 1 & 0 & 0 \\ 0 & \cos\theta & -\sin\theta \\ 0 & \sin\theta & \cos\theta \end{pmatrix}$$

giving an overall rotation matrix $\mathbf{R}= \mathbf{R}_{x'}\mathbf{R}_{z}$:

$$\begin{pmatrix} \cos\phi & -\sin\phi & 0 \\ \cos\theta\sin\phi & \cos\theta\cos\phi & -\sin\theta \\ \sin\theta\sin\phi & \sin\theta\cos\phi & \cos\theta \end{pmatrix}$$

From this new rotation matrix and the cylindrical symmetry assumption,

$$\chi^{(2)}_{YYY} = \chi^{(2)}_{yyy}\cos^3\phi\cos^3\theta + (\chi^{(2)}_{yxx}+\chi^{(2)}_{xyx}+\chi^{(2)}_{xxy})\cos\phi\sin^2\phi\cos^3\theta + (\chi^{(2)}_{yzz}+\chi^{(2)}_{zzy}+\chi^{(2)}_{zyz})\cos\phi\cos\theta\sin^2\theta$$

$$\chi^{(2)}_{XXY} = \chi^{(2)}_{xxy}\cos^3\phi\cos^3\theta + (\chi^{(2)}_{yyy}-\chi^{(2)}_{yxx}-\chi^{(2)}_{xyx})\sin^2\phi\cos\phi\cos\theta + (\chi^{(2)}_{xyz}+\chi^{(2)}_{yxz})\cos\phi\sin\phi\sin\theta$$

(4.7-4.8)

These relations are useful in evaluating the chemical significance of the experimental results.

4.4. Results and Discussion

The combined VR-SFG and SHG microscope was used to obtain images of rat tail tendon collagen and hawk corneal collagen. Figure 4.3 shows a comparison of the images from the rat tail tendon and hawk cornea with both VR-SFG and SHG [32]. The polarizations of the incident excitation beams were aligned along the long axis of the collagen fibrils in the sample, and for VR-SFG the mid-infrared resonance was tuned to 2950 cm^{-1}. As both methods probe the second order nonlinear response, similar features are observed in the VR-SFG and SHG images. The resolution of the VR-SFG image is limited by the diffraction limit of the mid-infrared wavelength and slightly lower. However, the overall intensity of the VR-SFG signal is 2 to 5 times that of SHG and SFG contrast seems higher.

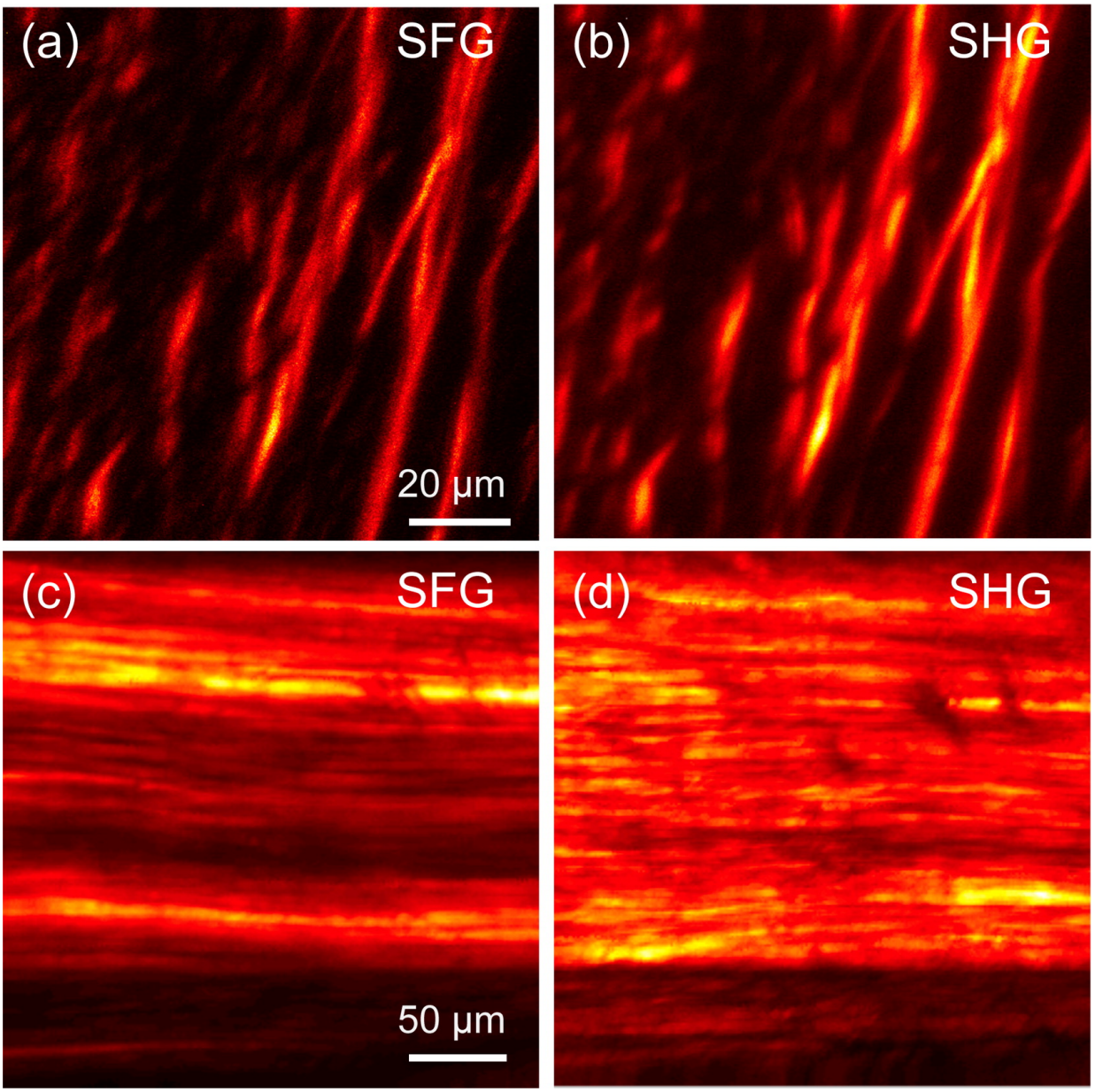

Figure 4.3: SFG and SHG images of hawk cornea (top, a and b), as well as SFG and SHG images of rat tail tendon (bottom, c and d). Wavelengths used were $\omega_1 = 2950\ cm^{-1}$ and $\omega_2 = 12\ 897\ cm^{-1}$, polarization along the long axis of collagen, figure intensities normalized.

To investigate the image contrast of the two modalities, anisotropy measurements where both excitation beams were first aligned parallel to collagen fibers, then perpendicular to the fibers were taken. As shown in Figure 4.4, the VR-SFG shows a much higher anisotropy when on resonance (up to ρ =15) , whereas the SHG anisotropy is relatively constant at $\rho = I_{//}/I_{\perp} \approx 3$. This shows that VR-SFG is preferable in terms of contrast when imaging samples with fibers of scattered orientation. The anisotropy measurements indicate that the relative contributions of different $\chi^{(2)}$ elements changes when on or off resonance. In the measurement here, the parallel configuration measures a sum of the $\chi_{yyy}^{(2)}$ and $\chi_{xyy}^{(2)}$ elements, while the perpendicular configuration measures the $\chi_{yxx}^{(2)}$ and $\chi_{xxx}^{(2)}$ elements. Applying cylindrical symmetry for collagen, the anisotropy ratio is equivalent to a ratio of $|\chi_{yyy}^{(2)}/\chi_{yxx}^{(2)}|^2$, leading to the conclusion that the ratio of these two elements is higher when on resonance.

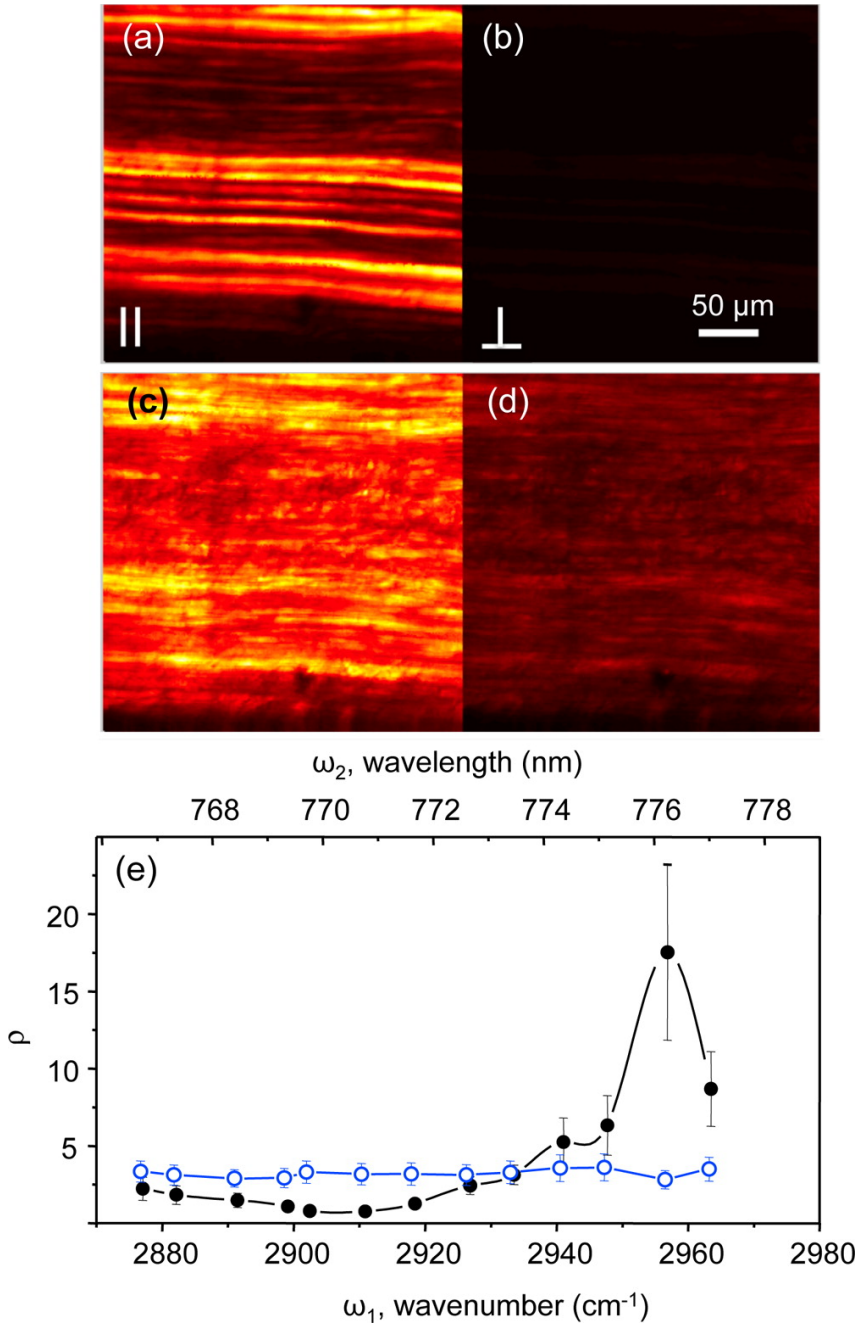

Figure 4.4: Anisotropy measurements for SFG and SHG on rat tail tendon collagen. a) SFG image of rat tail tendon collagen where both excitation beams are aligned parallel to the fiber long axis. b) SFG image where both beams are aligned perpendicular to the fiber long axis.

c) SHG image of the same area with excitation polarization aligned with the fiber. d) SHG where the excitation beam is perpendicular to the fiber axis. e) Graph comparing anisotropy of SFG (black line) and SHG (blue) over wavelength range that covers collagen resonance mode at 2950 cm^{-1}. Error bars indicate standard deviation for four measurements.

Following the anisotropy measurements, a more detailed analysis of 8 different tensor elements of rat tail tendon collagen was conducted by scanning across the CH stretch region with polarizer settings of *YYY*, *XXY*, *XYX*, *YXX*, *XXX*, *YYX*, *YXY*, and *XYY* . The resulting spectra are shown in Figure 4.5. The rat tail tendon was aligned with the *Y* axis so that ϕ =0 and the two coordinates (*X,Y,Z*) and (*x,y,z*) are equivalent. In this case the measured tensor elements are directly equal to the collagen susceptibility tensor elements.

Based on the cylindrical symmetry of collagen, the $\chi_{yyy}^{(2)}$, $\chi_{yxx}^{(2)}$, $\chi_{xxy}^{(2)}$, and $\chi_{xyx}^{(2)}$ elements are expected to have nonzero signal. Indeed signals are observed in these elements, and the signals were especially strong for $\chi_{yyy}^{(2)}$ and $\chi_{xxy}^{(2)}$ at the 2954 cm^{-1} resonance. The resonance is much weaker in the other two elements where the polarization of the mid-infrared ω_1 field is not aligned with the collagen long axis. Previous works have predicted methylene vibrational modes as a likely origin to the CH stretch signal [33]. Assuming C_{2v} symmetry for the methylene mode, it is expected that the $\chi_{yxx}^{(2)}$ and $\chi_{xyx}^{(2)}$ elements will be weaker and $\chi_{xxy}^{(2)}$ will be strong. The experimental data are in agreement with this, supporting that the 2954 cm^{-1} CH stretch is a symmetric stretching vibration.

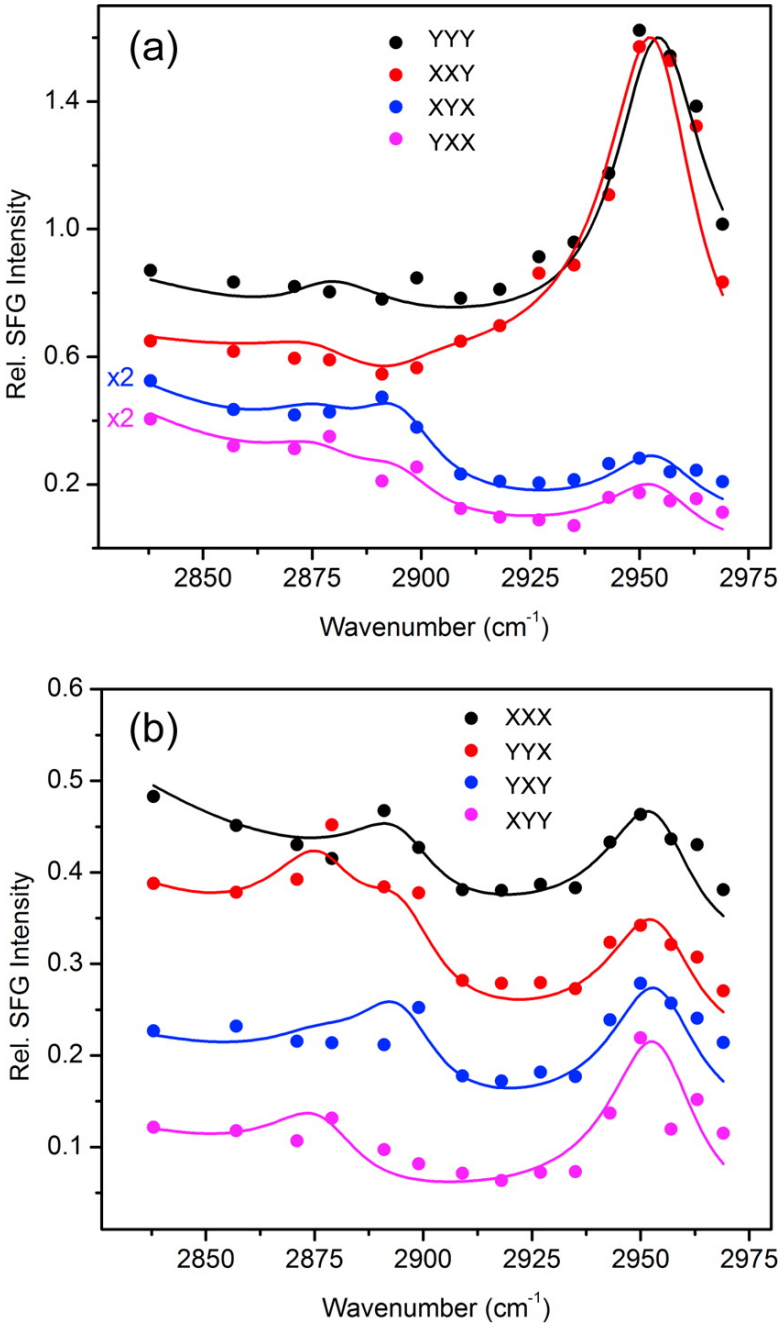

Figure 4.5: Polarization dependent spectra of rat tail tendon collagen in the CH stretch region. a) Stronger tensor elements: *YYY*, *XXY*, *XYX*, and *YXX* b)Weaker tensor elements: *XXX*, *YYX*, *YXY*, and *XYY* . Curves are vertically offset and collagen is aligned along the *Y* axis.

The spectra in Figure 4.5 can be fit with Lorentzian curves, where the frequency dependence of the nonlinear susceptibility can be written as:

$$\chi_{ijk}^{(2)} = \chi_{ijk,NR}^{(2)} e^{i\varphi} + \sum_{\upsilon} \frac{A_{\upsilon}^{ijk}}{(\omega_{\upsilon} - \omega) - i\Gamma_{\upsilon}} \tag{4.9}$$

with $\chi_{ijk,NR}$ being the nonresonant response, φ a phase shift for the nonresonant component, and the resonant response being a sum of Lorentzian curves of resonance frequency ω_v, half width half max Γ_v, and amplitude A. The total SFG signal can then be written as:

$$S_{I,J,K} \propto S_0 + \left|\chi_{IJK}^{(2)}\right|^2 \tag{4.10}$$

where S_0 is a background unrelated to second order nonlinear effects.

These equations are used to fit the data in Figure 4.5, and the best fit is obtained by fitting with three bands at 2954 cm^{-1}, 2896, and 2877 cm^{-1} with widths of 12.1, 11.8, and 12.4 cm^{-1}, respectively. The amplitudes for each band in different tensor elements are shown in Table 4.1, while the nonresonant responses are shown in Table 4.2.

Table 4.1: Lorentzian profile amplitudes for modeling polarization SFG spectra.

	2954 cm^{-1}	2896 cm^{-1}	2877 cm^{-1}
A^{yyy}	-4.82	-0.09	1.15
A^{xxy}	3.81	-0.29	0.40
A^{xyx}	0.88	0.90	0.40
A^{yxx}	0.80	0.50	0.40
A^{yxy}	1.20	0.80	0.20
A^{xyy}	1.45	0.00	0.67
A^{xxx}	1.00	0.51	0.00
A^{yyx}	0.95	0.65	0.65

Table 4.2: Modeling of nonresonant contributions to SFG spectra.

yyy	0.05
xxy	0.09
xyx	0.05
yxx	0.06
yxy	0.05
xyy	0.05
xxx	0.08
yyx	0.08

While the main band at 2954 cm^{-1} correlates well with a CH symmetric stretch of collagen, the other two weaker bands at 2896 and 2877 cm^{-1} are unlikely to be from the same mode. They are most predominant in the $\chi_{YXX}^{(2)}$ and $\chi_{XYX}^{(2)}$ spectra while also showing in the $\chi_{XXX}^{(2)}$, $\chi_{XYY}^{(2)}$, $\chi_{YYX}^{(2)}$, and $\chi_{YXY}^{(2)}$ elements, which are not present under a cylindrical symmetry assumption. The polarization measurements that follow further confirm the likelihood that these bands come from other molecule sources in the rat tail tendon other than the collagen fibers.

Polarization measurements were performed where the collagen fiber was rotated from 0 to 180 degrees and intensities of different tensor elements were recorded. Figure 4.6 shows an example of the polarization measurements at 2949 cm^{-1}, representative of the on resonance signal for CH stretching. The incident excitation beams were both oriented along the *Y* axis, and the signal analyzer polarization was also along the *Y* axis, giving the *YYY* tensor term. The small dots in the images were scattered $BaTiO_3$ particles that were used to identify the rotation angle of the collagen fibers.

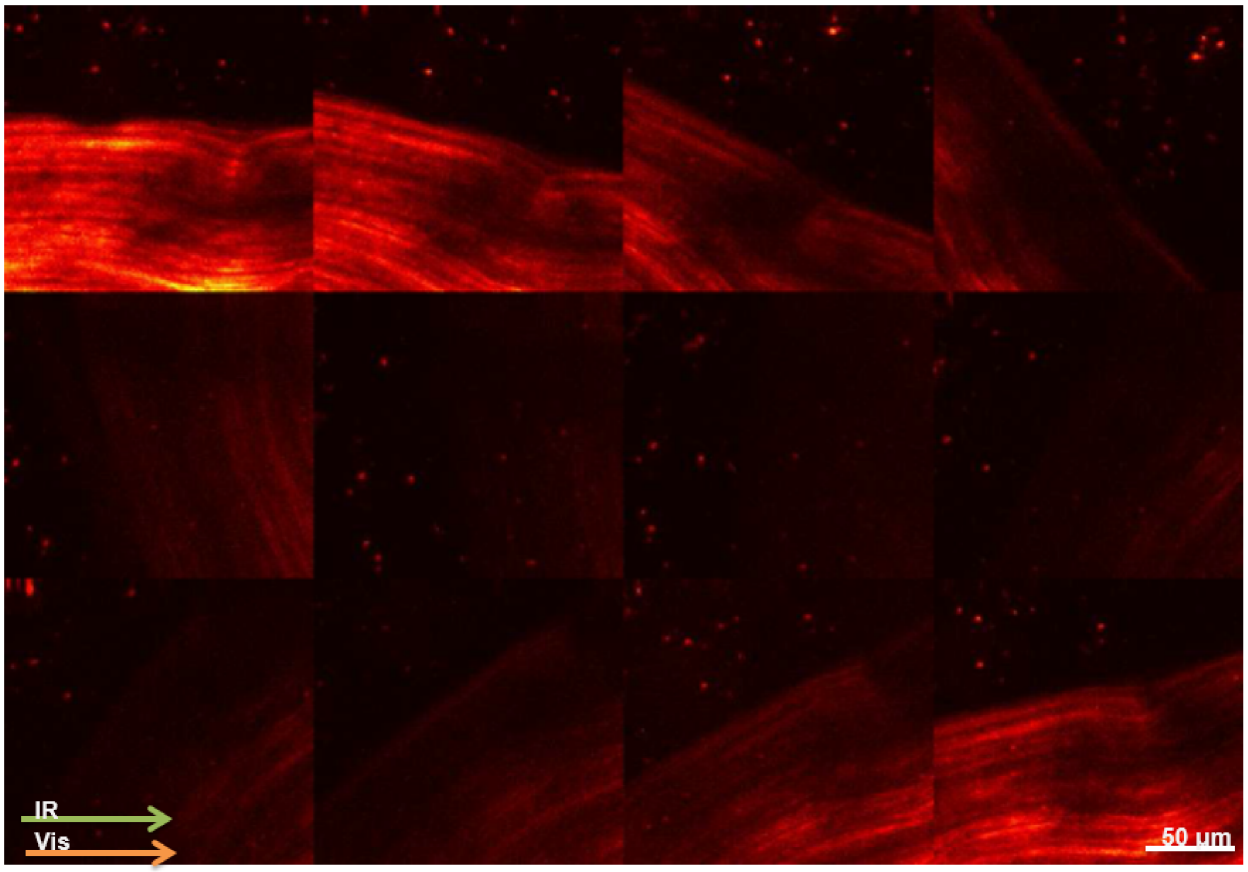

Figure 4.6: Polarization dependent measurements of rat tail tendon collagen. The incident beam and signal polarizations were all fixed along the *Y* axis, while the collagen sample was rotated.

Similar measurements were done for the *XXY, XYY*, and *YXY* tensor configurations, and the same areas in each image were summed to obtain the relative intensities of the four tensor elements. The measurement was then repeated at 2882 and 2845 cm^{-1}. The results from these measurements are shown in Figure 4.7. The first column, representative of the CH symmetric stretch resonance, corresponds well with the cylindrical symmetry collagen model. The *YYY* and *XXY* signals show $\cos^3 \phi$ dependence that indicate strong contribution of the $\chi_{yyy}^{(2)}$ and $\chi_{xxy}^{(2)}$ elements, and the four pointed patterns for *XYY* and *YXY* signals agree well with the forms in Eq

(4.5-4.6). The data in Figure 4.7 were fitted based on Eqs (4.3-4.6) to calculate the relative magnitudes of the tensor elements, and the data is shown in Table 4.3.

Table 4.3: Global fitting of relative tensor elements for polarization dependent SFG.

	2949 cm^{-1}	2882 cm^{-1}	2845 cm^{-1}
yyy	1.00 ± 0.07	0.06 ± 0.09	0.51 ± 0.04
xxy	−0.97 ± 0.08	0.15 ± 0.10	0.28 ± 0.07
xyx	0.24 ± 0.15	0.60 ± 0.05	0.28 ± 0.06
yxx	0.25 ± 0.15	−0.55 ± 0.05	0.15 ± 0.08
xxx	0.01 ± 0.19	0.29 ± 0.08	0.06 ± 0.11
yyx	0.01 ± 0.18	0.35 ± 0.07	0.02 ± 0.10
yxy	0.00 ± 0.11	−0.07 ± 0.09	−0.06 ± 0.07
xyy	0.00 ± 0.11	0.14 ± 0.08	0.01 ± 0.08

The second column of Figure 4.7 shows the polarization dependence at 2882 cm^{-1} signal, representative of the 2885 cm^{-1} spectral region. The polarization dependence here is very different from the 2949 cm^{-1} dependence; the signal is maximum when the collagen fibers are oriented on the X axis perpendicular to the polarization of the incident beam. For a cylindrical symmetric system this should be zero signal, and the tensor elements $\chi_{xxx}^{(2)}$, $\chi_{yyx}^{(2)}$, $\chi_{yxy}^{(2)}$, and $\chi_{xyy}^{(2)}$ are necessary to fit the signal. The fitting results also indicate large contributions from the elements $\chi_{xxx}^{(2)}$ and $\chi_{yyx}^{(2)}$ that do not fit the cylindrically symmetric molecule model, further confirming that the band in this region is unlikely to be from collagen.

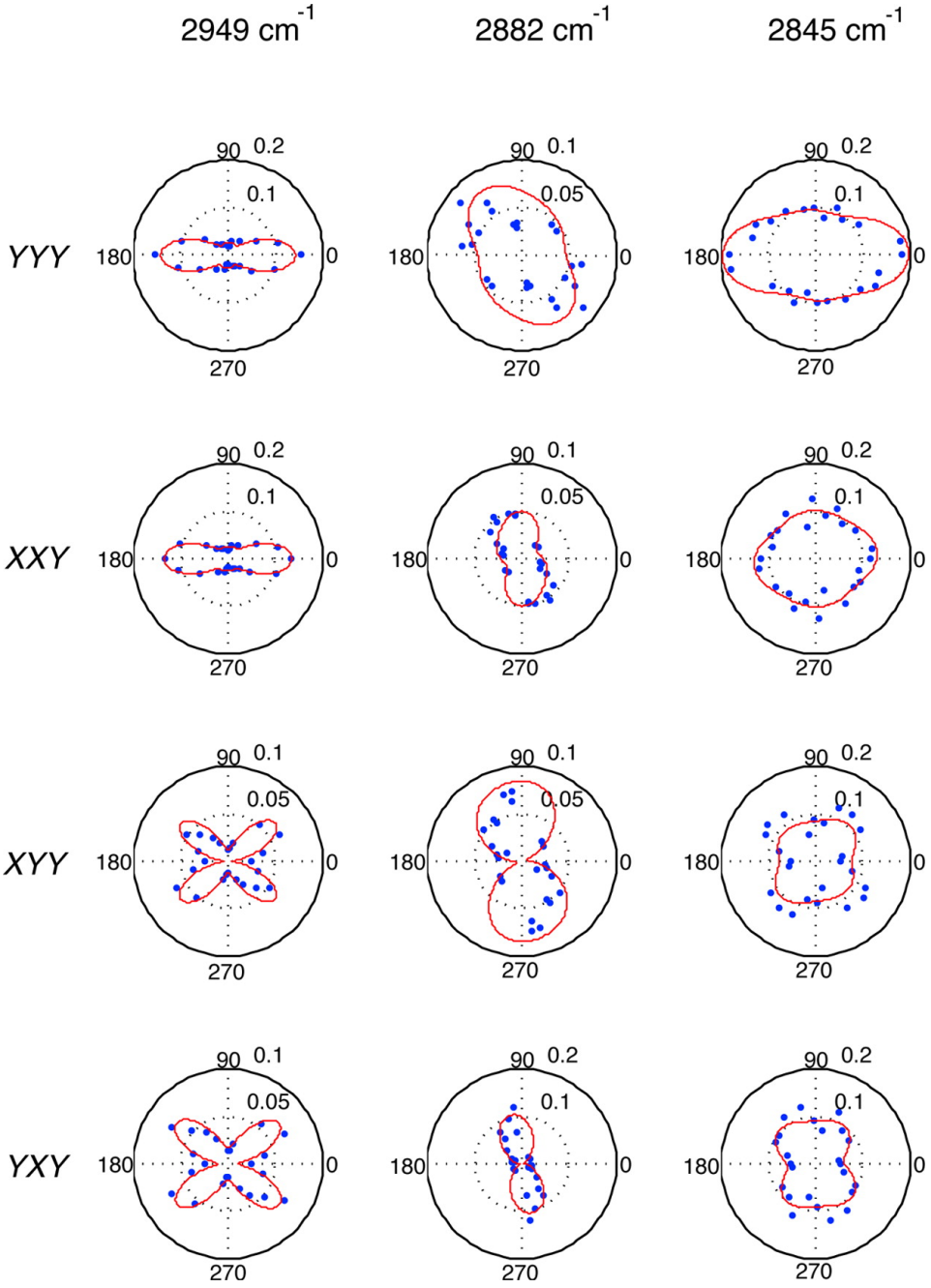

Figure 4.7: Polarization dependent sum frequency generation measurements. Collagen sample was rotated, and the *Y* axis aligns with 0 degrees in the polar plot. Dots show experimental data points and red lines show data fits.

The last column in Figure 4.7 shows the polarization dependence when the SFG is tuned off resonance. The signal displays a more isotropic shape, and a large contribution of the signal

comes from an isotropic background. This further confirms the on-resonance anisotropic signal enhancement for VR-SFG.

4.5. Conclusion

The study results demonstrate that SFG microscopy is a new technique that has advantages over currently used SHG in providing additional image contrast and chemical information. The measurements on collagen have shown high contrast and specificity, and the polarization dependent measurements have been useful in uncovering the tensor contributions in on resonance and off resonance conditions. Through analysis of the tensor contributions, we have been able to identify bands that correlate well with collagen methylene stretch vibrations as well as ones that are likely from another source in the tissue. The measurements have also clearly demonstrated the polarization dependent resonance enhancement of signal in VR-SFG. It is an imaging modality that combines the selectivity of infrared vibrational resonance, surface specificity of a second-order process, and speed and resolution of coherent nonlinear imaging and can be a powerful tool in future advancement of our understanding of microscale structures.

Chapter 5. Optical Study of Melanin

Melanins are the most common pigment found in mammalian animals and play an important role in protection against photodamage. Studies have shown that its photoprotective properties can play an influential role in skin cancer development, and eumelanins and pheomelanins may have different roles. This project aims to measure the Raman, time-resolved fluorescence, and transient absorption spectrum for eumelanin and pheomelanin to get a better picture of the optical properties of melanin and to find ideal signatures for identifying the two types of melanin. This will help in distinguishing between different types of melanin as well as in understanding the predominant optical processes that occur in melanin.

5.1. Melanin

Melanins are a broad group of pigments that are abundant in many organisms. They are produced by melanocyte cells in ~1 micron sized organelles called melanosomes. For humans, they exist in large quantities in skin, hair, and the retina. Melanosomes can be separated into two major classes: the brown-black eumelanin and the red pheomelanin. Melanin is able to effectively absorb light, dissipating over 99.9% of absorbed UV radiation[34]. It has been shown however that while eumelanin generally acts as a anti-oxidant photoprotecter, pheomelanin may become a photosensitizer after undergoing photodamage[35,36]. This may have implications for the cause of melanoma, currently the cause of 75% of deaths related to skin cancer, and as such it is vitally important to understand the optical processes in melanin[37].

There has been a dilemma to understanding the structure and optical properties of melanin. Melanin is a large heterogeneous polymer compound where the cross-linking and composition of

the melanin varies for different cells and species. It is known that the basic structural units of eumelanin are 5,6-dihydroxyindole and 5,6-dihydroxyindole-2-carboxylic acid, while the basic structural units of pheomelanin are benzothiazine and benzothiazole[38]. The basic structural units are shown in Figure 5.1 [39]. However, its heterogeneity has limited the amount of further information that traditional analytical methods have been able to glean about its structure and composition. For example, linear absorption of melanin generates a broad spectral response that is relatively featureless [40]. The chemical structure of a molecule is often used in predicting and interpreting its optical properties, while vice versa optical properties are often used to identify existing chemical structures. As both are presently unclear, there is no detailed description of the chemical structure of melanin and its optical properties. This project aims to better understand the optical properties of melanin through application of various optical spectroscopy techniques.

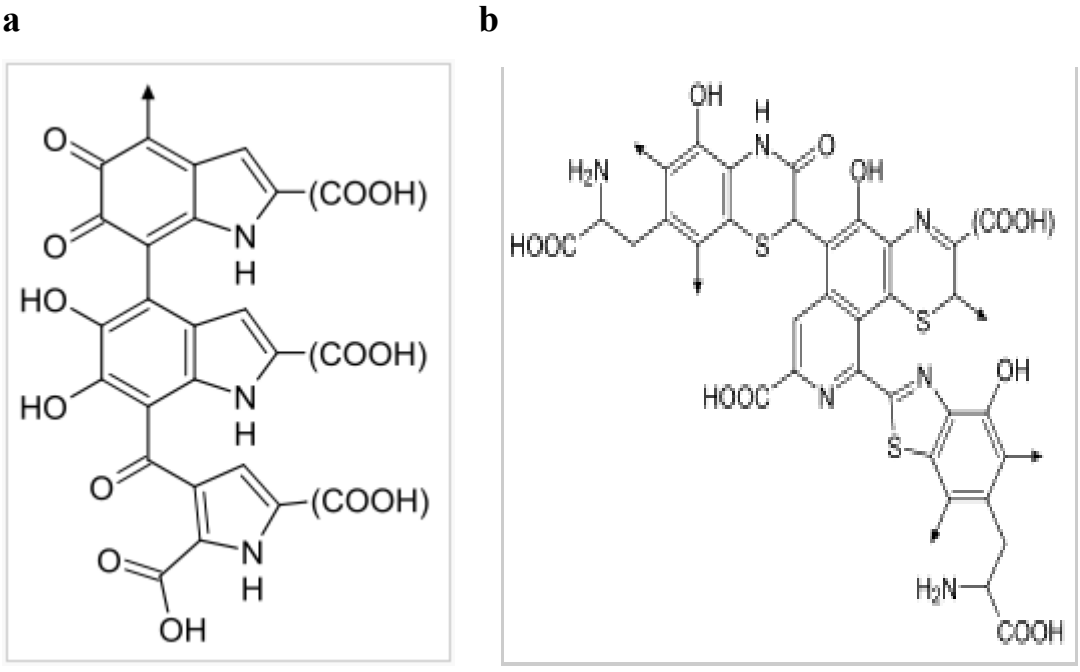

Figure 5.1: Basic structural units of melanin. a) 5,6-dihydroxyindole-2-carboxylic acid polymer in eumelanin. b) benzothiazine polymer in pheomelanin.

5.2 Melanin Sample Preparation

Several sources of melanin were used in the study. *Sepia officinalis* melanin was purchased from Sigma Aldrich. Synthetic pheomelanin as well as redhead mouse ear samples were provided by Professor Conor Evans, Harvard Medical School. Bovine and porcine retinal epithelial pigment melanosomes, both normal and photobleached, were provided by Professor Tadeusz Sarna, Jagiellonian University, Poland. Human eumelanin was extracted from black human hair based on extraction methods previously published [41]. The enzyme based extraction is briefly outlined in Figure 5.2.

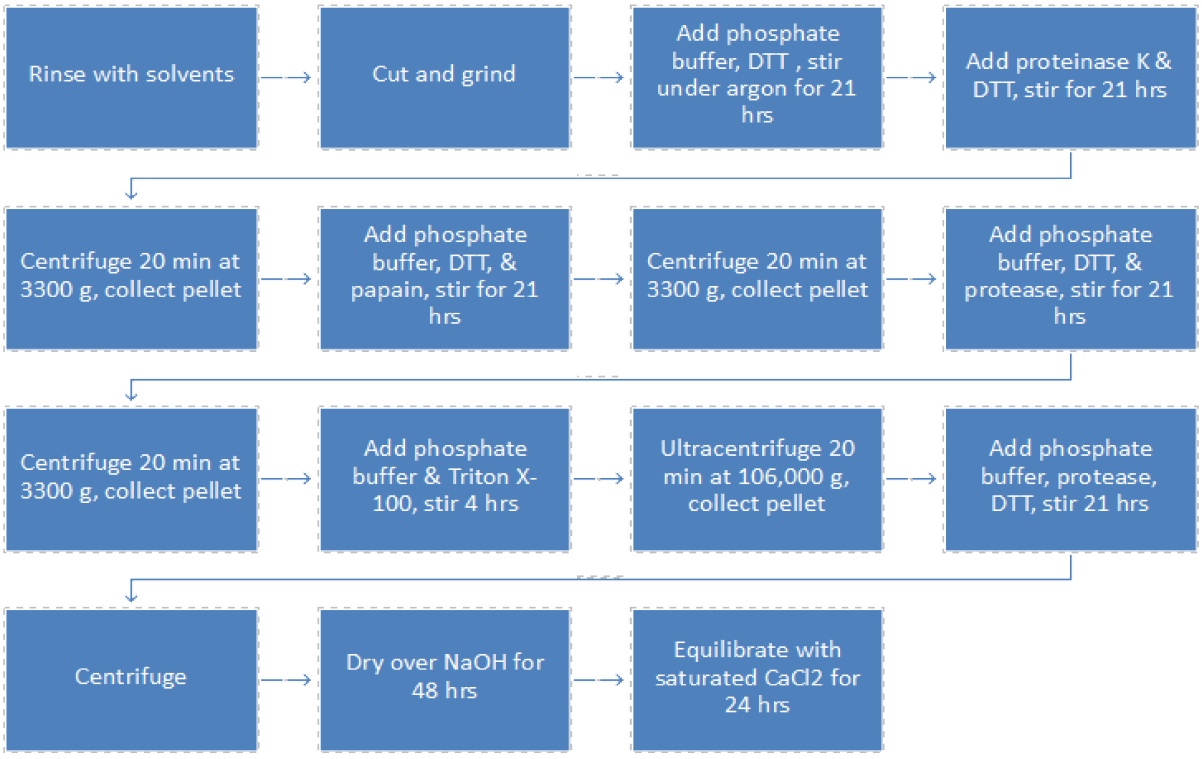

Figure 5.2: Extraction procedure of human hair eumelanin.

Melanin samples, excluding the redhead mouse ear samples mounted on slides, were suspended in pH 7.4 phosphate buffered saline. Synthetic pheomelanin was prepared as 0.84 mg/mL. Sepia eumelanin and human hair eumelanin were prepared as 3.2 mg/mL, sonicated for 2 hours, then filtered with a 1000 μm filter (Millipore).

5.3 Raman Microspectroscopy

Raman spectra of the melanin samples were compared to identify if eumelanin, pheomelanin, and photobleached melanin would have different signatures. Raman microspectroscopy was measured with a Renishaw InVia Raman microscope with a 2.2 mW 532 nm laser and 50x, 75 NA objective. Melanin samples were suspended in phosphate buffered saline and sandwiched between two glass slides. Measurements were scanned over an area of several melanosomes then averaged to reduce sample photodamage. Spectra are the averages of 20-50 measured raw spectra.

The measured spectra consistently showed broad features in the 1300 to 1600 cm^{-1} range, while there were no features visible elsewhere in the spectrum between 100 cm^{-1} to 3000 cm^{-1}. The features in the 1300 to 1600 cm^{-1} range can likely be attributed to heterogeneous C=C stretching that leads to a semiconductor-like band structure [42]. The spectrum for pig retinal epithelial melanosomes is shown in Figure 5.3 and Sepia melanin in Figure 5.4. In comparison with the synthetic pheomelanin and redhead mouser ear pheomelanin spectra in Figures 5.5 and 5.6, the eumelanins' second peak occurs at a slightly longer wavenumber. Although there are small

differences, the overall spectral features are very similar, and the broad spectral features do not provide very much structural insight.

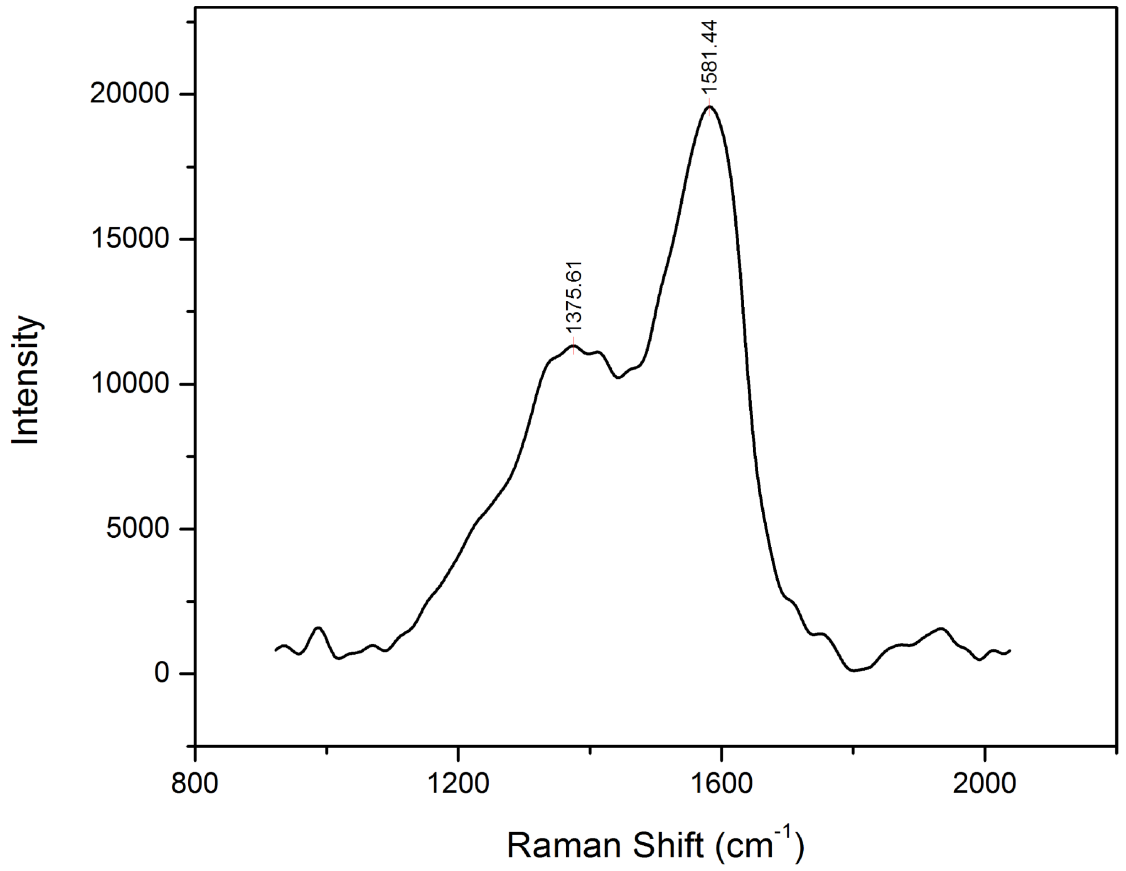

Figure 5.3: Pig RPE eumelanin Raman spectrum.

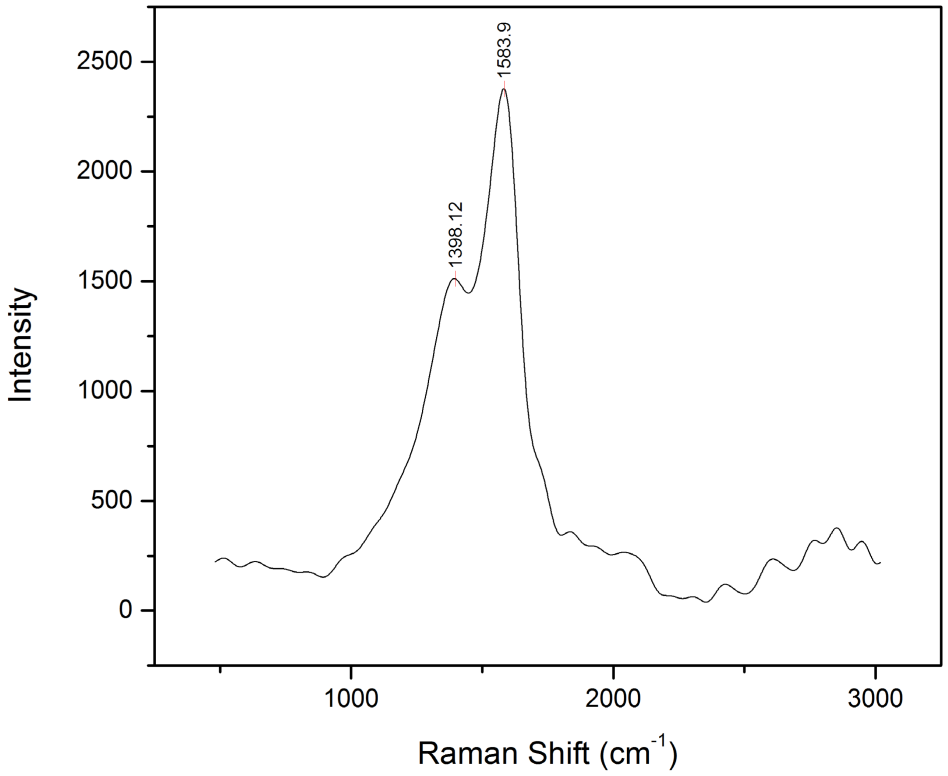

Figure 5.4: Sepia officinalis melanin Raman spectrum.

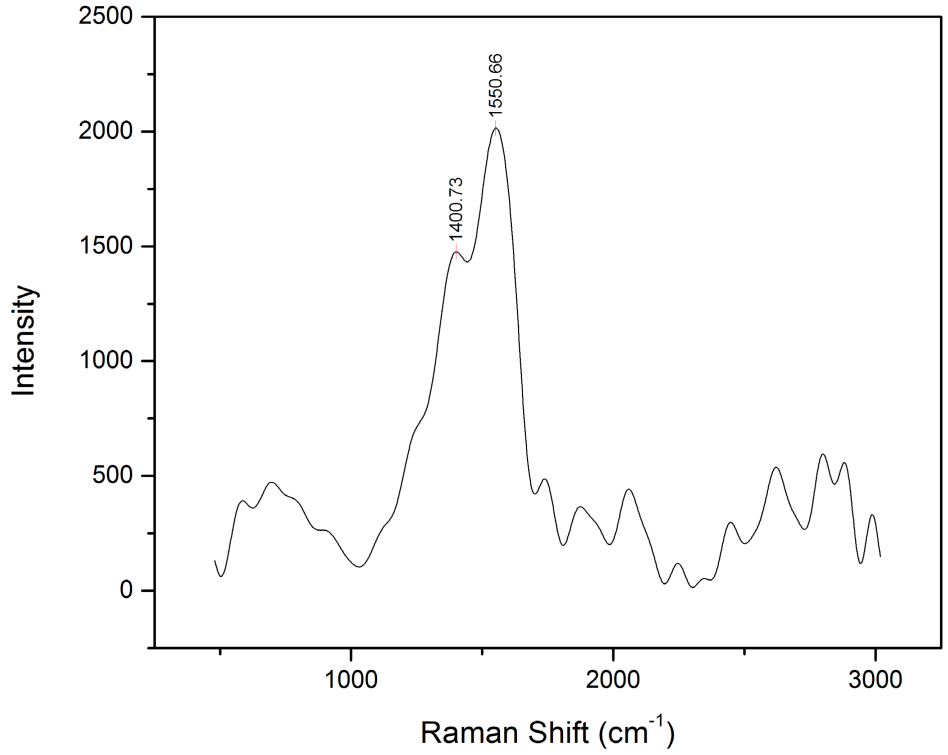

Figure 5.5: Synthetic pheomelanin Raman spectrum.

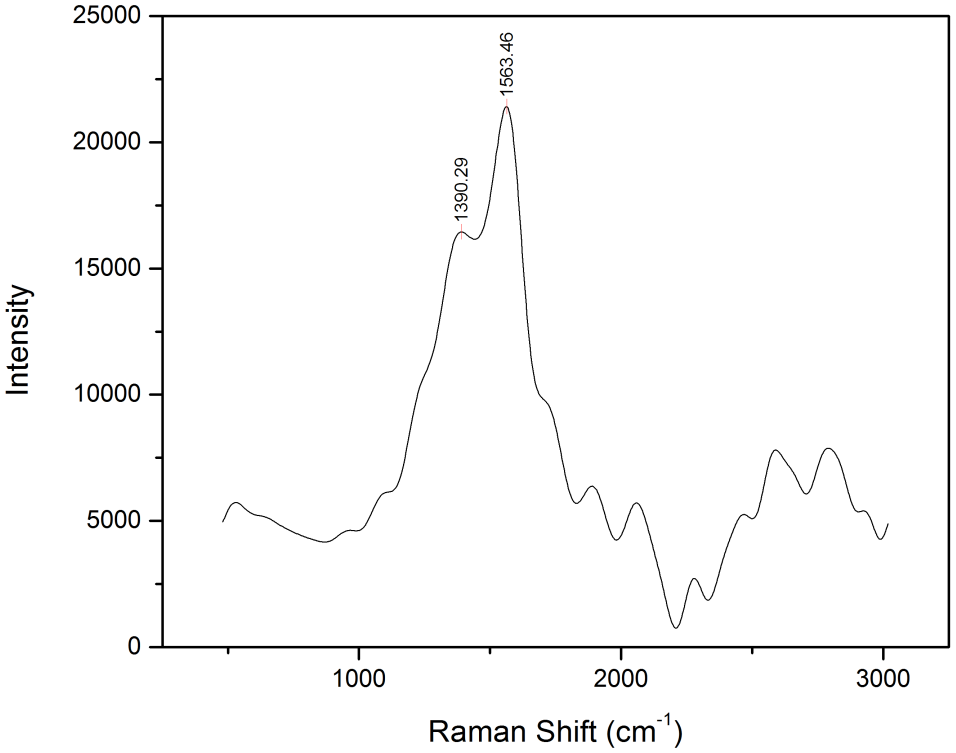

Figure 5.6: Redhead mouse ear pheomelanin Raman spectrum.

5.4 Linear Absorption, Infrared, and SRS

The optical properties of the various melanins were also compared using other optical spectroscopy techniques to see if there were any identifying features to distinguish melanin and clarify its optical properties.

Linear absorption was carried out with a Shimadzu UV-1700 absorption spectrometer. The samples were suspended in phosphate buffered saline and transferred to a cuvette. Limited by the sample amount, only Sepia melanin and the human hair extracted eumelanin linear absorption spectra were measured. As is typical of melanins, the linear absorption spectra were broad and featureless (Figure 5.7).

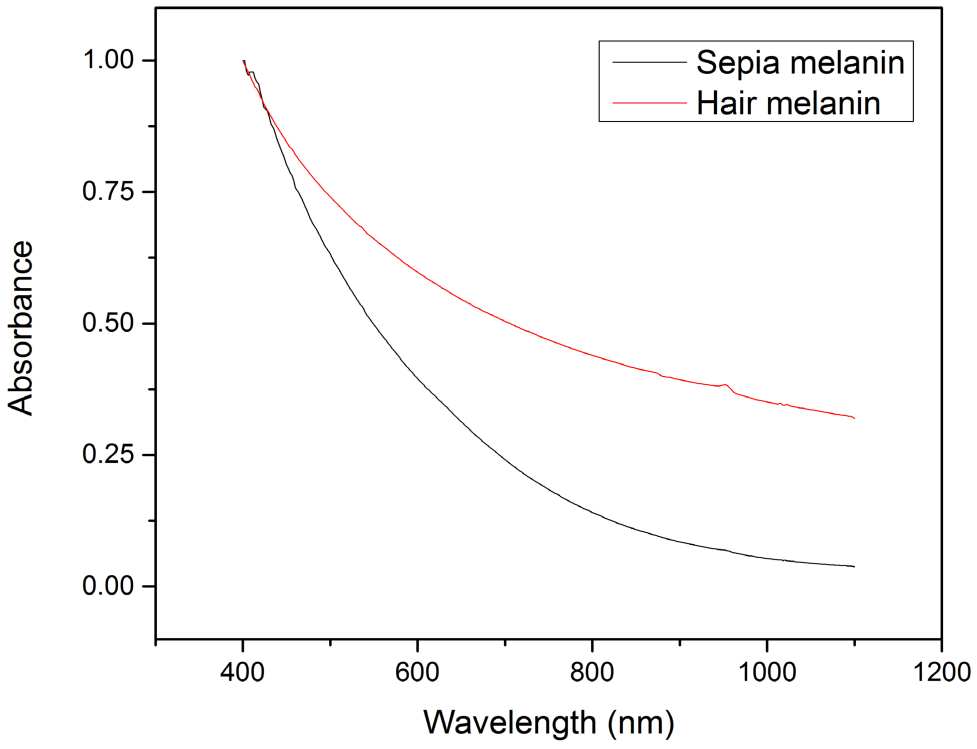

Figure 5.7: Linear absorption of Sepia melanin and human hair extracted melanin. Sepia melanin (black line) and human hair eumelanin (red line) spectra were normalized for comparison.

Infrared spectra were collected with a Jasco FT/IR-4700 spectrometer equipped with an ATR-Pro One. The ATR is only applicable to powder samples, so spectra could only be obtained for Sepia melanin and the human hair extracted melanin. The Sepia spectrum (Figure 5.8) is in close agreement with previous studies that assigned the peaks to OH/NH stretching (3300 -3400 cm^{-1}), bending vibrations of aromatic C=C(1500 -1600 cm^{-1}), and aliphatic CH groups (1300-1400 cm^{-1}) [43,44]. The human hair extracted spectrum (Figure 5.9) shows different spectral features indicative of the presence of other proteins in the extracted sample.

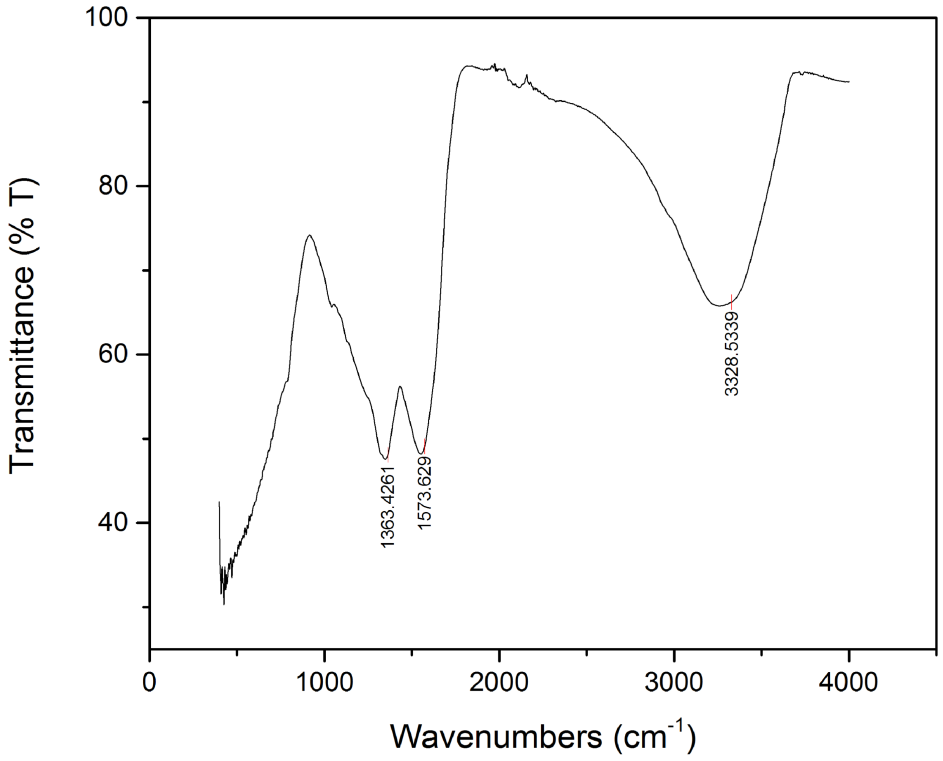

Figure 5.8: Infrared spectrum of Sepia melanin. Three main peaks at 1363, 1574, and 3329 cm-1 are labeled.

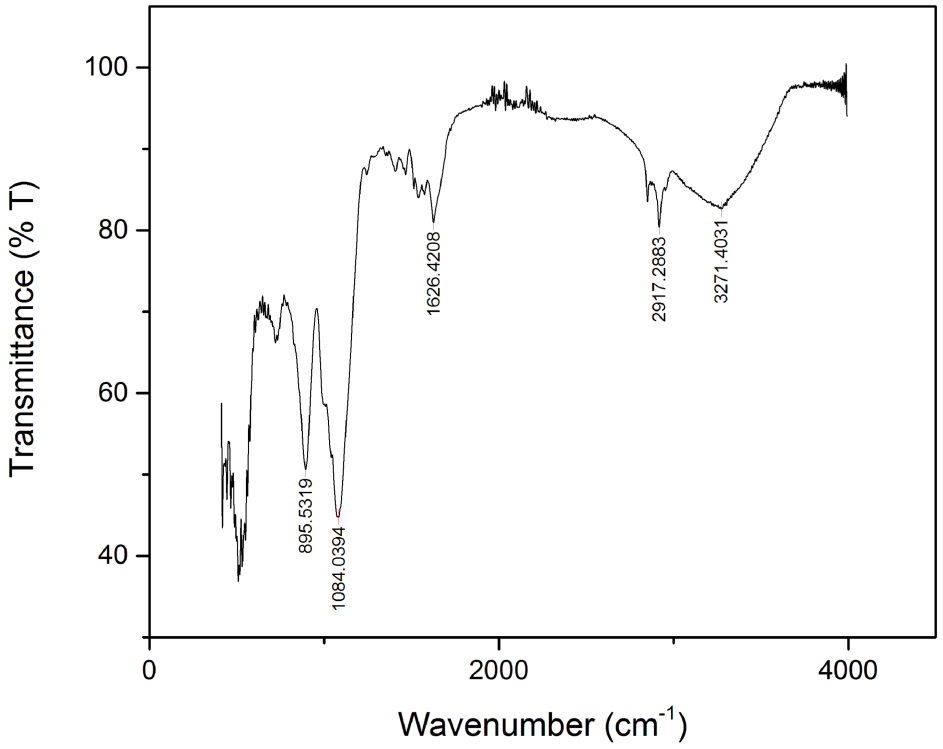

Figure 5.9: Infrared spectrum of human hair extracted melanin.

Stimulated Raman scattering hyperspectral imaging was collected with the system described previously in Chapter 3 [25]. The Stokes beam was 1064 nm, pump beam was scanned, and a 20x objective was used. Both beam intensities were 80 mW. The redhead mouse ear slides were used for this measurement, as well as synthetic pheomelanin embedded in an agarose gel. The hyperspectral scan covered a range from 1542 cm^{-1} to 2841 cm^{-1}, including the wavenumbers where Raman signal was observed in the Raman microspectroscopy measurements as well as the range for CH stretch. Figure 5.10 shows a transmission image of the redhead mouse ear area of scan.

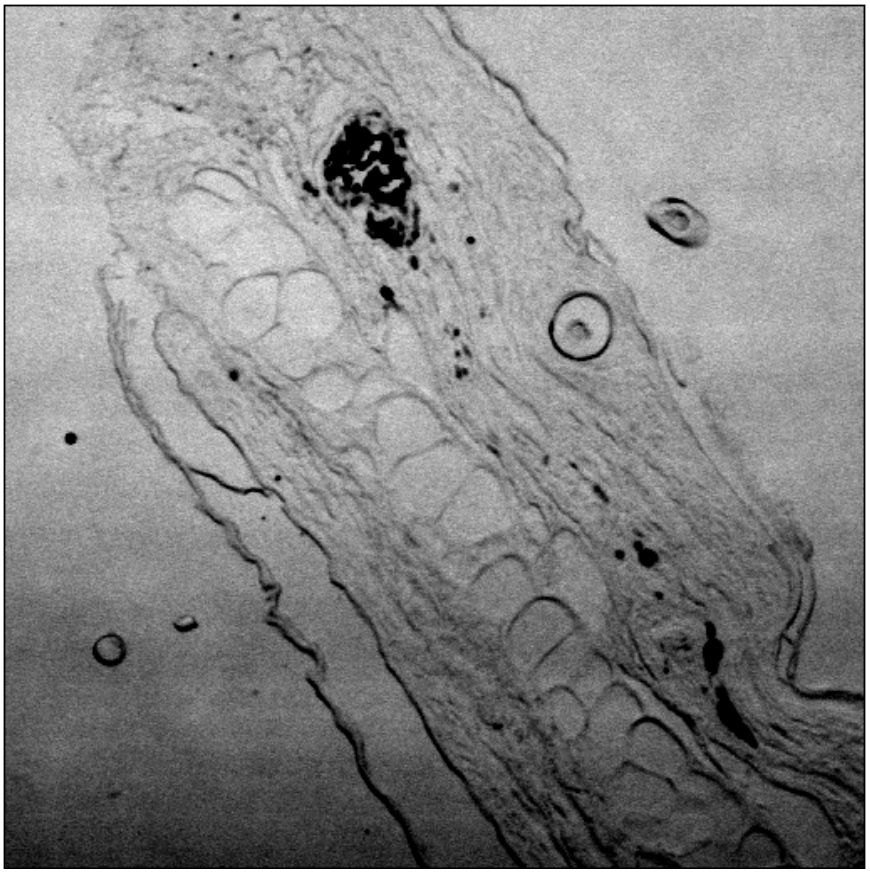

Figure 5.10: Transmission of redhead mouse ear slide. Melanin appears as black areas in transmission images.

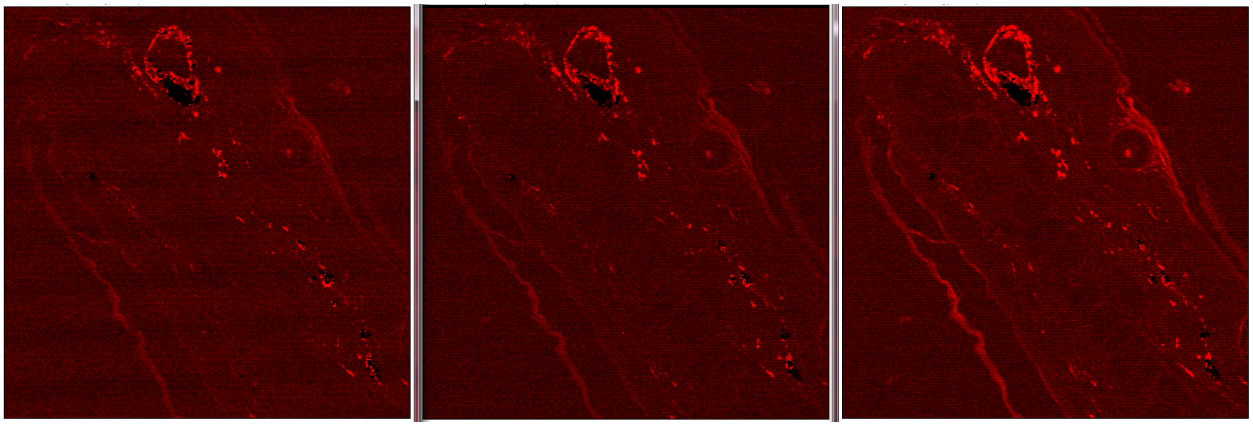

Figure 5.11: Comparison of SRS hyperspectral images of redhead mouse ear. Wavenumbers from left to right: 1712 , 2109, 2841 cm^{-1}.

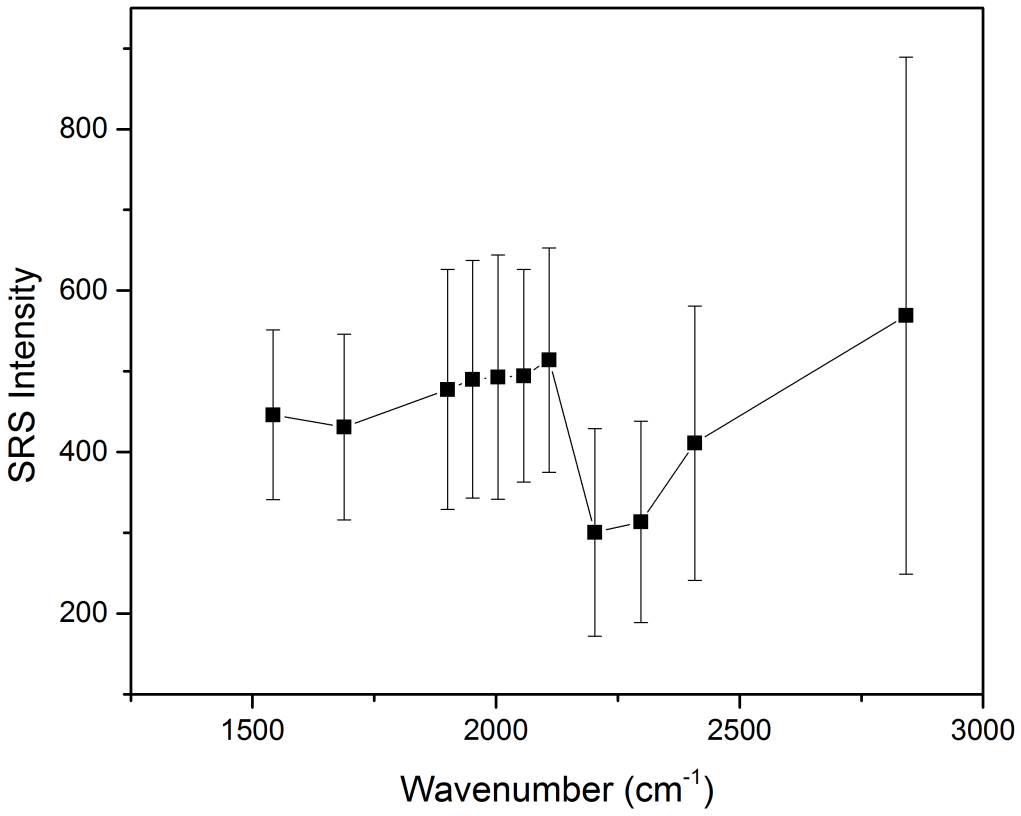

Figure 5.12 : Coarse SRS spectra of redhead mouse ear pheomelanin. Signals are averaged over an area of melanin and error bars indicate standard deviation of signal within the area.

A few examples of SRS hyperspectral scan images of the redhead mouse ear slides are shown in Figure 5.11. As can be seen, the SRS intensities did not vary much with the change of pump beam wavelength. The spectral shape is plotted in Figure 5.12, and indeed there are no visible peaks in this coarse spectrum at locations where we expect them. The 1542 cm^{-1} scan should be on resonance with the measured Raman peak, however, the SRS signal is not particularly enhanced. The 2841 cm^{-1} scan shows higher intensities overall due to larger background contributions from other tissue components with CH stretch frequencies. As such the SRS

spectra of melanin does not have any identifiable features. The SRS spectrum for synthetic pheomelanin is shown in Figure 5.13 and also does not have any identifiable features either.

The linear absorption spectra and infrared spectra of melanin both show broad features that are consistent with previous studies and the heterogeneous structural composition of melanin. The SRS spectra do not show any signatures for identifying melanin. The lack of features in the SRS spectrum is attributed to the fact that the measured signal is dominated by electronic pump-probe contributions. As will be shown in the next sections, the chosen excitation conditions give rise to a strong pump-probe contribution through the process of excited state absorption.

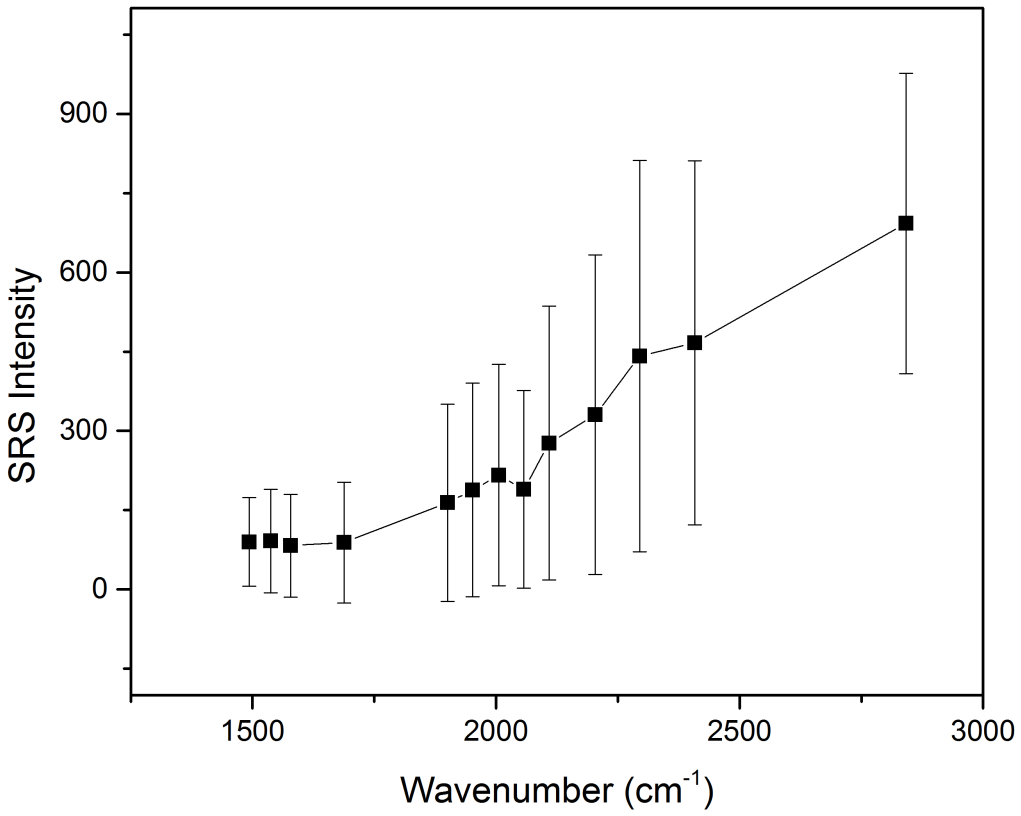

Figure 5.13: SRS spectrum of synthetic pheomelanin. Signals are averaged over an area of melanin and error bars indicate standard deviation of signal within the area.

5.5. Transient Absorption Spectroscopy

Following the measurements of melanin with the previous techniques without finding any significant distinguishing features, the melanin samples were studied with transient absorption spectroscopy. This pump-probe technique will allow for probing nonlinear effects that may not be observable with other linear spectroscopy techniques. In particular, these measurements will reveal the electronic contributions to dual-pulse, pump-probe type measurements, of which SRS is an example. The transient absorption technique is ideal for studying melanin as it can clearly highlight the spectral and time dependence of electronic excitations in eumelanin and pheomelanin. The transient absorption spectroscopy setup used consisted of a 80 MHz, 800 nm Mai Tai Ti:sapphire oscillator femtosecond laser amplified by a Spitfire-ACE-120F amplifier from Spectra-Physics (Newport Corp). The Spitfire is pumped by an Empower Q-switched Nd:YLF solid state and generates 1 kHz, 120 fs laser pulses. The beam from the Spitfire is then fed into two TOPAS Prime optical parametric amplifiers for generating a wide range of wavelengths. A Newport TAS system is used for the measurements, where the pump is modulated with a chopper and a crystal is used to generate broadband white light probe. Melanin samples were flowed through a quartz cuvette connected to a pump system to reduce sample damage. The power dependence of the TAS signal for Sepia melanin was measured as a function of the 700 nm pump intensity and shown in Figure 5.14. The linear dependence indicates that the melanin chromophores are not driven to saturation in the experiments.

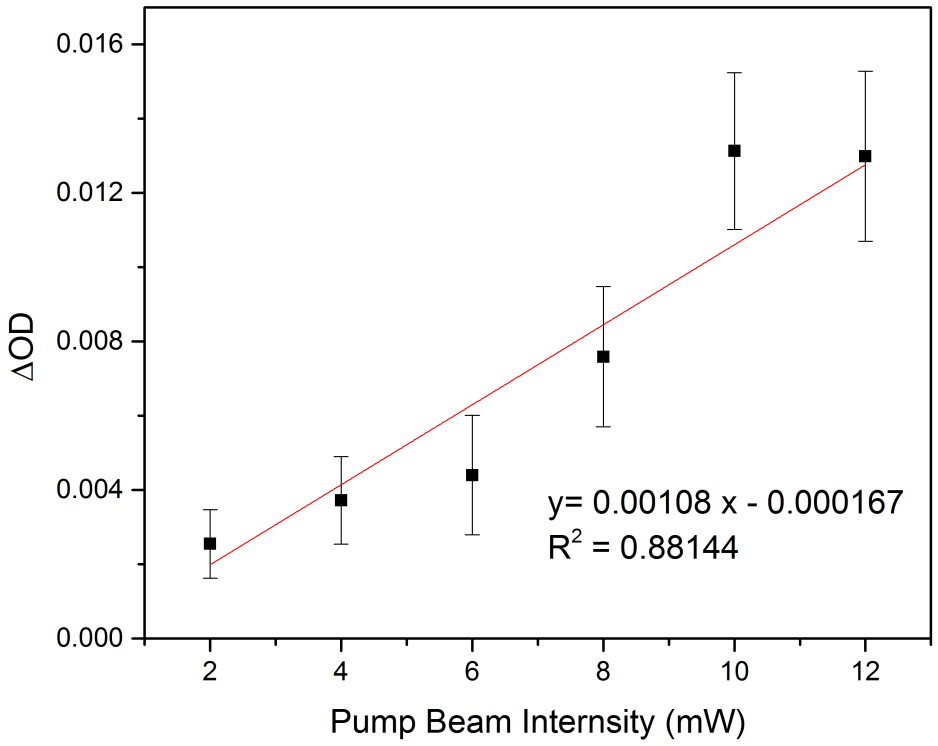

Figure 5.14: Power dependence of Sepia TAS signal as a function of pump beam intensity. Signal intensity for the near-infrared excited state absorption is linear up to 12 mW.

The transient absorption for Sepia melanin was initially pumped at 700 nm and probed with a CaF_2 crystal generated white light probe. The measurement showed an excited state absorption at 810~815 nm probe wavelength. This is in agreement with previously published studies, where an excited state absorption is reported for eumelanin at a 700 nm, 810 nm pump probe pair [45,46]. It was also observed that there is an excited state absorption at 850 nm probe wavelength. The wavelengths of the excited state absorption do not shift with time.

The decay profiles of the two excited state absorptions at 815 nm and 850 nm are compared in Figure 5.15. The decay for the 850 nm probe is faster than that of the 815 nm probe decay. They can be fit with biexponential decays with lifetimes of 1.018 ps and 54.242 ps for 815 nm and

1.183 ps and 41.170 ps for 850 nm. The decay lifetimes for the 700 nm pump, 815 nm probe are on similar time scales as previously published studies [45], while the 850 nm excited state absorption has not been explored before.

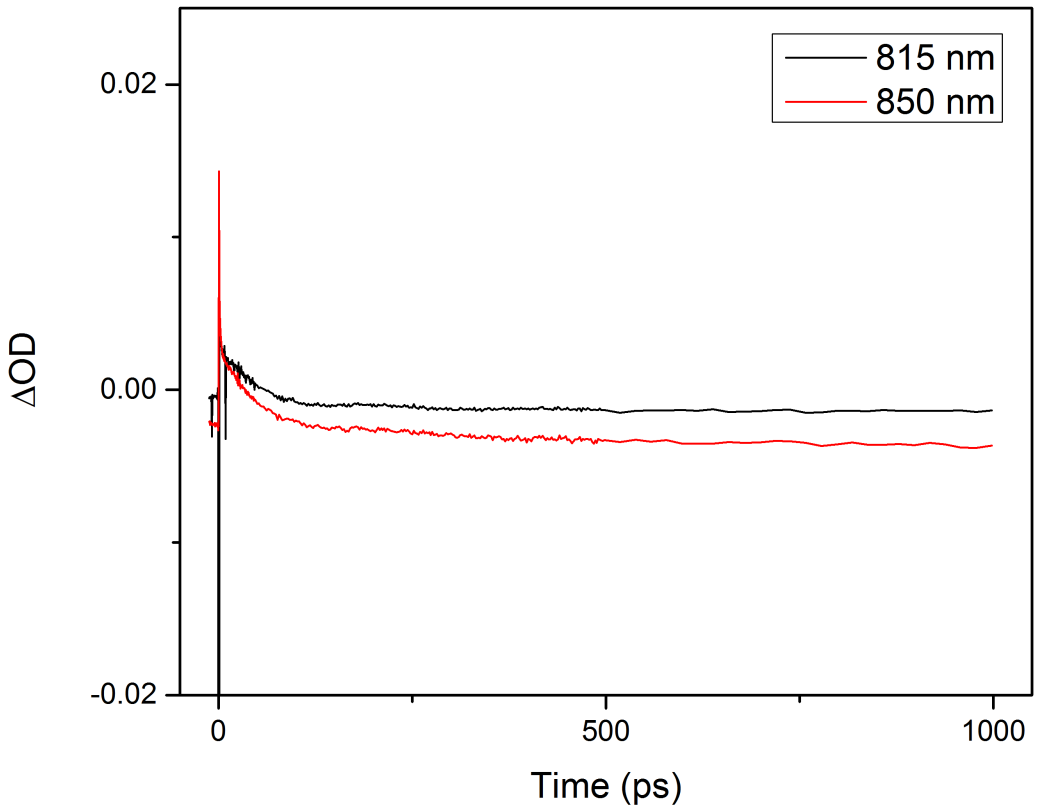

Figure 5.15: Decay profiles of Sepia melanin excited state absorption pumped by 700 nm. The excited state absorption transition at 815 nm probe is in black, the 850 nm probe is in red. The profiles are fit with biexponential decays with lifetimes: 1.018 ps and 54.242 ps for 815 nm and 1.183 ps and 41.170 ps for 850 nm.

Sepia melanin TAS measurements were also done with a 700 nm pump and YAG generated near-infrared probe setting. The data are shown in Figure 5.16. This data confirms the excited

state absorption at 850 nm probe that was shown in the previous figure while also showing excited state absorption around 900 nm.

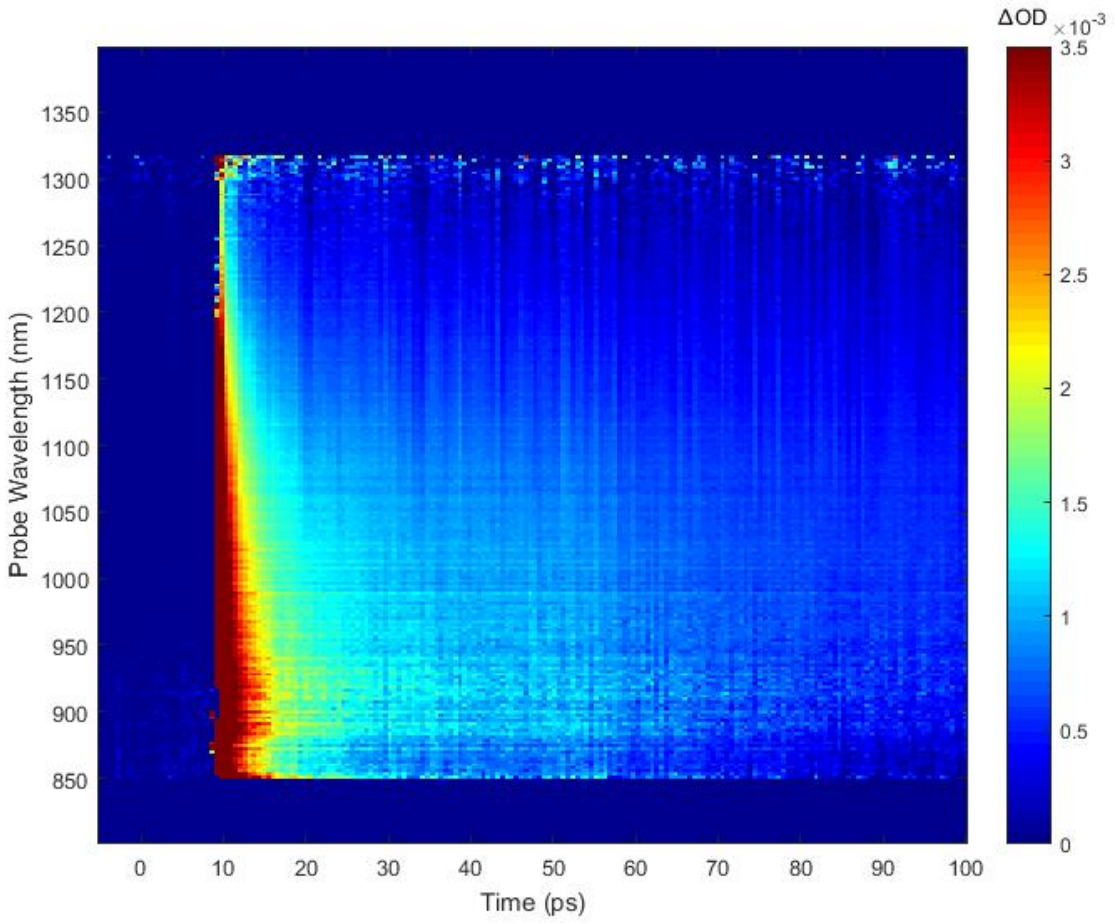

Figure 5.16: Sepia melanin TAS with 700 nm pump and YAG generated probe.

The spectral dependence for the YAG generated probe configuration is plotted in Figure 5.17. The spectra show excited state absorption with strongest signals approximately centered at 900 nm and 920 nm. The wavelengths of the excited state absorption do not shift much with time evolution, but the relative strength of the 921 nm peak increases relative to the 897 nm one for longer times, indicating a longer lifetime for that state. The decay profiles for the 850 nm, 897 nm, and 921 nm excited state absorption modes are shown in Figure 5.18. The biexponential fit

for the 850 nm mode is similar to the previous, 0.694 ps and 54.923 ps. The biexponential fit for 897 nm is 0.263 ps and 59.877 ps, while that for 921 nm is 0.268 ps and 64.285 ps. The decay lifetimes have similar magnitudes,with 921 nm slightly longer than 897 nm and 850 nm.

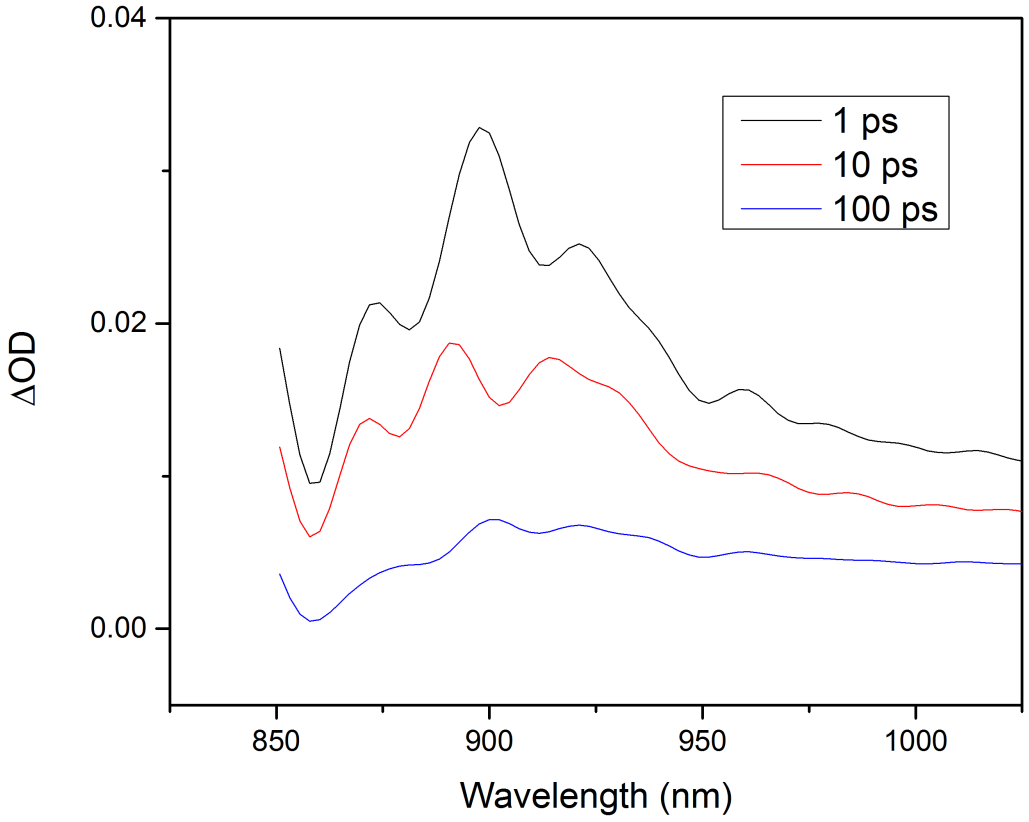

Figure 5.17: Sepia melanin TAS with 700 nm pump and YAG generated probe. The spectra show excited state absorption in the 900 nm range with strongest signal centered at 897 nm and 921 nm. The wavelengths of the excited state absorption do not shift much with time evolution, but the relative strength of the 921 nm peak increases relative to the 897 nm one for longer times.

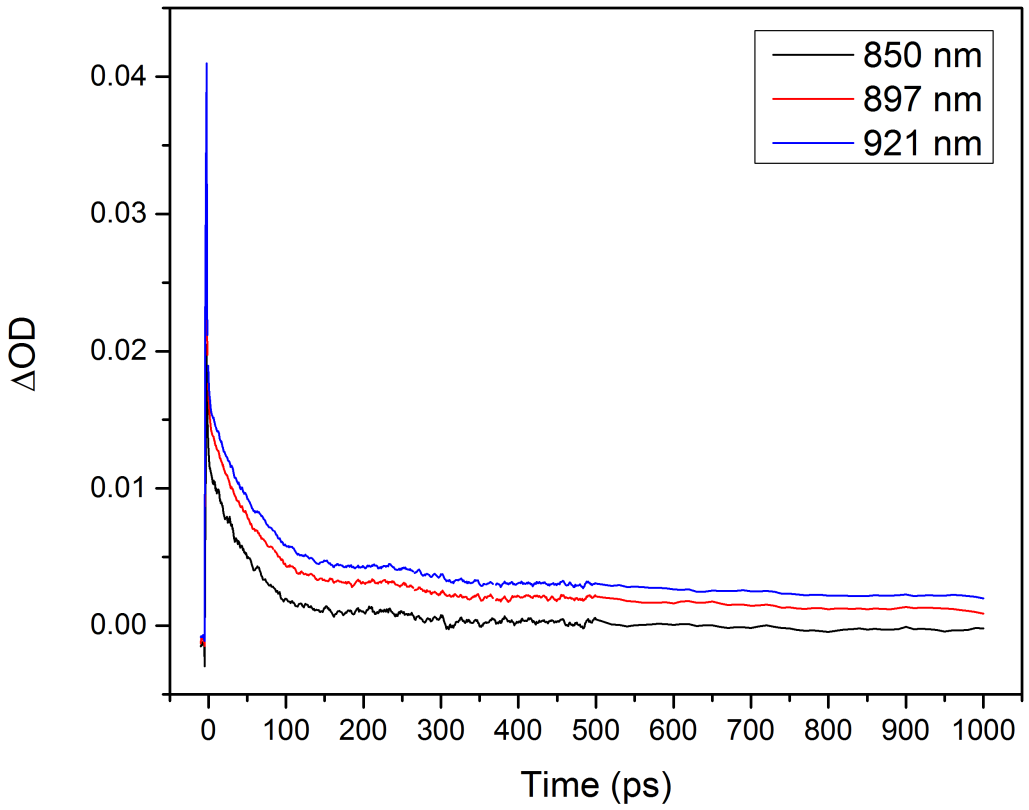

Figure 5.18: Decay profiles of Sepia melanin excited state absorption with 700 nm pump. The excited state absorption for 850 nm probe is plotted in black, 897 nm probe in red, and 921 nm probe in blue.

To follow up with the observation of the excited state absorption in the near-infrared probe range, the pump wavelength was varied to see how the transient absorption would change. Different pump wavelengths of 600 nm, 800 nm, and 850 nm were used for pump probe measurements of Sepia melanin. The excited state absorption is similar for these wavelengths, as shown in Figure 5.19. The signal was very weak for 850 nm and not shown. The decay profiles

for the peaks at 850 nm probe, 897 nm probe, and 921 nm probe are compared for the different pump wavelengths in Figure 5.20.

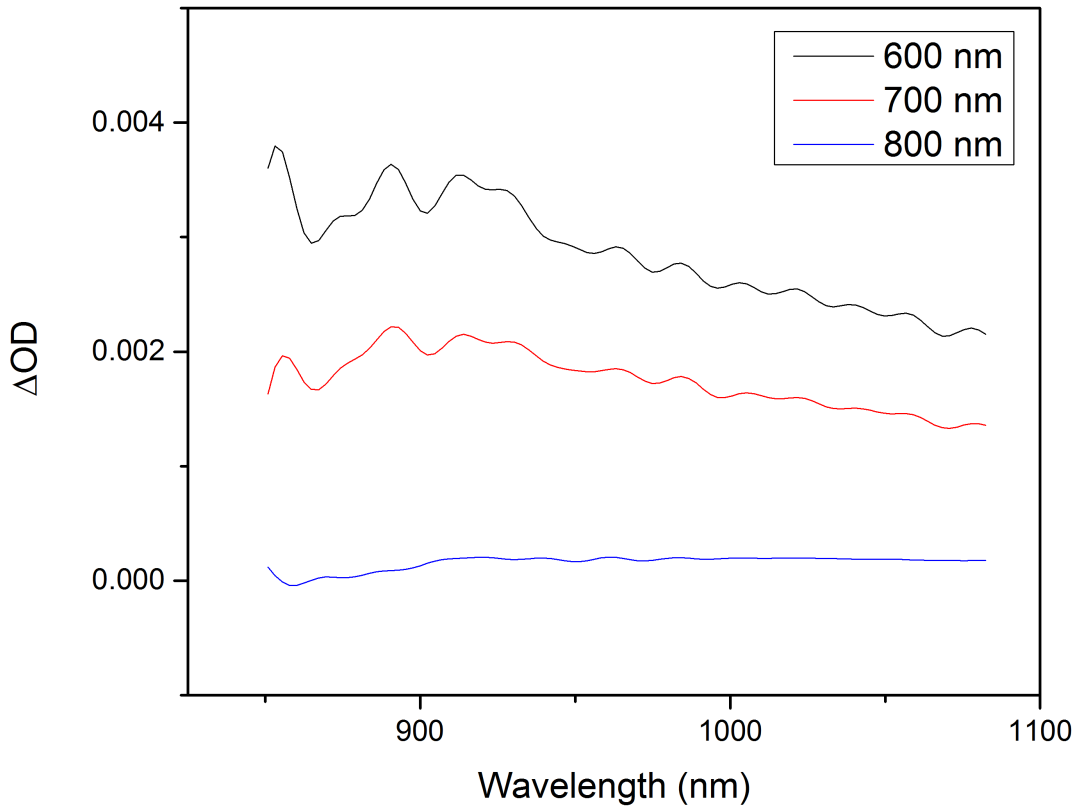

Figure 5.19: Spectral dependence of Sepia melanin TAS for various pump wavelengths. 600 nm pump wavelength (black), 700 nm pump (red), and 800 nm pump (blue) all show similar excited state absorption peaks at delay time of 1 ps.

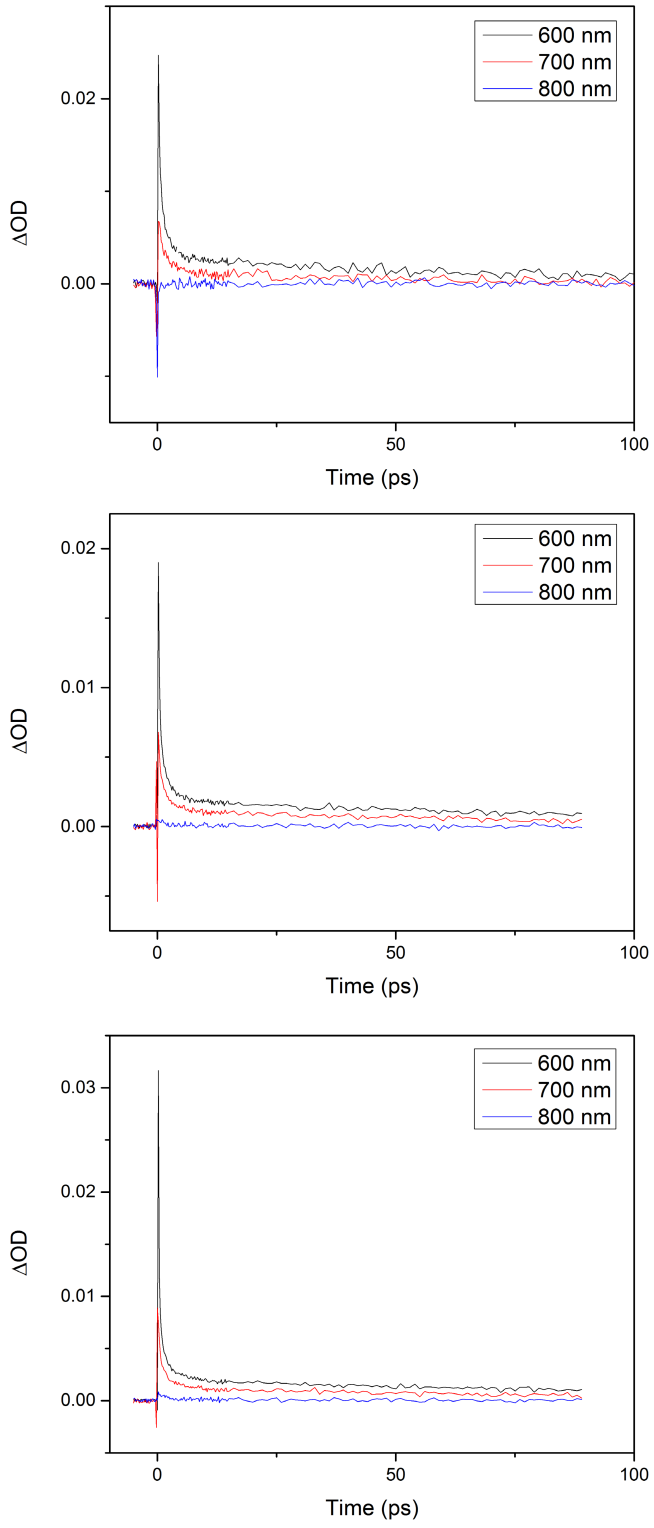

Figure 5.20: Decay profiles for Sepia melanin excited state absorption at various pump wavelengths. 850 nm probe (top), 897 nm probe (middle), 921 nm probe (bottom). 600 nm pump (black), 700 nm pump (red), 800 nm pump (blue).

The excited state transitions in the ranges of 850 nm. 900 nm, and 920 nm probe have not been reported elsewhere previously. These transitions occur for both 600 and 700 nm of pump, whereas it declines for 800 and 850 nm of pump, which is predicted to be close to the crossover wavelength where the transition no longer is probed by the wavelength combination. As the range of pump wavelengths all generate an exited state transition at the same probe wavelength, it can be concluded that there exists a fast internal conversion of the initial pump driven state to a common state from where the probe beam interacts with the molecule.

Similar TAS measurements were made for synthetic pheomelanin at 700 nm and 850 nm pump. The signal was weaker and could not be observed at 850 nm, while that at 700 nm is shown in Figure 5.21. The features are similar to that of Sepia melanin except for one excited state absorption peak shifting from 897 nm to 888 nm.

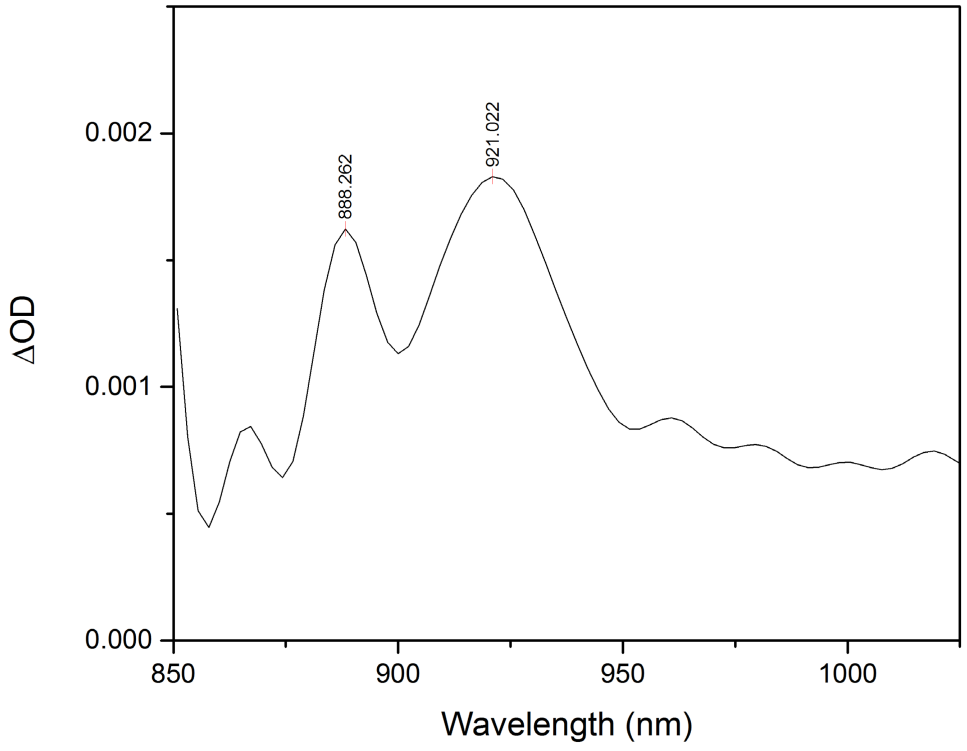

Figure 5.21: Spectral dependence of synthetic pheomelanin TAS signal at 700 nm pump and 1 ps delay time.

5.6 Time-resolved fluorescence spectroscopy

Time resolved fluorescence spectroscopy was performed on the Sepia melanin sample using the same Mai Tai femtosecond laser as the transient absorption spectroscopy system. The TRFL system from Newport is equipped with time-correlated single photon counting for measurement up to 13 ns with 100 ps resolution. The excitation at 780 nm induces a two photon fluorescence in Sepia melanin in the 500 to 600 nm range. The spectral dependence of the time-resolved fluorescence is shown in Figure 5.22. The two-photon excited emission spectrum is broad and featureless.

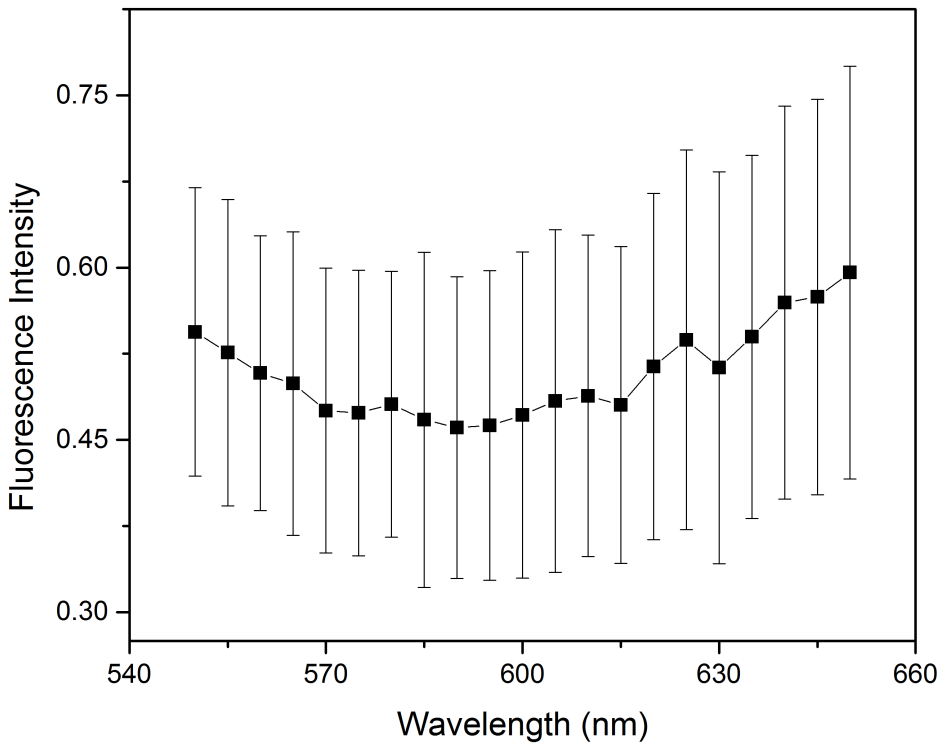

Figure 5.22: Spectral dependence of Sepia melanin time-resolved two photon fluorescence.

The time profiles for the two photon fluorescence at 550 nm and 630 nm are shown in Figure 5.23. The exponential decay can be fit with 0.317 ps and 0.44 ps, respectively. These lifetimes have the same magnitude as the shorter lifetimes fit for the transient absorption spectra. This confirms that the emitting excited states in melanin have relatively short lifetimes.

5.7. Conclusions

The optical properties of melanin were probed with various techniques, both linear and nonlinear. Generally the spectral features of melanin were quite broad, which can be expected as it is a highly heterogeneous molecule. Lifetimes of melanin included very short lifetimes less than 1 ps as well as lifetimes on the 40~60 ps range. The observation of excited state absorption in the 850 to 920 nm range has not been reported before, and provides some insight into optical pathways in melanin.

a

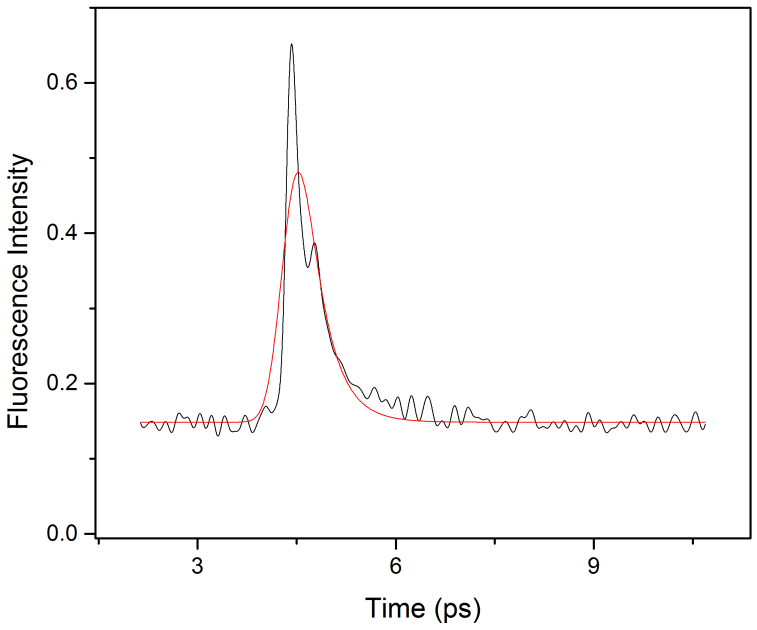

b

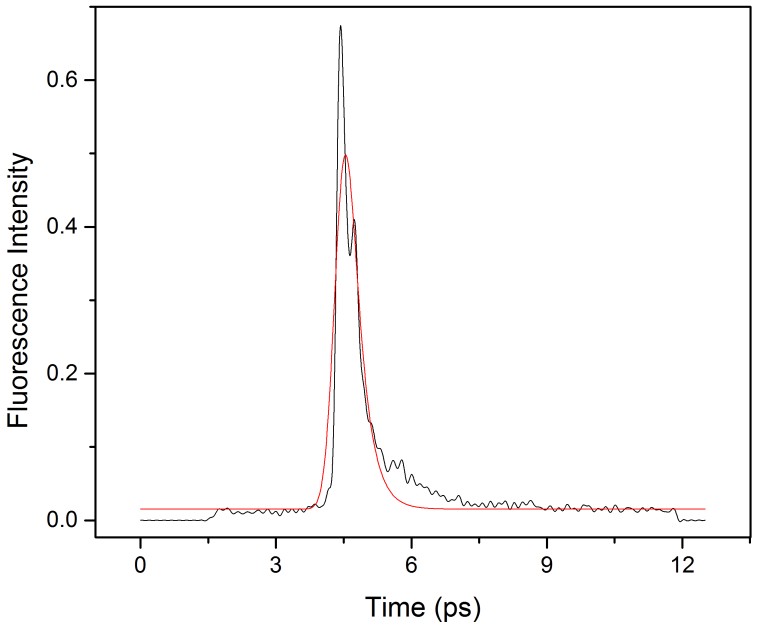

Figure 5.23: Sepia melanin two photon fluorescence time profiles. a) 550 nm decay profile, exponential fit with 0.317 ps. b) 635 nm decay profile, exponential fit with 0.44 ps.

Chapter 6: Conclusion

Coherent nonlinear optical microscopy is a rapidly developing field with large potential for application to biological imaging and detection. Nonlinear optical techniques share the advantages of high speed and resolution, three-dimensional focusing, minimal sample damage, and label free chemical selectivity. In addition, each modality has its own qualities that make it suitable for different applications. For example, sum frequency generation has a non-centrosymmetry requirement that gives it an advantage in studying interfaces and fiber structures, stimulated Raman scattering has a direct proportionality to the imaginary part of the susceptibility that enables it to reproduce spontaneous Raman spectra, and pump probe transient absorption has the capability of probing electronic modes with multiple degrees of freedom. The work presented in this thesis ranges from improving the nonlinear optical microscope setup, advancing understanding of phase effects on nonlinear microscopy measurements, to applications of different nonlinear spectroscopy and microscopy techniques to studying the optical and chemical properties of biological molecules. The optical design of achromatic lenses for sum frequency generation explores and demonstrates the feasibility of improving the technique through custom infrared lenses. The position dependent phase shift modeling for stimulated Raman scattering illustrates the effects on the spectra that can be present in different nonlinear optical microscopy measurement configurations and provides a method for analysis of these effects. The vibrationally-resonant sum frequency generation microscopy study of collagen shows the applicability of the VR-SFG microscope to clarifying collagen second order nonlinear susceptibility tensor terms that can not be determined with other techniques. Finally, the application of multiple optical techniques, including transient absorption

spectroscopy, to the study of melanin shows how these techniques can complement each other in providing different pieces of information on the whole picture of melanin molecular properties. The work in this dissertation shows the broad range of applications for nonlinear optical spectroscopy and microscopy, as well as the future potential for improving these techniques to provide even better performance.

REFERENCES

1. Suhalim, J.L., Boik, J.C., Tromberg, B.J., and E.O. Potma, *The Need for Speed*. Journal of Biophotonics, 2012. **5**: 387-396.
2. Boyd, R.W., *Nonlinear Optics, Third Edition*. 2008: Academic Press.
3. Raman, C.V., and K.S. Krishnan, *A New Type of Secondary Radiation*. Nature, 1928. **121**: 501-502.
4. Mukamel, S., *Principles of Nonlinear Optical Spectroscopy*. 1995: Oxford University Press.
5. Shen, Y.R., *Surface Properties Probed by 2nd-Harmonic and Sum-Frequency Generation*. Nature, 1989. **337**(6207): 519-525.
6. Zhuang, X., et al., *Mapping Molecular Orientation and Conformation at Interfaces by Surface Nonlinear Optics.* Physical Review B, 1999. **59**(19): 12632-12640.
7. Rocha-Mendoza, I., et al., *Sum Frequency Vibrational Spectroscopy: The Molecular Origins of the Optical Second-Order Nonlinearity of Collagen*. Biophysical Journal, 2007. **93**(12): 4433-4444.
8. Jacob, D., Shelton, R.L., and B.E. Applegate, *Fourier domain pump-probe optical coherence tomography imaging of Melanin*. Optics Express, 2010. **18**(12): 12399-12410.
9. Florsheimer, M., Brillert, C., and H. Fuchs, *Chemical Imaging of Interfaces by Sum Frequency Microscopy*. Langmuir, 1999. **15**(17): 5437-5439.
10. Hoffmann, D.M.P., Kuhnke, K., and K. Kern, *Sum-frequency Generation Microscope for Opaque and Reflecting Samples*. Review of Scientific Instruments, 2002. **73**(9): 3221-3226.
11. Sano, H., Mizutani, G., and K. Locharoenrat, *Demonstration of Confocal Sum Frequency Microscopy*. Physica Status Solidi C, 2009. **6**(1):304-306.
12. Raghunathan, V., et al., *Rapid Vibrational Imaging with Sum Frequency Generation Microscopy*. Opt. Lett., 2011. **36**(19): 3891-3893.
13. Murphy, D.B., and M.W. Davidson, *Fundamentals of Light Microscopy and Electronic Imaging, Second Edition*. 2013: Wiley-Blackwell.
14. T.H. Jamieson, *Decade Wide waveband Optic*s. SPIE ,1998. **3482**:306-320.

15. M. N. Polyanskiy, "Refractive index database," https://refractiveindex.info.
16. M.J. Weber, *Handbook of Optical Materials*. 2002, CRC Press.
17. Tropf, W.J., Thomas, M.E., and T.J. Harris, *Properties of Crystals and Glasses. Handbook of Optics, 2nd Edition Volume IV*. 1994: McGraw-Hill Professional.
18. J.M. Geary, *Introduction to Lens Design*. 2011: Willmann-Bell, Inc.
19. Herzberger, M., and C.D. Salzberg, *Refractive Indices of Infrared Optical Materials and Color Correction of Infrared Lenses*. Journal of the Optical Society of America, 1962. **52**(4):420-427.
20. Oliva, E., and S. Gennari, *Achromatic Lens Systems for Near Infrared Instruments*. Astron. Astrophys. Suppl. Ser., 1995. **114**:179-182.
21. L.G. Gouy, *Sur une proprieté nouvelle des ondes lumineuses*. Acad. Sci. Paris. CR, 1890. **110**:1251–1253.
22. Chung, C.-Y., et al., *Controlling stimulated coherent spectroscopy and microscopy by a position-dependent phase*. *Physical Review A.*, 2013. **87**(3), e033833.
23. R. Phillips, *In retrospect: The Feynman Lectures on Physics*. Nature, 2013. **504**(7478):30-1.
24. Raghunathan, V., and E.O. Potma, *Multiplicative and subtractive focal volume engineering in coherent Raman microscopy*. J Opt Soc Am A Opt Image Sci Vis., 2010. **27**(11):2365-74.
25. Suhalim, J.L., et al., *Characterization of cholesterol crystals in atherosclerotic plaques using stimulated Raman scattering and second-harmonic generation microscopy*. Biophys. J.,2012. **102**: 1988-1995.
26. Di Lullo, G.A., et al., *Mapping the ligand-binding sites and disease-associated mutations on the most abundant protein in the human, type I collagen*. Journal of Biological Chemistry, 2002. **277**(6): 4223-4231.
27. Hulmes, D.J.S., *Building Collagen Molecules, Fibrils, and Suprafibrillar Structures. Journal of Structural Biology*, 2002. **137**: 2-10.
28. Shoulders, M.D., and R.T. Raines, *Collagen Structure and Stability.* Annu Rev Biochem. 2009 ; **78**: 929–958.
29. Zoumi, A.; Yeh, A.; and B.J. Tromberg, *Imaging Cells and Extracellular Matrix In Vivo by Using Second-Harmonic Generation and Two-Photon Excited Fluorescence.*

Proc. Natl. Acad. Sci. U.S.A., 2002. **99** (17): 11014– 11019.

30. Tiaho, F., Recher, G., and D. Rouede, *Estimation of helical angles of myosin and collagen by second harmonic generation imaging microscopy*. Optics Express, 2007. **15**(19):12286-12295.
31. Su, P.-J., et al., *Determination of Collagen Nanostructure from Second-Order Susceptibility Tensor Analysis.* Biophysical Journal, 2011. **100**(8):2053-2062.
32. Han, Y., et al., *Polarization-Sensitive Sum-Frequency Generation Microscopy of Collagen Fibers*. Journal of Physical Chemistry B., 2015. **119**: 3356-3365.
33. Han, Y.; et al., *Mapping Molecular Orientation with Phase Sensitive Vibrationally Resonant Sum-Frequency Generation Microscopy*. J. Phys. Chem. B, 2013. **117** (20): 6149– 6156.
34. Nofsinger, J. B.; Forest, S. E.; Simon, J. D., *Explanation for the Disparity among Absorption and Action Spectra of Eumelanin.* J. Phys. Chem. B, 1999. **103**: 11428-11432.
35. Sarna, T., et al., *Interaction of radicals from water radiolysis with melanin.* Biochim. Biophys. Acta (BBA)—General Subjects, 1986. **883**(1): 162–167.
36. Hill, H.Z., and G. J. Hill, *UVA, pheomelanin and the carcinogenesis of melanoma.* Pigment Cell Res., 2000. **13**(Suppl 8): 140–144 (2000).
37. Gudbjartsson, D.F., et al., *ASIP and TYR pigmentation variants associate with cutaneous melanoma and basal cell carcinoma*. Nat. Genet., 2008. **40**(7): 886–891.
38. Ito, S., *A chemist's view of melanogenesis.* Pigm. Cell Res., 2003. **16**: 230.
39. Roland Mattern, https://commons.wikimedia.org/wiki/File:Eumelanine.svg
40. McGinness, J.; Corry, P.; and P. Proctor, *Amorphous semiconductor switching in melanins.* Science 1974, **183**: 853.
41. Liu, Y., et al., *Comparison of the Structural and Physical Properties of Human Hair Eumelanin Following Enzymatic or Acid/Base Extraction.* Pigment Cell Res, 2003. **16**: 355–365.
42. Capozzi, V., et al., *Raman and optical spectroscopy of eumelanin films*. Journal of Molecular Structure, 2005. 744–747: 717–721.
43. Mbonyiryivuze, A., et al., *Fourier Transform Infrared Spectroscopy for Sepia Melanin.* Physics and Materials Chemistry, 2015. **3**(2): 25-29.

44. Centeno, S.A., and J. Shamir, *Surface enhanced Raman scattering (SERS) and FTIR characterization of the sepia melanin pigment used in works of art*. Journal of Molecular Structure, 2008. **873**:149–159.
45. Piletic, I.R., Mattews, T.E., and W.S. Warren, *Probing Near-Infrared Photorelaxation Pathways in Eumelanins and Pheomelanins*. J. Phys. Chem. A, 2010. **114**: 11483–11491.
46. Simpson, M.J., et al., *Near-Infrared Excited State Dynamics of Melanins: The Effects of Iron Content, Photo-Damage, Chemical Oxidation, and Aggregate Size.* J. Phys. Chem. A, 2014. **118**: 993−1003.